ALMA MATER STUDIORUM
UNIVERSITÀ DI BOLOGNA

DOTTORATO DI RICERCA IN

Il futuro della terra, cambiamenti climatici e sfide sociali

Ciclo XXXVI

Settore Concorsuale: 04/A4

Settore Scientifico Disciplinare: GEO/12

A DOWNSCALING EXERCISE FOR THE COASTAL OCEAN WITH THE PERFECT MODEL APPROACH: A STUDY FOR THE ADRIATIC SEA

Presentata da: Renata Tatsch Eidt

Coordinatore Dottorato
Prof. Silvana di Sabatino

Supervisore:
Dr. Giorgia Verri
Co-Supervisori:
Dr. Vladimir Santos da Costa
Prof. Antonio Navarra

Esame finale anno 2024

I hope the unknown never
gets too familiar

Inspired by a book from one of
my favourite writers

Acknowledgements

I would like to start by mentioning how grateful I am for this opportunity in the first place, for being part of a great group at CMCC and followed by such great scientists.

I thank my supervisor Giorgia, who has always been close and guided me towards the most interesting outcomes and insights.

I thank my co-supervisors Vladimir and Murat, who shared their experience and knowledge in order to make this happen in the best way.

I thank prof. Antonio, who in my view could not have a better idea for this study.

I also would like to thank prof. Nadia, for her advices and her contagious passion about oceanography.

A special thanks to Anna, who is such an inspiration as scientist and as a person, and the main reason for the period abroad being a great and very productive experience.

I need to acknowledge the crossfit too, that for sure helped to keep my mind safe after heavy days.

Agradeço pela minha família, em especial minha mãe e meu pai, meu irmão e minhas irmãs. Obrigada por, mesmo distante, se manterem sempre por perto.

E claro, o que seriam desses anos sem o apoio e os conselhos do Leo, que acompanhou bem de perto, digamos, esse doutorado. E a Diana, que se tornou uma grande parceira e amiga para além das discussões sobre o NEMO.

Finally, there is a famous quote, attributed to Isaac Newton, that says: “If I see further, it is by standing on the shoulders of giants”. I could not agree more...

Abstract

Dynamical downscaling is extremely important for obtaining high resolution ocean simulations, providing information at regional to local scales with reduced computational cost especially for climate projections. This PhD project proposes a downscaling exercise for the Adriatic Sea with the perfect model approach. A large domain high resolution experiment covering the entire Adriatic Sea, referred to as the "truth", is used as benchmark for assessing a downscaling configuration for a small nested domain, the Northern Adriatic Sea.

A set of experimental setup with different nesting strategies have been performed based on the NEMO ocean model. Coarse (parent) experiments covering the entire Adriatic Sea provide boundary conditions for nested (child) experiments at the Northern Adriatic, which are finally compared with the "truth" experiment. This approach has shown to be a useful methodology to assess the downscaling performance of nested regional climate models and to investigate the best/tailored solutions for a particular domain of interest.

The downscaling performance of each nesting strategy was estimated by kinetic energy spectral analysis. Overall, the child experiments were able to regenerate small scale features and recover the energy not present at the boundaries. The 6 km to 2 km resolution ratio was found to be the best choice for the coastal downscaling, while higher downscaling ratio (from 10 km to 2 km) caused instabilities to grow and deviate from the "truth".

The reproducibility of physical processes and extreme events was evaluated by analysis of dense water formation and marine heat waves. Results show that dense water computation in the Northern Adriatic by the child experiment differs whether there is local or external contribution, relying on atmospheric conditions or lateral open boundaries, respectively. The entrance of saltier waters from the Levantine Basin was found to be decisive for the dense water formation in the last decade of study.

Surface marine heatwaves did not significantly differ between experiments, since it is mainly associated with local atmospheric conditions which are the same in all experiments. However, in depth the child experiment shows significant improvement with respect to parent, especially with respect to the duration of some events, which tends to be overestimated by the parent coarse experiment. Once again, when the warming events are more associated to local processes child experiment is closer to the truth, while when the events computed are more related to the advection of waters from the boundaries towards the inner domain, re-

producibility is more affected by the sea water properties of the parent experiment.

Dense water computation in the parent experiment revealed what can be assumed as an "inner value problem", meaning that a coarse resolution model limits the reproducibility of the dynamics in complex geometry within the computational domain such as the Otranto Strait. In the proposed coarse configuration, the entrance of saltier waters at the Otranto Strait is poorly represented by the coarse parent experiment, affecting the Adriatic Sea thermohaline properties and circulation with impact in the Northern sub-basin.

A final methodology was therefore proposed based on the spectral nudging technique, as an attempt to correct the density field inside the coarse resolution nested domain and overcome the drawback in dense water computation. Although spectral nudging was applied only for tracers, the inner domain circulation evolved accordingly. With that, the inflow of saltier waters at the Otranto Strait towards the Adriatic Sea was significant improved, evidencing the applicability of the tool for ameliorating the inner domain thermohaline circulation.

Contents

1 Introduction 16

1.1 Dynamical downscaling in the regional to coastal ocean 16

1.1.1 The perfect model approach 17

1.1.2 The spectral nudging technique 18

1.2 The Adriatic Sea 20

1.2.1 A shallow semi-enclosed bay: The Northern Adriatic Sea 23

1.3 Aim and objectives 25

1.4 Structure of the thesis 25

2 Dynamical downscaling in the Northern Adriatic Sea 27

2.1 The NEMO ocean general circulation model 27

2.2 The experimental design and the downscaling strategy 31

2.2.1 Large domain experiments: Parent Models 34

2.2.2 Small domain downscaling experiments: Child Models . . 37

2.3 Towards an eddy resolving ocean model 39

2.4 *Can we regenerate small scale features?* 42

2.4.1 Kinetic energy distribution 42

2.4.2 Spectral analysis of kinetic energy 45

2.5 Conclusions 54

3 Reproducibility study for the Adriatic Sea: a physical overview 56

3.1 Sea water properties of the Northern Adriatic Sea 56

3.2 *What is the reproducibility for selected physical processes and extreme events?* 60

3.2.1 Dense Water Formation 60

3.2.2 Looking at the "bigger picture": The entire Adriatic Sea . 64

3.2.3 Interannual thermohaline variability in the Northern Adriatic Sea 72

3.2.4 Marine Heat Waves 77

3.3 Our regional model for the Adriatic Sea: Validation 86

3.4 Conclusions 96

4 Spectral nudging application for coastal ocean modelling 98

4.1 Coastal modelling and the "inner" value problem 98

4.2 Design and implementation of spectral nudging 100

4.2.1 Filtering the small scales 103

4.2.2 Spatial variability of nudging 105
4.3 *Are we able to improve the representation of water mass structures with spectral nudging?* 107
4.4 A new downscaling experiment 114
4.5 Conclusions 117

5 Conclusions and future perspectives 119

Appendices 122

A Supporting material for Chapter 2 122
A.1 The model setup 122
A.2 Complementary figures 123
A.3 Kinetic energy under different wind stress computation 124

B Supporting material for Chapter 3 126
B.1 Complementary figures 126
B.2 Further discussion on dense water formation 126

C Supporting material for Chapter 4 130
C.1 Spectral nudging implementation on the fly 130
C.1.1 Interpolation and flooding at complex bathymetry 131
C.1.2 The linearity of the spectral nudging increment 132
C.2 Additional discussion on thermohaline properties 133
C.2.1 A new downscaling experiment in single nesting approach 134

References 147

List of Figures

1.1 Representation of the Adriatic / Ionian domain, with delimitation of the transect along the Otranto Strait. 20

1.2 Schematic representation of the Adriatic Sea circulation from Artegiani et al. (1997b). The figure illustrates the counterclockwise surface circulation dominated by eastern (eastern south Adriatic – E-SAd), western (Northern Adriatic – NAd, western middle Adriatic – W-MAd, western south Adriatic – W-SAd) boundary currents, and sub-basin scale cyclonic gyres (Northern – NAd, Middle – MAd, and Southern Adriatic – SAd gyres). Consider that the the basin is shifted so that left and right here represent northern and southern regions, respectively. The geographical representation of the basin can be seen in Figure 1.1. 22

2.1 Schematic representation of the perfect model approach for the Adriatic Sea with northern sub-region as nested domain. In the left is the large domain high resolution experiment (truth) and in the right the downscaling experiment. At the end the child experiment is compared with the accordingly same area of the truth experiment. Shading is a daily output of surface velocities, for illustration. 32

2.2 Adriatic Sea bathymetry (in meters) from EMODnet (2020) with 3.75 arc second horizontal resolution. Panel (a) covers the Adriatic Sea and part of the northern Ionian Sea, and panel (b) contains a section for the Northern Adriatic domain (with updated colorbar). 34

2.3 First baroclinic Rossby radius of deformation [km] for Winter (top figures) and Summer (bottom figures) calculated based on L2 outputs for the Adriatic Sea. Panels on the right correspond to Northern Adriatic sub-domain, with updated colorbar. 40

2.4 Seasonal mean EKE [$10^{-3}\,\mathrm{m}^2\,\mathrm{s}^{-2}$] of S0 experiment. Black line in right panel indicates the position of transect along longitude 13.3°E used for spectral analysis. 43

2.5 Basin average kinetic energy [$\mathrm{m}^2\,\mathrm{s}^{-2}$] for all three parent experiments (L6, L10 and L2F) and child S0 compared with truth L2. . 44

2.6 Eddy kinetic energy spectrum in the space (wavenumber) domain [cycles per km], computed from the surface (a) and depth averaged (b) velocities. Solid and dashed lines indicate parent and child experiments, respectively; the colors represent the nesting strategy. This computation was performed along a section at longitude 13.3°E, as illustrated in Figure 2.4. 47
2.7 Eddy kinetic energy spectrum in the time (frequency) domain [cycles per day], computed from the surface (a) and depth averaged (b) velocities. Solid and dashed lines indicate parent and child experiments, respectively; the colors represent the nesting strategy. This computation was performed along a section at longitude 13.3°E, as illustrated in Figure 2.4. 48
2.8 Maps of eddy kinetic energy spectrum [$\mathrm{m}^2\,\mathrm{s}^{-2}$] associated with the 4 months frequency, for: truth L2 (left); parent (middle) and their respective child (right) experiments. L2 and parent experiments domain was cut to focus on the Northern Adriatic (child domain). Depth averaged fields were used for this analysis. 50
2.9 Maps of EKE spectrum [$\mathrm{m}^2\,\mathrm{s}^{-2}$] associated with the 6 months frequency, for: truth L2 (left); parent (middle) and their respective child (right) experiments. L2 and parent experiments domain was cut to focus on the Northern Adriatic (child domain). Depth averaged fields were used for this analysis. 51
3.1 Vertical profiles of temperature monthly mean (a) and anomaly from its annual cycle (b), for truth L2 (top), parent L6 (middle) and child (S6) experiments in the Northern Adriatic area covered by the nested domain. 57
3.2 Vertical profiles of salinity monthly mean (a) and anomaly from its annual cycle (b), for truth L2 (top), parent L6 (middle) and child (S6) experiments for the Northern Adriatic area covered by the nested domain. 58
3.3 Vertical profiles of density monthly mean (a) and anomaly from its annual cycle (b), for truth L2 (top), coarse L6 (middle) and downscaling (S6) experiments for the Northern Adriatic area covered by the nested domain. Black contour line in left represents the density anomaly of 1029.2 $\mathrm{kg\,m}^{-3}$ 59

3.4 Daily river runoff for Po River based on observations from the Pontelagoscuro station, located 40 km upstream of river mouths. Red line corresponds to a running average with 180 days window. 60

3.5 Dense water volume (top), dense water temperature (middle) and dense water salinity (bottom) computed for each experiment for the area covered by the nesting experiments in the Northern Adriatic Sea. Solid and dashed lines represent, respectively, large domain (entire Adriatic Sea) and downscaling (Northern Adriatic) experiments. 62

3.6 Dense water volume computed for each large domain experiment (L2 and L6) compared with reanalysis data, for the three Adriatic sub-basins. The potential density threshold is 29.2 $\mathrm{kg\,m^{-3}}$ for Northern and Middle Adriatic, and 29.0 $\mathrm{kg\,m^{-3}}$ for Southern Adriatic. 65

3.7 Dense water temperature (left) and salinity (right) for “truth” L2 and parent L6 experiments, compared with reanalysis from CMEMS. 67

3.8 Basin average salinity [psu] for three different experiments (“truth” L2, parent L6 and child S6) and CMEMS reanalysis, computed for the area covered by the downscaling Northern Adriatic subdomain. Solid and dashed lines represent, respectively, large domain (entire Adriatic Sea) and downscaling (Northern Adriatic) experiments. 67

3.9 Seasonal transects for salinity [psu] (shaded) and meridional velocity [$\mathrm{m^2\,s^{-1}}$] (contour) along the Otranto Strait during the period 2011-2019, for coarse L6 (left) and “truth” L2 (right) experiments. 69

3.10 Maps of salinity [psu] at 10 m (top panels) and at 150 m depth (bottom panels) for coarse L6 (left) and “truth” L2 (right) at a daily output in 21/06/2012. (Updated color bar with depth) . . 70

3.11 Mean salinity and temperature at a zonal section at 39°N which are based on CMEMS reanalysis and correspond to the time series provided at the southern open boundary of the parent L6 experiment. The Otranto Strait is 2° north of this open boundary. 73

3.12 Mean surface circulation for period 2001-2005 (top-left), 2006-2010 (top-right),2011-2015 (bottom-left) and 2016-2019 (bottom-right) obtained from L2 experiment. 74

3.13 Mean intensity [°C] (left) and duration [days] (right) of MHW events computed for each experiment: truth L2 (top), parent L6 (middle) and child S6 (bottom), for the events encountered in the period 2001-2019. Red bar indicates the most intense and longest MHW event, in left and right panels, respectively. 79

3.14 Spatial MHW computation for the year 2007 at the sea surface, by means of total number of days (left), maximum intensity [°C] (middle) and number of events (right) for the experiments: truth L2 (top), parent L6 (middle) and child S6 (bottom). 82

3.15 Spatial MHW computation for the year 2007 at 20 m depth, by means of total number of days (left), maximum intensity [°C] (middle) and number of events (right) for the experiments: truth L2 (top), parent L6 (middle) and child S6 (bottom). 83

3.16 Spatial MHW computation for the year 2017 at 20 m depth, by means of total number of days (left), maximum intensity [°C] (middle) and number of events (right) for the experiments: truth L2 (top), parent L6 (middle) and child S6 (bottom). 84

3.17 Delimitation of the three Adriatic sub-domains (North – yellow, Middle – green, and South – blue) used for the validation. The Northern Adriatic sub-region corresponds to the same domain of the child experiments set up. The entire figure is the parent experiments domain, but the southern area which contains the Ionian Sea was ignored for the validation (dark blue). 86

3.18 Salinity RMSE and BIAS for truth experiment L2 compared with in situ observations, for the entire Adriatic Sea. Left and right panels separate two periods (2001-2011 and 2012-2019) which are linked to the multi-annual variability in the thermohaline properties identified. 90

3.19 Temperature RMSE and BIAS for truth experiment L2 compared with in situ observations, for the entire Adriatic Sea. Left and right panels separate two periods (2001-2011 and 2012-2019) which are linked to the multi-annual variability in the thermohaline properties identified. 91

3.20 Vertical profiles of Temperature and Salinity RMSE and BIAS for truth experiment L2 compared with in situ observations, computed for the each of the Adriatic Sea sub-basins (sub-domains delimitation can be seen in Figure 3.17). Top and bottom panels correspond to periods 2001-2011 and 2012-2019, respectively, which are linked to the multi-annual variability in the thermohaline properties identified. 92
3.21 Salinity RMSE and BIAS for parent experiment L6 compared with in situ observations, for the entire Adriatic Sea. Left and right panels separate two periods (2001-2011 and 2012-2019) which are linked to the multi-annual variability in the thermohaline properties identified. 93
3.22 Temperature RMSE and BIAS for parent experiment L6 compared with in situ observations, for the entire Adriatic Sea. Left and right panels separate two periods (2001-2011 and 2012-2019) which are linked to the multi-annual variability in the thermohaline properties identified. 94
3.23 Vertical profiles of Temperature and Salinity RMSE and BIAS for parent experiment L6 compared with in situ observations, computed for the each of the Adriatic Sea sub-basins (sub-domains delimitation can be seen in Figure 3.17). Top and bottom panels correspond to periods 2001-2011 and 2012-2019, respectively, which are linked to the multi-annual variability in the thermohaline properties identified. 95
4.1 Schematic representation of the nesting strategy for new experiment L6+, with inner domain being nudged towards the parent model (CMEMS reanalysis). Shading is a daily output of surface velocities, for illustration. 101
4.2 Signal response of the Butterworth filter for 1st, 2nd, 3rd and 4th order. 104
4.3 Horizontal (a) and vertical (b) variability of nudging parameter. 106
4.4 Maps of salinity at 10 m (top panels) and at 150 m depth (bottom panels) for L2 (left), L6 (middle) and L6+ (right) at a daily output in 21/06/2012. (Updated color bar with depth) 107
4.5 Mean circulation in L6 (left) and L6+ (right) experiments. Vectors indicate depth averaged velocity of currents [$\mathrm{m\,s^{-1}}$] and shaded fields correspond to depth integral of volume transport [Sv]. . . . 108

4.6 Vertical transect along the Otranto Strait with mean temperature [°C] (top) and salinity [psu] (bottom) fields for L2 (left), L6 (middle) and L6+ (right). Contour lines correspond to meridional velocity [$\mathrm{m}^2\,\mathrm{s}^{-1}$]. 109

4.7 Dense water volume computed for L2, L6 and L6+ compared with CMEMS reanalysis, for the three Adriatic sub-basins. The potential density threshold is 29.2 $\mathrm{kg\,m^{-3}}$ for Northern and Middle Adriatic, and 29.0 $\mathrm{kg\,m^{-3}}$ for Southern Adriatic. 110

4.8 Dense water volume (top), temperature (middle) and salinity (bottom) computed for L2, L6 and L6+ compared with CMEMS reanalysis, for the Northern Adriatic sub-basin. The potential density threshold is 29.2 $\mathrm{kg\,m^{-3}}$. 111

4.9 Time series of salinity (top) and temperature (bottom) at 2.5 m depth for experiment L6 (left) and L6+ (right) compared with in situ observations from fixed platform (45.5488°N 13.5505°E, indicated by the red mark on map). 112

4.10 Schematic representation of the downscaling experiment S6+ nested in parent L6+. Shading is a daily output of surface velocities, for illustration. 114

4.11 Time series of salinity (top) and temperature (bottom) at 2.5 m depth for child experiments S6 (left) and S6+ (right) compared with in situ observations from fixed platform (45.5488°N 13.5505°E, indicated by the red mark on map). 115

4.12 Dense water volume (top), temperature (middle) and salinity (bottom) computed for truth L2, parent L6 and L6+, and child S6 and S6+, for the Northern Adriatic sub-basin. The potential density threshold is 29.2 $\mathrm{kg\,m^{-3}}$. 116

A.1 Winter daily surface velocity [$\mathrm{m\,s^{-1}}$] field for means of qualitative comparison between for truth L2 (left), parent L10 (middle) and filtered solution L2F (right). 123

A.2 Schematic representation of how the spectral analysis was performed along the longitudinal transect in the frequency domain [cycles per day]. Middle figure is an illustration of the grid cells along the transect, indicating that the procedure is done for each grid point generating a spread of spectrum (right panel). The spectrum is the resulting PSD of depth averaged eddy velocities, having here S6 experiment as example. 124

A.3 Power spectral density of eddy velocity in the time (frequency) domain [cycles per day], computed for surface (a) and depth average (b). Solid and dashed lines indicate parent and child experiments, respectively; in orange (green) there are the experiments with relative (absolute) wind stress formulation. 125

B.1 Time series of daily values for Po River discharge and basin average surface salinity computed for truth L2, in the Northern Adriatic Sea domain (Correlation between the two fields is -0.68). 126

B.2 Delimitation of Northern, Middle and Southern Adriatic subbasins, used for the dense water computation of the large domain experiments covering the entire Adriatic Sea. 126

B.3 Dense water volume (top), temperature (middle) and salinity (bottom) computed for each experiment for the area covered by the nesting experiments in the Northern Adriatic Sea. Solid and dashed lines represent, respectively, parent and child experiments. 127

B.4 Basin average salinity for "truth" L2, parent L6 and parent L10 computed for the area covered by the downscaling Northern Adriatic sub-domain. 128

B.5 Salinity [psu] at 150 m from reanalysis of the Copernicus Marine Service for the entire Mediterranean Sea, during periods of anticyclonic (top) and cyclonic (bottom) circulation phase of the Northern Ionian Gyre (NIG). 129

C.1 Example of reanalysis field (temperature) interpolated to the model grid by using the horizontal extrapolation (top panel) or the vertical extrapolation (middle panel). Bottom panel is the original reanalysis grid. 132

C.2 Example of two different methods for computing the temperature increment for spectral nudging: filter of the difference between the fields (left), difference of the filtered fields (middle). Right panel corresponds to the difference between results of the two approaches. Note the differences in colorbar between the first two panels and the last panel, where values are of the order of 10^{-14} and are essentially noise. 133

C.3 Maps of salinity at 10 m (top panels) and at 150 m depth (bottom panels) for experiments L2, L6 and L6+ (first panels), compared with CMEMS reanalysis (right panels) in 21/06/2012. (Updated color bar with depth). 134

C.4 Time series of salinity (top) and temperature (bottom) at 2.5 m depth for multiple nesting (boundary conditions from L6+) downscaling experiment S6+ (left) and single nesting (boundary conditions from CMEMS reanalysis) S4R (right) compared with in situ observations from fixed platform (45.5488°N 13.5505°E, indicated by the red mark on map). 136

C.5 Dense water volume (top), temperature (middle) and salinity (bottom) computed for the Northern Adriatic sub-basin, for multiple nesting (boundary conditions from L6+) downscaling experiment S6+ and single nesting (boundary conditions from CMEMS reanalysis) S4R. The potential density threshold is 29.2 $\mathrm{kg\,m^{-3}}$. . . 137

List of Tables

2.1 List of large domain experiments (truth L2 and parent models) and the respective numerical choices 36
2.2 List of downscaling (child) experiments 38
A.1 Model setup 122

1 Introduction

1.1 Dynamical downscaling in the regional to coastal ocean

The increase demand on regional marine weather and climate information relies on high resolution prediction systems able to reproduce the different scales of motion. Avoiding significant computational cost and providing high resolution information at coastal levels, downscaling has become an indispensable practice in ocean modelling.

There is still large unknowns regarding energy transfer in the ocean, especially associated with reservoirs and dissipation (Ferrari and Wunsch, 2009). Therefore, being able to reproduce a system accounting for oceanic features at the various time and spatial scales can contribute to better understanding the different processes in the ocean and their interaction.

Mesoscale circulation plays a significant role in the heat transport and overall dynamics of the ocean (Marshall and Plumb, 1989). Most of the total kinetic energy is believed to be contained in mesoscale eddies (Ferrari and Wunsch, 2009). Depending on the region of study (i.e. latitude, stratification, depth) the length scale of the eddies may vary (Hallberg, 2013) and, consequently, the ideal horizontal resolution to explicitly reproduce them. Mesoscale variability in the Middle Adriatic Sea, for example, is characterized by eddies with a size of 10-20 km (Paschini et al., 1993), which increase in diameter as moving towards the open sea.

A proper representation of the mesoscale features and baroclinic instability depends on a model resolution sufficiently high to be considered eddy-resolving (Hurlburt et al., 2008). That means a model grid spacing small enough to resolve the Rossby radius of deformation with two grid points (Hallberg, 2013). As we move towards marginal areas and coastal seas, these values can reduce significantly (Pinardi et al., 2006). Moreover, seasonality can have a strong impact in the Rossby radius at shallow seas, mostly associated with structure of the water column varying from mixed and stratified.

In ocean modeling it is expected that increasing the resolution leads to an improvement of the representation of oceanic features that are not resolved by coarser models and therefore a better representation of the ocean state (Chassignet and Xu, 2017; Chassignet et al., 2020; Fox-Kemper et al., 2019). When considering semi-enclosed bays with shallow depths such as the Adriatic Sea, for example, a considerable high resolution model would be necessary to explicitly reproduce the mesoscale features. In this way, downscaling becomes a more viable alternative for refining the grid spacing at smaller nested domains.

Reliable regional model predictions depend on a trustful downscaling strategy capable of properly regenerating the smaller scale features not present in the parent driving fields. Nested modeling strategies are expected to be able to represent the multi-scale processes interaction in a reliable way. Therefore, evaluating the performance of the downscaling implementation can be considered a crucial step in coastal modelling.

1.1.1 The perfect model approach

The perfect model is a useful framework to assess the performance of downscaling and understand the limitations that might be associated with the nesting implementation. This approach states that, rather than observations, model simulations can be used as a reference in investigating a so-called "perfect model predictability". A large variety of studies can be made with the use of this methodology, with the advantage that this kind of prognosis is not affected by model errors, for example, or limitations associated to observations (Denis et al., 2002).

One well known application, predominantly for atmospheric predictions, is in the scope of downscaling. For studies involving nested regional models, the implementation of the perfect model framework has been frequently referred to as the "Big Brother" experiment. It has been widely used for atmospheric regional model studies (De Elia et al., 2002; Denis et al., 2002; Y. Liu et al., 2019; Skamarock et al., 2018), but up to now not significantly explored by the ocean modelling community (e.g. Pham and Hwang, 2020; Pham et al., 2016).

The perfect model approach suggests that there is a reference run, which is considered the "truth". In the scenario of downscaling studies, this "truth" is set to be a large domain high resolution experiment. Smaller domain downscaling experiments, with the same resolution as the "truth", are nested into a coarse resolution large domain parent model. The evaluation of the downscaling performance of the nesting strategy is finally achieved by comparing the child experiment to the reference "truth" run.

The philosophy of the perfect model experiment resembles the ones of the Observing System Simulation Experiments - OSSE (Hoffman and Atlas, 2016; Masutani et al., 2010), as in the latter it is also proposed a long free model run as the "truth", referred to as the "Nature run". The Nature run fields are used as synthetic observations, instead of actual observations, and in this way it is possible to evaluate the impact of new observing systems on operational forecasts. In the perfect model approach, our "truth" reference is a high resolution configuration covering a bigger domain, which works as a benchmark for the nested domain downscaled experiment.

By principle the perfect model experiment proposes the use of filtered boundary conditions for the downscaling, where the "truth" experiment is degraded to mimic a low resolution parent model (e.g. De Elia et al., 2002; Pham and Hwang, 2020). With this approach no additional dynamical experiment is needed to generate coarse boundary fields, which are instead statistically obtained by low pass filtering the "truth" fields. Although this method also avoids combining the contributions of different sources of errors (Pham et al., 2016), the filtered fields are not exactly representative of a realistic coarse resolution model output.

1.1.2 The spectral nudging technique

Sub-regional high-resolution models can capture well local and small-scale dynamical processes, but they can also generate unrealistic internal variability which leads to a misplacement of the large-scale patterns introduced at their lateral open boundaries. Long model simulations, such as climate projections, are known to be susceptible to "model drift" (i.e. a persistent unrealistic trend not related to changes in forcing or in the internal dynamics of the model). Furthermore, nesting high-resolution regional models into very coarse resolution Earth System Models used for global climate projections can lead to a large "resolution jump" between parent and child models.

Spectral nudging is a technique already well known among the atmospheric modeling community (von Storch et al., 2000; Waldron et al., 1996; among others), but only limited studies have implemented it towards improving ocean predictions and projections. In a usual dynamical downscaling with nesting approach, the parent model drives and provides information to the child model only along its lateral open boundaries. Ideally, the child model should act as a magnifying glass, such that it reveals the small-scale information associated with the parent's model larger-scale patterns.

The traditional nesting approach, however, through posing constraints only along the model's lateral open boundaries, can lead the child model to generating internal variability and ocean fields that are inconsistent with those of the parent model (Katavouta and Thompson, 2016; von Storch et al., 2000). In a spectral nudging approach, the area inside the nested domain is forced to satisfy large-scale flow conditions (von Storch et al., 2000). Thus the large scales of the downscaled experiment are constrained to follow the parent model, while the small-scale features evolve freely in the nested domain.

A similar technique that is also called spectral nudging has been proposed to applying corrections to the tracers (or momentum) equations, however based on a previously defined climatology instead of nudging towards the parent model solution; at this approach both temporal and spatial filter are applied so that only selected frequencies and wave numbers remain in the nudging terms (Thompson et al., 2006; Wright et al., 2006).

It is worth noting that the spectral nudging application for dynamical downscaling (Katavouta and Thompson, 2016; von Storch et al., 2000) should not be confused with the spectral nudging application for correction of seasonal biases and drift in ocean (regional or global) models (Thompson et al., 2006; Wright et al., 2006). Although the technique is quite similar, in the former spectral nudging is applied to constrain unrealistic internal variability in regional models that leads to decoupling, at least in terms of large-scales, of the regional nested model solution from the parent model fields used to drive the nested regional model along its lateral open boundaries. In the latter, spectral nudging is applied as to relax the ocean model's solution towards climatologies (usually monthly) on specific frequencies and wavelengths, so as to reduce model drift and seasonal biases without suppressing variability on shorter or longer time-scales not present in the climatologies.

The main difference in the implementation is that: (i) the spectral nudging for downscaling is applied using the time-evolving fields that come from the parent model (or the reanalysis) that was forced at the lateral open boundaries, and is relevant only to regional models; while (ii) the spectral nudging for bias and drift correction is applied to either regional or global models using climatologies, which can be independent from the lateral boundary conditions in the case of a regional model, and which do not include interannual and decadal variability or long-term trends. In our study we employ the spectral nudging technique as a downscaling method and apply constraints on large scales, but we do not apply any frequency-depending constraints.

In previous study conducted by Katavouta and Thompson (2016), spectral nudging contributed for placing large-scale features at correct locations in the water column. Moreover, even though nudging was applied only for tracers and at large scales, enstrophy and kinetic energy of the system were indirectly

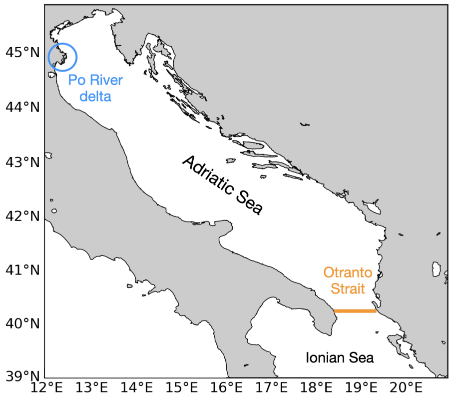

Figure 1.1: Representation of the Adriatic / Ionian domain, with delimitation of the transect along the Otranto Strait.

improved through the non-linearity of the governing equations. In addition to removing the decoupling between nested and parent model, the application of the technique in this study is expected to possibly correct inner domain features known to not be properly solved by the nested model.

1.2 The Adriatic Sea

A semi-enclosed bay, the Adriatic Sea (Figure 1.1) connects southwards with the Ionian Sea and accounts for an important branch of the Mediterranean thermohaline circulation (Pinardi et al., 2006). The connection between the Adriatic and the entire Mediterranean happens through a narrow passage at the Otranto Strait. Throughout this feature substantial exchange of salt and heat takes place and modulates the sea water properties at the basin (Astraldi et al., 1999; Vilibić and Orlić, 2002; Yari et al., 2012).

Due to its "land-locked" nature between the Balkans mountains and the Italian peninsula, the Adriatic Sea is also influenced by a variable local atmospheric forcing (Cushman-Roisin et al., 2013). Scirocco winds flow northwards, affecting the near surface circulation and contributing to the displacement of waters to the north, even enhancing the entrance of southern waters at the Otranto Strait (Artegiani et al., 1997b). During winter seasons, strong northeasterly winds named Bora contribute to major heat loss in the basin and are also important local drivers for dense water formation, especially in the Northern Adriatic Sea (Artegiani et al., 1997a; Vilibić and Supić, 2005).

Generally, tides in the Mediterranean Sea are considerably weak, with surface elevations of less than 1 m (Tsimplis et al., 1995). Within the Mediterranean, it is along straits and in the Northern Adriatic Sea where higher tidal amplitudes can be found (Malačič et al., 2000). Numerical studies have found that tides in the Northern Adriatic may have a contribution to mixing and stratification, and also impact the circulation of the sub-basin (Guarnieri et al., 2013).

Circulation in the Adriatic Sea is characterized by a basin-wide counterclockwise near surface circulation (Artegiani et al., 1997b; Cushman-Roisin et al., 2013). A schematic representation of the circulation at each of the three Adriatic sub-basins (north, middle and south) can be found in Figure 1.2 obtained from Artegiani et al. (1997b). The boundary currents and the sub-basin gyres present clear seasonal variability.

Mesoscale processes may have an important role in the formation and spreading of water masses (Gascard, 1978). In the Adriatic Sea, much of the meandering features along the Italian coast are associated with baroclinic instability which depend on the vertical stratification even more than the bathymetry configuration (Cushman-Roisin et al., 2007).

The Adriatic Sea is, in the long term, dominated by a mean surface heat loss of 19–22 Wm^{-2} (Artegiani et al., 1997a). Despite the large freshwater input from rivers to the basin, the enhanced cooling during winter seasons makes it a very important site for dense water production in the Mediterranean Sea (Pinardi et al., 2006). Dense water formation in the Adriatic is mostly classified as deep convection type and shelf type (Cushman-Roisin et al., 2013; Vilibić and Orlić, 2002): the former occurs in the center of the Southern Adriatic Pit, where the cyclonic circulation and ascending of the pycnocline associated with strong wind outbreaks in winter favour deep water convection (Manca et al., 2002); shelf type dense water formation, on the other hand, is mostly what happens in the Northern Adriatic Sea during cold and dry winters, when the shallow waters of this broad shelf experience significant surface buoyancy loss resulting in the North Adriatic dense water – NAdDW (Orlić et al., 1992; Vilibić and Supić, 2005; Zore-Armanda, 1963).

Circulation patterns and thermohaline properties in the Adriatic Sea have a strong interannual variability that is affected by local processes, i.e. atmospheric forcing and rivers, especially the Po River (Oddo et al., 2005); and external drivers, i.e. thermohaline circulation in the Mediterranean Sea (Cardin et al., 2011; Manca et al., 2006).

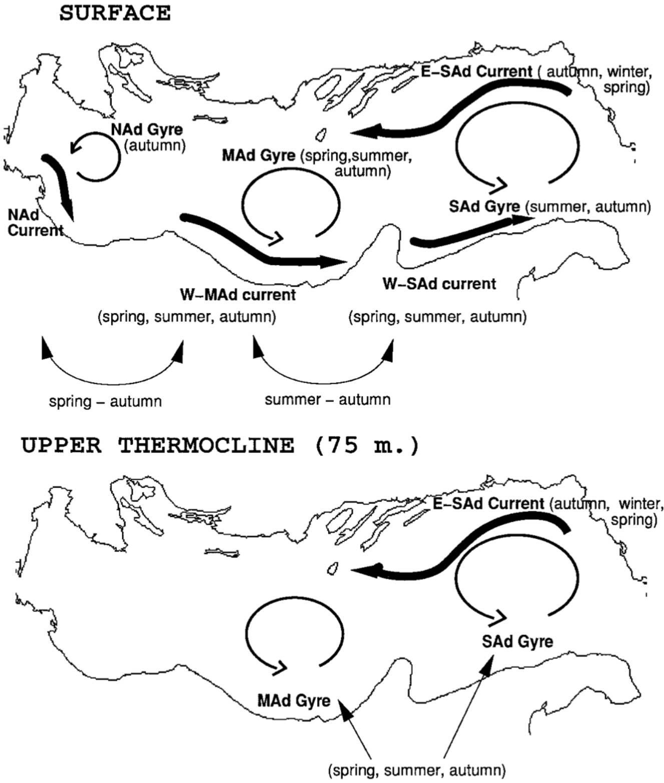

Figure 1.2: Schematic representation of the Adriatic Sea circulation from Artegiani et al. (1997b). The figure illustrates the counterclockwise surface circulation dominated by eastern (eastern south Adriatic – E-SAd), western (Northern Adriatic – NAd, western middle Adriatic – W-MAd, western south Adriatic – W-SAd) boundary currents, and sub-basin scale cyclonic gyres (Northern – NAd, Middle – MAd, and Southern Adriatic – SAd gyres). Consider that the the basin is shifted so that left and right here represent northern and southern regions, respectively. The geographical representation of the basin can be seen in Figure 1.1.

An important external driver for modulation of temperature and salinity in the Adriatic Sea is the general circulation at the Ionian Sea, i.e. Northern Ionian Gyre (NIG). Near surface circulation regime of the NIG, cyclonic or anticyclonic, preconditions the entrance of water masses towards the Adriatic, which can have characteristics from, either eastern or western, Mediterranean origin (Gačić et al., 2010; F. Liu et al., 2022; Pinardi et al., 2015). The cyclonic phase is actually among the preconditioning factors of dense water formation in the Southern Adriatic, associated with inflow of saltier waters from the Levantine basin. A complete discussion on this circulation regime and associated Adriatic properties will be performed in Chapter 3.

The effect of local drivers gives the Adriatic Sea its main characteristics as seasonally modulated by atmospheric conditions and highly influenced by freshwater input from rivers. At an even more local scale, the shallow Northern Adriatic Sea is a clear exemplification of these interesting processes.

1.2.1 A shallow semi-enclosed bay: The Northern Adriatic Sea

The Northern Adriatic Sea is a shallow region highly influenced by local atmospheric forcing, such as the Bora winds outbreaks (Cushman-Roisin et al., 2013), and river discharge, mainly the Po River in the western coast (Figure 1.1). At this sub-basin, a cyclonic circulation is formed mainly during autumn (Cushman-Roisin et al., 2013).

An essential component of the Mediterranean thermohaline circulation, the NAdDW is the densest water mass of the entire Mediterranean Sea (Zore-Armanda, 1963). This cold bottom water is originated during winter and renewed every season (Artegiani et al., 1997a). The main processes associated to the formation of the NAdDW are the strong and cold Bora winds, that favor the turbulent heat fluxes at the sea surface (Artegiani et al., 1997a; Vilibić and Supić, 2005).

At a cooling episode, dense water is produced at the surface and penetrates downwards until reaching the bottom, forming a dense bottom current that flows towards the deeper parts of the Middle Adriatic (Vested et al., 1998). The significance of this dense water production site makes the Northern Adriatic Sea a crucial contributor to the density driven circulation not only in the Adriatic basin, but in the entire Mediterranean Sea. Therefore, variations in dense water production in the Northern Adriatic can cause changes in the general thermohaline circulation and have strong effect in the Mediterranean deep waters (Pinardi et al., 2006).

1.3 Aim and objectives

This thesis proposes a downscaling study for a coastal domain in the Mediterranean Sea, the Adriatic Sea, with the perfect model approach. Inspired by the idea of introducing a methodology closely related to a real dynamical downscaling scenario, a different strategy have been implemented to the already known perfect model framework. Together with the original design of statistically (i.e. filtered) generated parent fields, a complete new coarse model simulation was also developed for a dynamically generated parent experiment. The use of a realistic parent model may evidence the actual limitations that are associated with the use of coarse resolution models as driving fields for nested regional models.

Our downscaling study here proposed is focused on the Northern Adriatic Sea. Based on known dynamics of the sub-basin, the downscaling performance in this perfect model framework will be assessed within a reproducibility study of physical processes and extreme events. The ability of child experiments in reproducing dense water formation and marine heat waves will be estimated by comparison with our "truth" reference. Our "truth" here will be considered a large domain high resolution experiment for the entire Adriatic Sea.

In regional experiments the nested solution may decouple from the driving parent model in the well known "boundary value problem". In this study, our large domain experiments cover complex geometries, such as the Otranto Strait, which, associated with limited resolution may reveal an "inner value problem". As an attempt to improve the thermohaline properties of a limited coarse resolution model, this thesis finally proposes a spectral nudging tool for coastal ocean modelling application.

The aim of the PhD is to perform a reproducibility study of the coastal ocean with the perfect model approach. The main questions to be addressed in the thesis are: 1) Can we regenerate small scale features? 2) What is the reproducibility for selected physical processes and extreme events? 3) Are we able to improve the representation of water mass structures with spectral nudging?

1.4 Structure of the thesis

This thesis is arranged in a sequence of motivations and questions, starting from a downscaling strategy for the Northern Adriatic Sea, moving towards a broader overview of ocean modelling in the coastal sea.

First, the downscaling setup for the Northern Adriatic Sea is proposed in

Chapter 2 with the perfect model framework. In this chapter analysis of kinetic energy allow the assessment of the downscaling performance and recommendation of an ideal downscaling strategy.

In Chapter 3 a reproducibility study is proposed for the downscaling experiments, this time covering the representation of physical processes and extreme events. Here it is discussed the thermohaline properties of the Northern Adriatic and its interannual variability based on our results and what is already known from literature. Our downscaling performance is assessed in terms of dense water formation and marine heat waves analysis.

At the end of Chapter 3 is where the model validation takes place. Temperature and salinity fields of the models outputs are compared with in situ observations, and the outcomes are discussed together with the main findings regarding the thermohaline properties. Finally some model improvements and future perspectives are proposed.

The outcomes of Chapter 3 led to an open discussion regarding the model setup, the representation of inner domain features in coastal modelling and the implications of horizontal resolution. Therefore, as an attempt to overcome the "inner domain" problem encountered and improve the representation of water mass structures, Chapter 4 proposes a spectral nudging tool for coastal ocean modelling.

The supporting material at the Appendices is expected to complement the material of each chapter. It contains explanations of modelling approaches, and further discussion on the numerical choices and the dynamics of the Adriatic Sea.

Despite the methodological approach of this numerical modelling study, the set of experiments proposed and even the limitations faced led to a better understanding of the dynamics of the Adriatic Sea and its interannual variability. Therefore, at each chapter, speculations and discussion on local and remote ocean processes that corroborate to the model outcomes are also covered.

2 Dynamical downscaling in the Northern Adriatic Sea

Assuming that numerical models are like laboratories, we can establish systems for predicting the ocean climate and make scenarios based on various hypothesis. They are incredible tools for understanding the physical properties of specific regions, and allow us to evaluate in what step we are towards the truth. The truth here can be any, actually, as long as we know it beforehand.

We may think of this study as an experimental laboratory, where we wish to investigate the behaviour of the coastal ocean in a downscaling configuration tailored for the Northern Adriatic Sea. It is important to emphasize that the main objective of this research does not hinge on the predictability or validation of our ocean model. Instead, it serves as a methodological investigation directed to the added value of a downscaling strategy.

This approach turned out to provide some valuable insights to scientific questions related to the thermohaline properties and dynamics of the Adriatic Sea. Our version of the truth involves conducting a large scale domain experiment with high horizontal resolution, and it is going to be our guide towards "reproducing the coastal ocean".

Throughout the subsequent sections, the experimental design and the concept of reproducibility will become clearer. The purpose of this chapter is to assess our downscaling performance across a series of different experiments within the perfect model framework for the Adriatic Sea. Strengths and limitations of the model and the implications of transitioning from coarse towards a near eddy-resolving resolution will be covered.

2.1 The NEMO ocean general circulation model

The ocean model used for this study is the finite difference Nucleus for European Modelling of the Ocean – NEMO 3.6 (Madec et al., 2017), which solves the primitive equations in a structured grid Arakawa C type. The primitive equations are based on the Navier-Stokes equations assuming Boussinesq and hydrostatic approximation, and are defined as follows:

Conservation of momentum for horizontal velocity vector field $\vec{u}_H = (u, v)$:

$$\frac{\partial u}{\partial t} + u\frac{\partial u}{\partial x} + v\frac{\partial u}{\partial y} + w\frac{\partial u}{\partial z} - fv = -\frac{1}{\rho_0}\frac{\partial p}{\partial x} + A_m(\frac{\partial^2 u}{\partial x^2} + \frac{\partial^2 u}{\partial y^2}) + \frac{\partial}{\partial z}K_m\frac{\partial u}{\partial z} \quad (2.1)$$

$$\frac{\partial v}{\partial t}+u\frac{\partial v}{\partial x}+v\frac{\partial v}{\partial y}+w\frac{\partial v}{\partial z}+fu=-\frac{1}{\rho_0}\frac{\partial p}{\partial y}+A_m(\frac{\partial^2 v}{\partial x^2}+\frac{\partial^2 v}{\partial y^2})+\frac{\partial}{\partial z}K_m\frac{\partial v}{\partial z} \quad (2.2)$$

Where (x, y, z, t) are the horizontal, vertical and time coordinates, and (u, v, w) are the horizontal and vertical velocity components. A_m and K_m correspond to the momentum eddy coefficients for horizontal and vertical turbulent viscosity, respectively, and $-fv$ and $+fu$ correspond to the horizontal components of the Coriolis term.

With the hydrostatic approximation, the vertical momentum equation is reduced to a balance between the vertical pressure gradient and the buoyancy force:

$$\frac{\partial p}{\partial z}=-\rho g \quad (2.3)$$

Where p is pressure, ρ is the density and g is the gravitational acceleration.

Equation of state:

$$\rho=\rho(T,S,p) \quad (2.4)$$

Prescribing sea water density ρ as an empirical nonlinear thermodynamic relationship to the state variables temperature T, salinity S and pressure p (following Fofonoff and Millard, 1983).

The advection-diffusion equations of salinity an temperature read as below::

$$\frac{\partial S}{\partial t}+\frac{\partial uS}{\partial x}+\frac{\partial vS}{\partial y}+\frac{\partial wS}{\partial z}=D_H(\frac{\partial^2 S}{\partial x^2}+\frac{\partial^2 S}{\partial y^2})+\frac{\partial}{\partial z}D_V\frac{\partial S}{\partial z} \quad (2.5)$$

Conservation of heat:

$$\frac{\partial T}{\partial t}+\frac{\partial uT}{\partial x}+\frac{\partial vT}{\partial y}+\frac{\partial wT}{\partial z}=D_H(\frac{\partial^2 T}{\partial x^2}+\frac{\partial^2 T}{\partial y^2})+\frac{\partial}{\partial z}D_V\frac{\partial T}{\partial z} \quad (2.6)$$

Where D_H and D_V are, respectively, the horizontal and vertical eddy diffusivity coefficients for tracers.

With the penetrative solar radiation implemented in the model, an additional term is added to the above time evolution equation for temperature (Equation 2.6):

$$\frac{\partial T}{\partial t}=...+\frac{1}{\rho_0 C_p}\frac{\partial I}{\partial z} \quad (2.7)$$

Where ρ_0 is a reference density, C_p is the specific heat capacity of sea water and I is the downward solar irradiance, representing the heat flux transmitted through the water column up to depth z_i:

$$I_i = I(z_i) = Q_s(T_r e^{\frac{z_i-\eta}{\lambda_1}} + (1-T_r)e^{\frac{z_i-\eta}{\lambda_2}}) \tag{2.8}$$

Where Q_s is the short-wave radiation flux, T_r corresponds to the transmission coefficient of the entering solar radiation based on Jerlov (1976) water type classification, and λ_1 and λ_2 are the length scales of solar penetration.

Continuity equation with incompressible approximation $\vec{u} = (u, v, w)$:

$$\frac{\partial u}{\partial x} + \frac{\partial v}{\partial y} + \frac{\partial w}{\partial z} = 0 \tag{2.9}$$

Free surface formulation:

$$\frac{\partial \eta}{\partial t} = -D + P + R - E \tag{2.10}$$

$$D = \nabla.[(H+\eta)\overline{\vec{u}_H}]$$

Where η is the sea surface height and H is the depth, P is precipitation, R is river runoff, E is evaporation rate .

The model solves prognostic variables, i.e. potential temperature, absolute salinity, sea surface height and the horizontal velocity components; and diagnostic variables, i.e. vertical velocity, potential density and hydrostatic pressure.

A time-splitting technique is used by the model to solve the primitive equations with linear free surface formulation. Also referred to as the split-explicit free surface formulation, it follows Shchepetkin and McWilliams (2005) and states that the free surface and the associated barotropic velocity equations will be solved at a smaller time step (Δt_e) than the one of the three dimensional prognostic values (Δt). It follows this relationship: $\Delta t_e = \frac{\Delta t}{n_{baro}}$, where n_{baro} was set to 60 for all experiments and Δt varies among them.

The air-sea interaction is parameterized by means of atmospheric fluxes with the use of interactive bulk formulae. In this study it was used the MFS (Mediterranean Forecasting System) bulk formulae developed by Castellari et al. (1998), that uses the model predicted sea surface temperature and the following atmospheric fields: temperature and dew point temperature at 2 m, sea level pressure, total cloud cover, precipitation, and wind at 10 m.

Bi-Laplacian operators are used for horizontal parameterization of lateral sub-grid scale mixing for both momentum and tracers. Horizontal eddy viscosity and diffusivity coefficients of each experiment are constant values, defined based on the resolution of parent and child model (Section 2.2).

The vertical mixing coefficients are computed with the turbulent closure scheme (TKE). No-slip boundary conditions are applied for the lateral land boundaries, and non-linear bottom friction was used for bottom boundary condition.

A synthesis of the NEMO model configuration and numerical choices is available at the Appendix section in Table A.1.

2.2 The experimental design and the downscaling strategy

The aim of this study is to propose a comprehensive “perfect model” framework, where a high resolution large domain experiment, referred to as L2, is considered our “truth” reference. This L2 experiment covers the entire Adriatic Sea at a 1/48° (approximately 2 km) resolution, and will be used to “validate” our downscaling experiments. These downscaling experiments cover a smaller domain in the Northern Adriatic Sea with the same high horizontal resolution. They are nested at different parent experiments, meaning different downscaling strategies, and are at the end compared to the truth L2. All parent experiments cover the same area as truth L2, the entire Adriatic Sea, but with lower horizontal resolution. A schematic overview of the perfect model approach can be seen in Figure 2.1.

In the set of experiments proposed, the resolution of the child experiment in the Northern Adriatic domain will be always the same as the truth L2, which is 1/48° (see Figure 2.1 for visualization). What varies is the horizontal resolution of the parent experiments and hence the resolution jump between parent and child. The different configurations will be introduced in the next Sections 2.2.1 and 2.2.2.

For the vertical discretization in this study, a z-coordinate with partial step is adopted, featuring 120 levels spanning from 1.2 to 2600 m. This partial step configuration adjusts the bottom layer thickness as a function of position to better align with the real topography, allowing for a more accurate representation of the bathymetry. The vertical grid is unevenly distributed, with a large number of layers in the top levels to ensure higher vertical resolution near the surface, moving to largely spaced as the depth increases. We use a stretching function to distribute the 120 z-coordinate vertical levels along the water column of the entire Adriatic domain, with appropriate thinning designed to better resolve the surface and intermediate layers (the stretching factor is 30 and the model level at which maximum stretching occurs is 80).

The atmospheric fields used as surface boundary conditions for the model were the analysis product of the Integrated Forecasting System (IFS) from the European Centre for Medium-Range Weather Forecasts (ECMWF), featuring a horizontal resolution of 0.125° at a frequency of 6 hours. The choice of the analysis product, instead of a reanalysis, was motivated by the higher horizontal resolution available, with the aim of capturing local features such as the Bora winds outbreaks. Total precipitation was, instead, obtained from the ECMWF

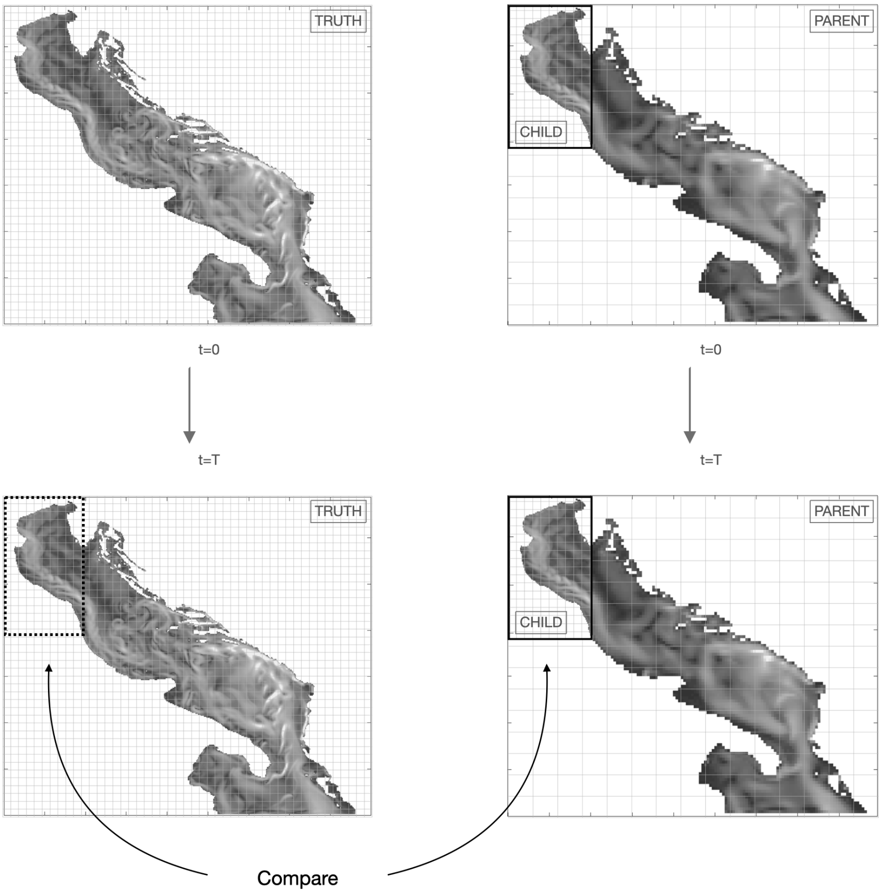

Figure 2.1: Schematic representation of the perfect model approach for the Adriatic Sea with northern sub-region as nested domain. In the left is the large domain high resolution experiment (truth) and in the right the downscaling experiment. At the end the child experiment is compared with the accordingly same area of the truth experiment. Shading is a daily output of surface velocities, for illustration.

reanalysis product ERA5 (Hersbach et al., 2020), characterized by a horizontal resolution of 0.25° and frequency of 1 hour. Atmospheric fields are interpolated to the model grid using bi-linear interpolation for most fields and bi-cubic for wind components.

Rivers inputs are provided as surface boundary condition at the respective river mouths in terms of volume flux and salinity. Salinity is set as a constant value of 17 PSU for Po River and 15 PSU for all other rivers, defined after previous studies (e.g. Verri et al., 2018) and sensitivity tests performed for the region (Oddo et al., 2005; Simoncelli et al., 2011). Runoff values for most rivers are based on monthly climatologies, except for the Po River, which incorporates observations from the Pontelagoscuro station located approximately 40 km upstream of river mouths. Daily mean data were obtained from Arpae (Agenzia Regionale per la Prevenzione e l'Ambiente) Emilia Romagna (https://simc.arpae.it). The total runoff from this catchment was divided into 9 separated river mouths in the model domain to correspond to the branches of the Po River delta.

In addition to the Po River branches, a total of 63 other river catchments are introduced to the model domain. Monthly climatologies for these respective rivers were converted into daily values using linear interpolation in time. This step followed the Killworth procedure (Killworth, 1996), involving the computation of "pseudo values" to conserve the correct monthly average value.

Figure 2.2 presents the bathymetry of the Adriatic Sea obtained from the European Marine Observation and Data Network - EMODnet (2020), used for the model configuration. This dataset contains a high horizontal resolution (3.75 arc second) that covers the complex coastlines of the Adriatic Sea. The bathymetry for each experiment was interpolated to the respective model grid, filtered to avoid numerical issues and manually modified at some critical coastline areas of eastern Adriatic.

Tides were not present in the modelling configuration. The inclusion of tides would probably represent an additional important feature for reproducing the local dynamics in a more realistic way (e.g. Guarnieri et al., 2013; Malačič et al., 2000). However, this feature was not included for the scope of this downscaling perfect model framework, which is directed to a climate study on a multiannual basis.

The series of experiments outlined in the following sections were designed to guide to the answers concerning coastal downscaling in the Northern Adriatic Sea. With the perspective of climate downscaling, the study covers a 19 years

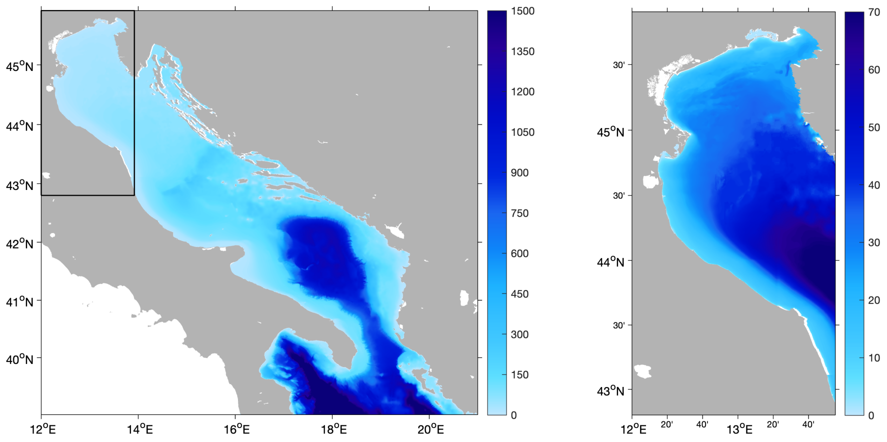

(a) (b)

Figure 2.2: Adriatic Sea bathymetry (in meters) from EMODnet (2020) with 3.75 arc second horizontal resolution. Panel (a) covers the Adriatic Sea and part of the northern Ionian Sea, and panel (b) contains a section for the Northern Adriatic domain (with updated colorbar).

time window of experiments, from 2001 to 2019.

2.2.1 Large domain experiments: Parent Models

The first large domain experiment, denoted as L2, serves as our truth reference, and covers the entire Adriatic Sea with high horizontal resolution. Other large domain parent experiments cover the same Adriatic Sea region but at coarser resolution. These parent experiments provide lateral open boundary conditions for the nested child experiments in the Northern Adriatic (Figure 2.1).

In prior studies employing the perfect model approach (e.g. De Elia et al., 2002; Denis et al., 2002; Pham and Hwang, 2020), low resolution boundary conditions for downscaling experiments were obtained by filtering the high resolution truth experiment. This involved using a low-pass filter to remove small scales, leaving only the large scales as boundary conditions for the child experiment, simulating a coarse resolution model. For this thesis, in addition to this method, a different approach was also implemented, meaning two distinct strategies that can be named as: "statistically" generated parent experiment (L2F), obtained through statistical methods by filtering the truth experiment L2; and "dynamically" generated parent experiments (L6 and L10), new numerical modelling experiments with low horizontal resolution.

The use of a completely new dynamical experiment as boundary condition for the child experiment can provide some valuable information of how a real downscaling scenario would be. We will be able to assess the limitations of a coarse resolution model for the Adriatic Sea and the gains with the downscaling. Moreover, the perfect model framework (both with the dynamically and statistically generated parent experiments) will be a useful tool to evaluate the performance and the added value of our dynamical downscaling strategy for the Northern Adriatic Sea.

The set of large domain experiments is detailed in Table 2.1, where the nomenclature references the respective horizontal resolution in kilometers. L2 represents our true experiment with 1/48° (2 km) horizontal resolution; while L6 and L10 correspond to the parent dynamical experiments with resolutions 1/16° and 1/10° (6 km and 10 km), respectively. Constant values of horizontal coefficients of viscosity and diffusivity were defined for each experiment. Such choices were made to ensure that the "only difference" between these experiments would be associated with the horizontal resolution.

Initial conditions were provided to the model as daily average salinity and temperature for the respective first day of simulation (01/01/2001), obtained from the reanalysis product of the Copernicus Marine Service (CMEMS) for the Mediterranean Sea (Escudier et al., 2021). These fields are 1/24° horizontal resolution and 141 unevenly distributed vertical z* levels, and were bi-linearly interpolated to the model grid.

The large domain experiments, covering the entire Adriatic Sea, have a southern open boundary that connects to the Ionian Sea at 39° N. The same reanalysis product from CMEMS were used for implementation of the ocean lateral boundary conditions, where the following fields were provided: ocean temperature and salinity, meridional and zonal baroclinic velocities, meridional and zonal barotropic velocities, sea surface height.

At the lateral open boundary, barotropic velocities were implemented to the model with Flather scheme (Flather, 1976), a radiation condition on the depth mean transport normal to the open boundary (Equation 2.11). The depth mean velocity normal to the boundary at the edge of the model domain is set to be equal to the external depth mean normal velocity, with the addition of a correction term to allow internally generated gravity waves to exit.

$$U = U_P + \frac{c}{H}(\eta - \eta_P) \tag{2.11}$$

Table 2.1: List of large domain experiments (truth L2 and parent models) and the respective numerical choices

Experiment	Horizontal Resolution	Eddy viscosity / diffusivity coefficients
L2	1/48° (2 km)	$-5e7$ / $-3e7$ $m^4\ s^{-1}$
L6	1/16° (6 km)	$-4.05e9$ / $-2.43e9$ $m^4\ s^{-1}$
L10	1/10° (10 km)	$-3.1e10$ / $-1.8e10$ $m^4\ s^{-1}$
L2F	1/10° (10 km)	–

U is the depth mean velocity normal to the boundary and η is the sea surface height of the nested model. The same fields with subscript P accounts for parent model source. c is the speed of external gravity waves ($c = \sqrt{gH}$), and H is the depth of the water column.

For both tracers and baroclinic velocities, imposition scheme was used, meaning that incoming and outgoing information were determined by the parent model (i.e. CMEMS reanalysis) regardless of the inner solution. In order to preserve the total volume transport at the open boundary, an "interpolation constraint" (Pinardi et al., 2003) was applied when introducing the reanalysis fields to the regional model grid. This means that, after the interpolation, the normal velocity field at the open boundary of the nested model grid was corrected with a correction term coming out by imposing the nested volume transport at the boundary to be equal to the one of the original parent model grid.

Maintaining the relationship of time-splitting explained at the previous section, baroclinic and barotropic time steps for each experiment were, respectively: 120 s and 2 s for L2; 200 s and 3 s for L6; 240 s and 4 s for L10.

L2F is our statistically generated experiment, obtained by filtering truth L2, and is exactly what the perfect model approach proposes. Using a low-pass Gaussian filter (Eq. 2.12) the small scale variability of L2 was removed so that the energy of the filtered solution (L2F) would resemble one of a coarse model (i.e. L10).

$$G(x,y) = \frac{1}{2\pi\sigma^2} e^{-\frac{x^2+y^2}{2\sigma^2}} \tag{2.12}$$

The coarse experiment L10 was thus used as a benchmark for judging the filter choices to be applied in L2 in order to obtain L2F, being w the window and

σ the standard deviation used, in units of grid points. Sensitivity analysis for the final choice of the filter parameters ($w = 20,\ \sigma = 6$) was performed based on comparison of kinetic energy time series (further in this chapter) and spatial maps of surface currents (Appendix A) between the resulting filtered fields (L2F) and the coarse experiment L10. The procedure was done iteratively for each vertical level, and land points were flooded to avoid impact of coastlines when applying the filter.

2.2.2 Small domain downscaling experiments: Child Models

All child experiments maintain the same resolution as the truth L2, 1/48°, with identical model configuration and time step. In this case, however, they specifically cover the small domain of the Northern Adriatic and are nested within the parent models listed in Table 2.1. Eddy viscosity and diffusivity coefficients remain consistent across experiments, set at –5e7 and –3e7 $m^4\ s^{-1}$, respectively, mirroring the values of the truth L2.

For these downscaling experiments, the same z-geopotential coordinate discretization as the parent models are employed. Given the shallower nature of the Northern Adriatic region, with a maximum depth of approximately 70 m in the nested domain, a reduced number of vertical levels remains present for this sub-domain model configuration. Nevertheless, due to the high vertical resolution in the top levels, the downscaling domain maintains a significant number of 35 vertical layers, which can be considered as a very detailed discretization for the shallow domain.

Generally, in downscaling implementations, the increase in resolution in the nested model configuration is performed not only in the horizontal, but also in the vertical discretization. Less vertical levels in the parent experiments would imply changes in the parent and child solutions. However, the purpose of this study was focused on addressing the impact of the increase in the horizontal resolution. Therefore, a ‘mechanistic approach’ is used by changing only the horizontal spacing between parent and child domain and with the downscaled experiment reaching the same resolution as the “truth” experiment. Adding also a downscaling ratio in the vertical discretization would have brought an additional source of speculation to the discussion with the representation of the vertical dynamics and turbulent mixing affected by the vertical resolution ratio.

Boundary conditions are sourced from the previously generated parent experiments, and the nesting strategies are outlined in Table 2.2. The child ex-

Table 2.2: List of downscaling (child) experiments

Child Experiment	Parent	Downscaling Ratio
S0	L2	1
S6	L6	1:3
S10	L10	1:5
S2	L2F	1:5

periments are named after their respective parent except for S0, which is the control setup.

Two dynamical nesting strategies for downscaling are proposed, with child S6 and S10 nested within parents L6 and L10, respectively. In addition to the downscaling approaches, a control experiment, referred to as the "best nesting", was conducted with S0 nested in L2; both parent (L2) and child (S0) have the same horizontal resolution, thereby mitigating any issue related to resolution jumps. This setup allows for the isolation of outcomes related to the nesting setup, enabling an evaluation of the boundary implementation. Finally, S2 corresponds to downscaling from the statistically generated parent L2F (L2 filtered).

For the implementation of the eastern lateral open boundary of the child experiments again the Flather radiation scheme (Flather, 1976) was adopted for the barotropic velocities. For tracers and baroclinic velocities the Orlanski scheme with radiation plus relaxation algorithm was used (Marchesiello et al., 2001), and it is referred to as a normal propagation of oblique radiation (NPO) approximation. At this time a sponge layer of 5 grid points was used with an inflow and outflow damping time scale of 1 and 30 days, respectively. The time scale of the outward propagation points is larger so that at inwards propagation points the solution is constrained more strongly by the external data (Madec et al., 2017).

Baroclinic and barotropic time steps for the nested experiments were set to be the same as truth L2, i.e. 120 s and 2 s, respectively.

2.3 Towards an eddy resolving ocean model

The first baroclinic Rossby radius of deformation is associated with the spatial scales of baroclinic instabilities (Ferrari and Wunsch, 2009), and can provide insight into our progress in explicitly resolving eddy variability in our ocean model. This parameter is often used as a criteria for distinguishing ocean models between eddy-permitting or eddy-resolving (Hallberg, 2013; Hurlburt et al., 2008). We can assume that, for an ocean model to be classified as eddy-resolving, its horizontal resolution should be at least two times smaller than the local Rossby radius of deformation (Hallberg, 2013), indicating that baroclinic instabilities can be explicitly resolved.

The Rossby radius of deformation (Rd) relates to the horizontal length scale of motion with the local buoyancy and rotation (Marshall and Plumb, 1989), and can be calculated with the following equation:

$$Rd = \frac{NH}{f} \tag{2.13}$$

Where H is interpreted as the vertical scale of motion, f is the Coriolis parameter, and N is the Brunt-Väisälä frequency:

$$N \equiv \sqrt{-\frac{g}{\rho}\frac{d\rho}{dz}} \tag{2.14}$$

Where g is the gravitational acceleration and ρ is the potential sea water density.

Consequently, Rd varies according to local density properties (i.e. stratification), latitude, and the depth of the region. As will be discussed in the next chapter, the Northern Adriatic is significantly influenced by seasonal variability. Its shallow waters exhibit a shift in the vertical profile structure from well mixed in winter to stratified in summer. Given this, the Rossby radius of deformation is expected to demonstrate large seasonality in the Northern Adriatic Sea.

Figure 2.3 illustrates maps of Rossby radius for the Adriatic Sea, calculated based on outputs from our truth experiment L2. These results can be used as indicators of the regions where the model can explicitly resolve eddies based on its spatial resolution.

Our results are in agreement with what the literature on the Mediterranean Sea proposes, which states that the Rossby radius of deformation varies from 5 to 12 km for the entire Mediterranean Sea (Grilli and Pinardi, 1998; Pinardi

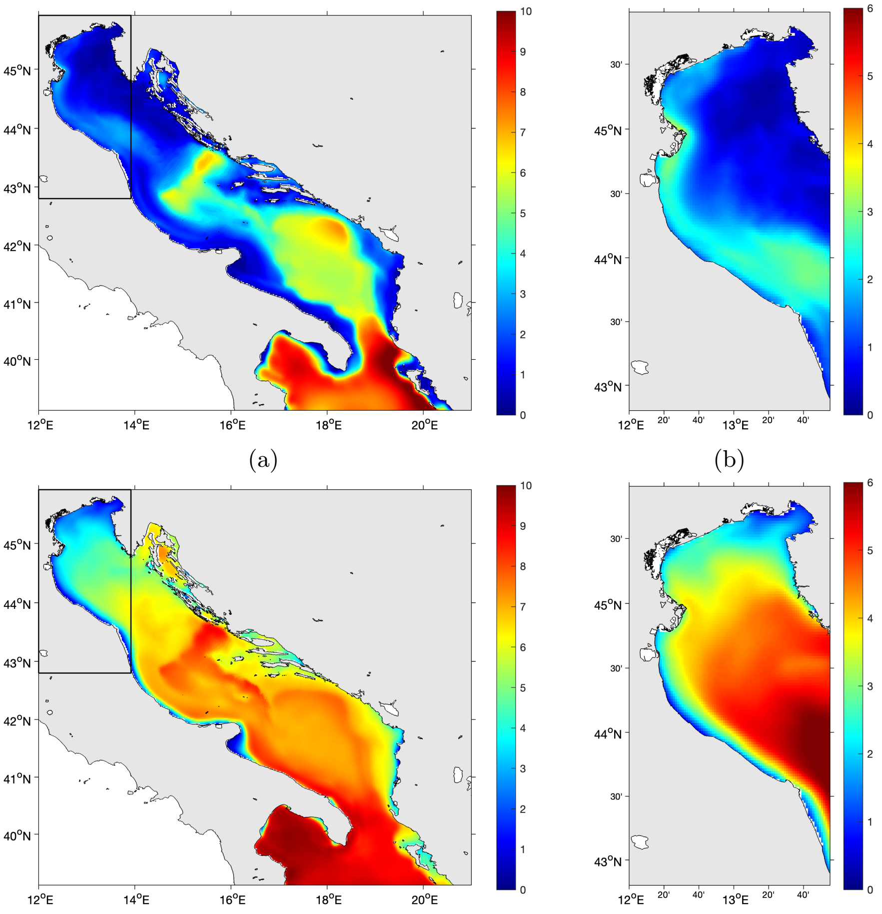

(a) (b)

(c) (d)

Figure 2.3: First baroclinic Rossby radius of deformation [km] for Winter (top figures) and Summer (bottom figures) calculated based on L2 outputs for the Adriatic Sea. Panels on the right correspond to Northern Adriatic sub-domain, with updated colorbar.

and Masetti, 2000) but reduces next to shallow regions as it is the case of the Northern Adriatic Sea, reaching 3-4 km in summer and 1 km in winter (Bergamasco et al., 1996; Cushman-Roisin et al., 2007; Masina and Pinardi, 1994; Paschini et al., 1993).

The observed seasonality, particularly within our downscaling domain, the Northern Adriatic Sea, implies that the model's ability to reproduce small scales varies significantly not only in space but also over time. The maps illustrate that Rd is less than 3 km in winter and around 6 km in summer. Moving southwards, with greater depths towards the Ionian Sea, Rd increases.

During winter periods in the Adriatic Sea, characterized by strong wind events, the shallow waters in the Northern sub-basin exhibit a vertically mixed profile. In this scenario, small Rd of around 1 km requires a very high-resolution model to explicitly resolve small scale dynamics. In contrast, in summer there is the stratified vertical profile with greater Rd, where our high resolution model with a 2 km grid spacing can be considered eddy resolving.

By having a 2 km horizontal resolution in the Northern Adriatic Sea domain it means that the model is actually on a threshold limit of eddy-permitted/eddy-resolving, and its ability changes in time. The choice of 2 km resolution was made with a prospective climate application of this model configuration, although it becomes clear from the Rd that an ideal representation of the eddy field would require a finer resolution. However, being on the limit between eddy-permitting and eddy-resolving actually allows for an interesting study on the model assessment and possible gains when moving from one configuration to another, as we will see in the next sections.

2.4 *Can we regenerate small scale features?*

The subsequent analyses focus on evaluating the ability of the downscaling experiments in regenerating small scale features, using truth L2 as a reference. This assessment is performed by statistical means, looking at the kinetic energy of the system rather than at specific mesoscale events. Seasonal maps and time series of kinetic energy (section 2.4.1) can provide information on the distribution and transfer of energy in both space and time, for the different experiments. Further spectral analyses (section 2.4.2) help to investigate the time and space dependence of kinetic energy in order to evaluate the performance of the downscaling experiments at each time and length scales.

2.4.1 Kinetic energy distribution

When developing a downscaling strategy, understanding the implications of implementing boundary conditions in a regional model is crucial. In a reproducibility study, comparing the downscaling regional model with a global (or large domain) equally high resolution model allows for assessing boundary-related limitations and evaluating the performance of downscaling. Additionally, comparing coarse and high-resolution models helps gauge the added value of increased horizontal resolution in coastal ocean modelling.

The study addresses the boundary value problem through a "best" nesting approach, where both parent and child experiments share the same high resolution, avoiding a jump in resolution at the nesting. A new experiment, S0, was conducted with boundary conditions from the truth reference L2. Comparing S0 with L2 helps isolate the "irreducible error", revealing the error associated with implementation of the lateral boundary condition. Any difference between child and parent experiments in this case represents the minimum error one could expect in subsequent downscaling strategies, providing insights into boundary condition implementation and the best achievable outcome in a perfect downscaling scenario.

Figure 2.4 illustrates the seasonal mean eddy kinetic energy (EKE) computed for experiment S0, the optimal solution achievable with the current downscaling strategy. The panels also indicate the energy features of our inner domain and their seasonality. The circulation of the sub-basin is characterized by an average inflow at the northern part of the open boundary, and dominant outflow through the south.

Energy associated with the Po river delta and the western current feature

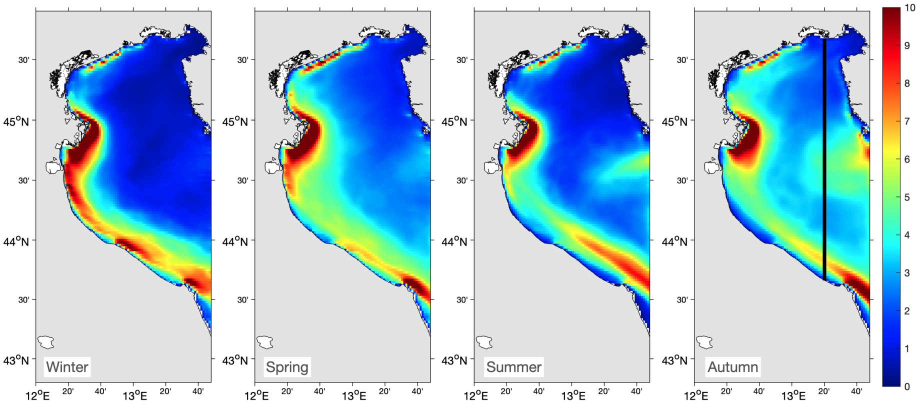

Figure 2.4: Seasonal mean EKE $[10^{-3}\,\mathrm{m}^2\,\mathrm{s}^{-2}]$ of S0 experiment. Black line in right panel indicates the position of transect along longitude 13.3°E used for spectral analysis.

is evident for basically all year long. The western current moving southwards along the Italian coast presents more meanders during winter season and turns into a stronger and better developed current in summer (Orlić et al., 1992). In summer and autumn we can see the energy associated with the Northern Adriatic cyclonic gyre, which presence has been previously reported mainly for autumn months (Artegiani et al., 1997b; Cushman-Roisin et al., 2013).

Time series of basin-average kinetic energy (KE) offer insights into the overall energy variability in the Northern Adriatic Sea and facilitate comparisons between different experiments, as shown in Figure 2.5 for the period 2012-2015.

As mentioned previously, this analysis on KE was also important for the definition of filter choices for L2F. By performing sensitivity tests, different filter parameters were tested in order to obtain a resulting L2 filtered solution which would resemble L10 fields. As can be seen in Figure 2.5, L2F KE (third panel) is comparable to L10 KE (second panel). Further comparison on surface current velocity can be found at the Appendix in Figure A.1.

Examining the bottom panel with L2 and S0 time series, higher energy levels during summer and autumn are evident. This aligns with the presence of the Northern Adriatic cyclonic gyre during this period, suggesting that our model effectively resolves the eddy field during these seasons, consistent with the larger local Rossby radius of deformation observed during summer.

From the three upper panels we can notice that it is also during these seasons that KE in coarse (L10, L6 and L2F) and high (L2) resolution models differs

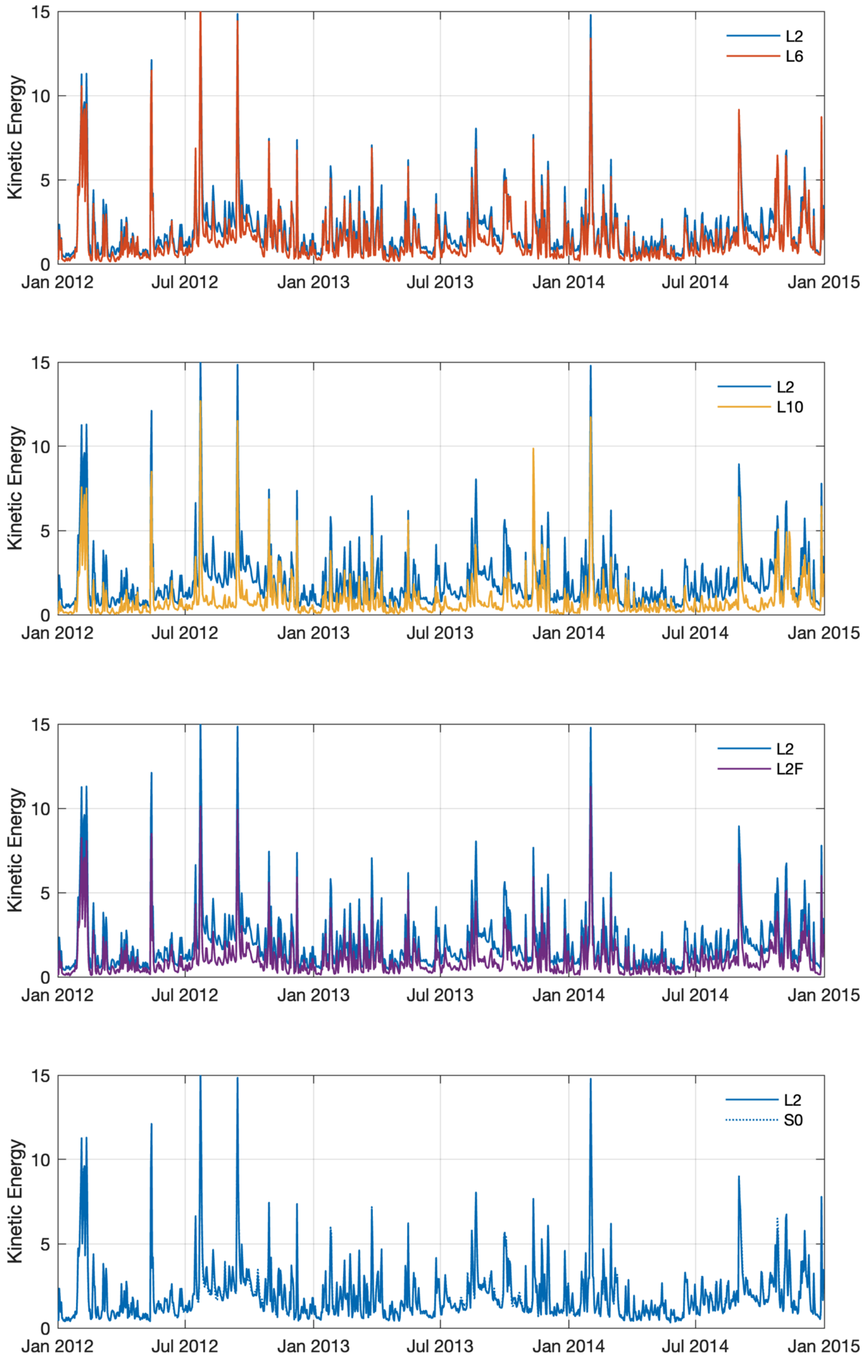

Figure 2.5: Basin average kinetic energy [$\mathrm{m}^2\,\mathrm{s}^{-2}$] for all three parent experiments (L6, L10 and L2F) and child S0 compared with truth L2.

the most. This stands out on the second panel in comparison between L10 and truth L2. During summer/autumn L2 resolution is closer to eddy-resolving and, therefore, it is expected to be able to explicitly reproduce the mesoscale features in the domain. During winter, however, not even our high resolution model is capable of resolving the eddy field, and mean KE in this season do not differ significantly from the coarse models.

Finally, comparison between KE of parent L2 and child S0 are represented in the bottom panel. The two time series are basically overlapped, indicating that no significant problem is associated with the nesting and child experiment reproduces the same pattern as its parent. The other downscaling strategies will be next evaluated through spectral analysis of KE.

2.4.2 Spectral analysis of kinetic energy

Power spectral density analysis of eddy velocity (leading to eddy kinetic energy) were performed in both space and time domain for all parent and child experiments. This study has been done for a section along longitude 13.3°E, illustrated in Figure 2.4 right panel. This transect is expected to comprise the northern inward and southern outward flow and the features associated with the Northern Adriatic cyclonic gyre, and at the same time avoid instabilities very close to the open boundary.

For the computation of the KE spectrum the spectral analysis was performed in two approaches: in space (wavenumber), for each day over the spatial transect; and in time (frequency), for each grid point of the transect over time. At the end the resulting feature is a “spread” of spectrum and we can calculate the average in time and space, for the wavenumber and frequency analysis, respectively. A schematic representation of this analysis can be seen at the Appendix in Figure A.2.

This analysis was performed following the subsequent steps: (i) remove time and space mean from u and v velocity components, resulting in eddy velocities (u' and v'); (ii) apply a windowing step to the data series; (iii) calculate the Fast Fourier Transform (FFT) and compute the power spectrum density (PSD) for u' and v'; (iv) apply a window correction to account for step ii; (v) filter (smooth) the final spectrum in order to increase statistical significance; (vi) sum the PSD of the two eddy velocity components leading to an equivalent of the EKE.

The windowing step (ii) is used to minimize “spectral leakage” that may occur when applying the FFT if there is discontinuity in the start end points of a time series. We thus multiply a smooth window function (taper) so that the amplitude varies gradually towards zero at the edges. Later, after computing the FFT, we apply the window correction to re-scale the spectrum accounting for the energy that was lost in the previous step with the windowing. Different types of data windows can be used; for this study it was applied the Hanning window (Oppenheim, 1999).

FFT (Frigo and Johnson, 2005) computes the discrete Fourier transform of a signal with length n decomposing the sequence of values into components of different frequencies. The transforms are defined as:

$$Y(k) = \sum_{j=1}^{n} X(j) W_n^{(j-1)(k-1)} \tag{2.15}$$

where W_n is the root of unit:

$$W_n = e^{(-2\pi)/n}$$

The PSD afterwards is calculated by multiplying the amplitude of the FFT by its conjugate and normalize it to the frequency (or wave length) of the bin width. Thus, in this case, we consider either the time interval (i.e. 1 day) for the frequency analysis, or the space interval (i.e. model grid size in km) for the wavenumber analysis.

Figure 2.6 contains the results of PSD of eddy velocity in the space domain in terms of wavenumber. Overall we can see that the downscaling experiments are able to generate higher energy than their respective parent experiments, as expected, for all wavelengths. In comparison with truth L2 we can verify, however, that some nesting approaches have better performance than others.

Notably, for large scales (small wavenumber), child experiment S10 overestimates the energy present in truth L2, even though its parent L10 has very low associated energy. Compared with S10, S6 appears to be a better downscaling approach (ratio 1:3), recovering energy comparable to truth L2. Downscaling from the filtered solution L2F, experiment S2 contains surface EKE very similar to L2. In depth, however, as shown by the right panel, S2 is not capable of recovering the same amount of energy as the other downscaling strategies.

In spectral estimates of ocean variability in the wavenumber domain the energy increases with wavelength (Ferrari and Wunsch, 2009), as it was seen in the previous picture. In the frequency PSD analysis in Figure 2.7, however, we

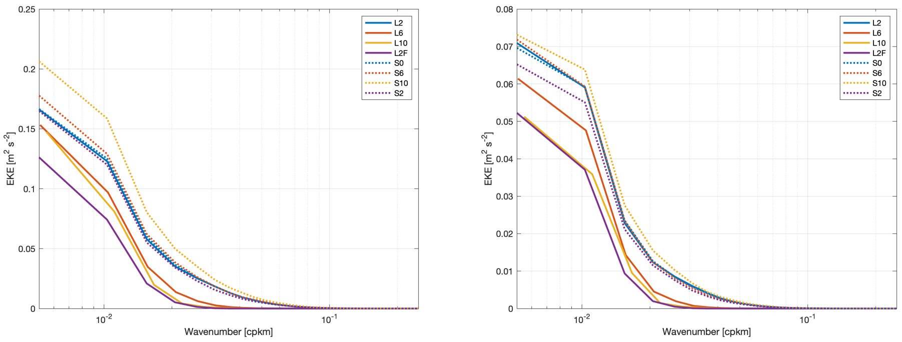

(a) (b)

Figure 2.6: Eddy kinetic energy spectrum in the space (wavenumber) domain [cycles per km], computed from the surface (a) and depth averaged (b) velocities. Solid and dashed lines indicate parent and child experiments, respectively; the colors represent the nesting strategy. This computation was performed along a section at longitude 13.3°E, as illustrated in Figure 2.4.

now see a completely different pattern. At this time the spectrum is composed of distinctive features with a frequency associated, that we can refer to as peaks of energy. This means that each peak corresponds to different features with specific time frequencies.

Although the same peaks of energy are present in all experiments, low resolution implies in the inability of reproducing the same amount of energy. It is easy to notice that child experiments have higher EKE than parent experiments for all frequencies. This result is expected as the increase in resolution corresponds to a better representation of the smaller scales features and therefore higher energy associated. Nevertheless, the proportion of energy increase with the downscaling and the model performance with respect to truth L2 vary depending on the nesting strategy and the associated frequency.

In agreement with wavenumber results, once more we can identify the analogue pattern between S0 and truth L2. Moreover, child S6 is also able at recovering equivalent amount of energy, as already observed in the previous wavenumber analysis. In surface analysis of EKE, S6 solution is very similar to truth L2. This could be expected since it is mostly a direct result of the atmospheric forcing. For depth average EKE, in 6 and 4 months there is a slight underestimation and overestimation, respectively; but still the results are promising and there is a considerable improvement with respect to the S10 strategy. This gives an indication that our downscaling approach with 1:3 ratio (S6)

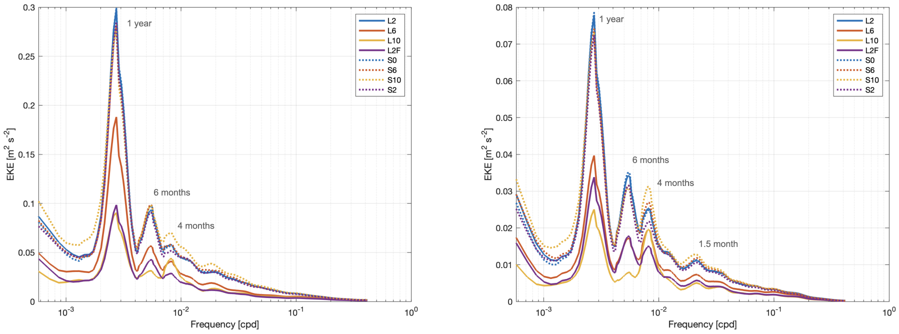

(a) (b)

Figure 2.7: Eddy kinetic energy spectrum in the time (frequency) domain [cycles per day], computed from the surface (a) and depth averaged (b) velocities. Solid and dashed lines indicate parent and child experiments, respectively; the colors represent the nesting strategy. This computation was performed along a section at longitude 13.3°E, as illustrated in Figure 2.4.

is capable of regenerating the inner domain features accordingly to the truth experiment, even though the parent experiment L6 have much lower energy.

Results of S2 indicate that the model is capable in regenerate the small scales even though very low energy is provided at the boundaries. However S2 slightly underestimates the L2 energy as can be seen for 6 and 4 months peaks in the depth averaged analysis (panel (b)). Results of the different nesting strategy with S2 and L2F comparing to nesting of L10 and S10 also evidence how the downscaling performance changes between the two approaches.

For the dynamical nesting from the very coarse experiment L10, the problem is not solely due to low energy at the boundaries. The downscaling performance depends on how inner domain features are forced by the boundary fields. In S10, there is overshooting of energy with respect to truth L2, especially in scales lower than 4 months, indicating instabilities associated with the boundary conditions in the S10 downscaling experiment.

The good agreement between S0 and L2 indicates that there are not errors being introduced to the inner domain by the implementation of lateral boundaries. The significant differences between S10 and L2 suggest that limited representation of the energy field inside the downscaling experiment is due to the lack of resolution in the boundary fields.

In a further analysis we can now focus on a particular peak of energy, trying to understand the features associated with it and how it differs among experiments. Characterized by interesting features observed in Figure 2.7, the next study is intent to two particular peaks: 6 and 4 months. For that, maps of spectrum were created for the respective frequency of each of the peaks. By comparing with truth L2 it is possible to verify if the child experiments are able to reproduce the equivalent features.

In the 4 months peak there is an overshooting of energy by the child S10, both at surface and depth average, and it persists for lower frequencies at surface. Figure 2.8 indicates that experiment L10 is too coarse and the nesting results in propagation of instabilities associated with the lateral open boundaries. Since the cyclonic feature is located next to the open boundary, the misrepresentation of the energy amount and position from the parent results in errors in the child S10.

The same does not occur for the other dynamical nesting strategy, with parent L6 and child S6. In this downscaling approach the ratio in resolution still allows for the correct placement of the western feature, and therefore the resulting S6 is very similar to L2. Hence, the downscaling seems to be working properly in regenerating the small scales.

For the case of parent L2F, very low energy is present due to the filtering. As much of the Northern Adriatic variability is associated to the local atmospheric forcing, the downscaling S2 is capable at recovering considerably the energy not available in the parent L2F. However, when it comes to dynamics which are more dependent on the boundary fields, such as the 4 months peak, the situation changes. At this frequency the lateral boundary conditions are feeding the local cyclonic circulation, and the downscaling in this case was not efficient in regenerating small scales accordingly to truth L2.

The 6 month period eddy variability is clearly not represented by coarse L10, and the map of spectrum (Figure 2.9) confirms the misrepresentation of the eddy field in this parent experiment. We can associate to summer periods where the local radius of deformation is higher; and to the eddies present linked to the western current along the Italian coast. Again the downscaling S6 is in good agreement with truth L2, and at this frequency also S2 and S10 experiments show better results than in the 4 months, for example. Therefore, we can speculate that the EKE is mainly driven by local forcing and less dependent on the lateral open boundaries.

Winds acting on the sea surface have a direct impact on the ocean kinetic energy which is converted from the atmospheric kinetic energy (Ferrari and Wunsch, 2009). In fact, moving the wind stress formulation in the model con-

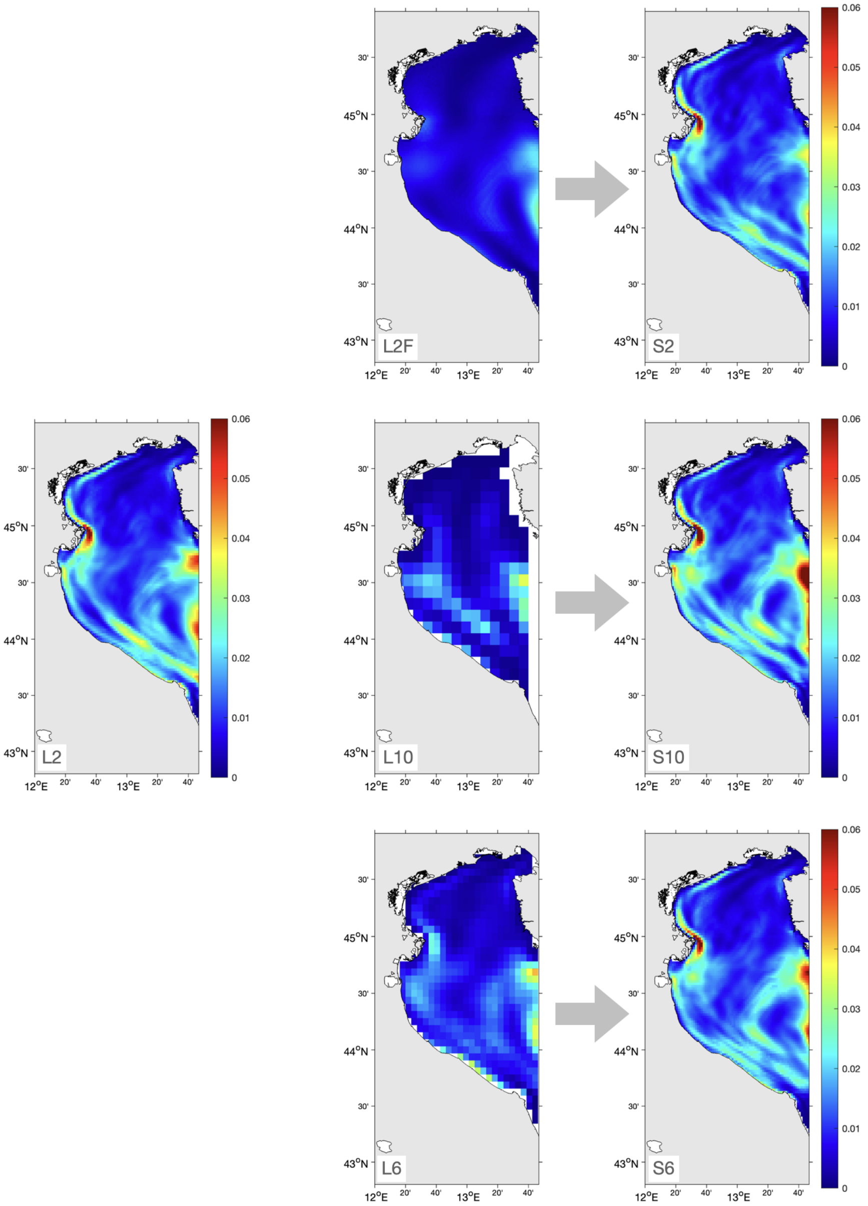

Figure 2.8: Maps of eddy kinetic energy spectrum [$m^2 \, s^{-2}$] associated with the 4 months frequency, for: truth L2 (left); parent (middle) and their respective child (right) experiments. L2 and parent experiments domain was cut to focus on the Northern Adriatic (child domain). Depth averaged fields were used for this analysis.

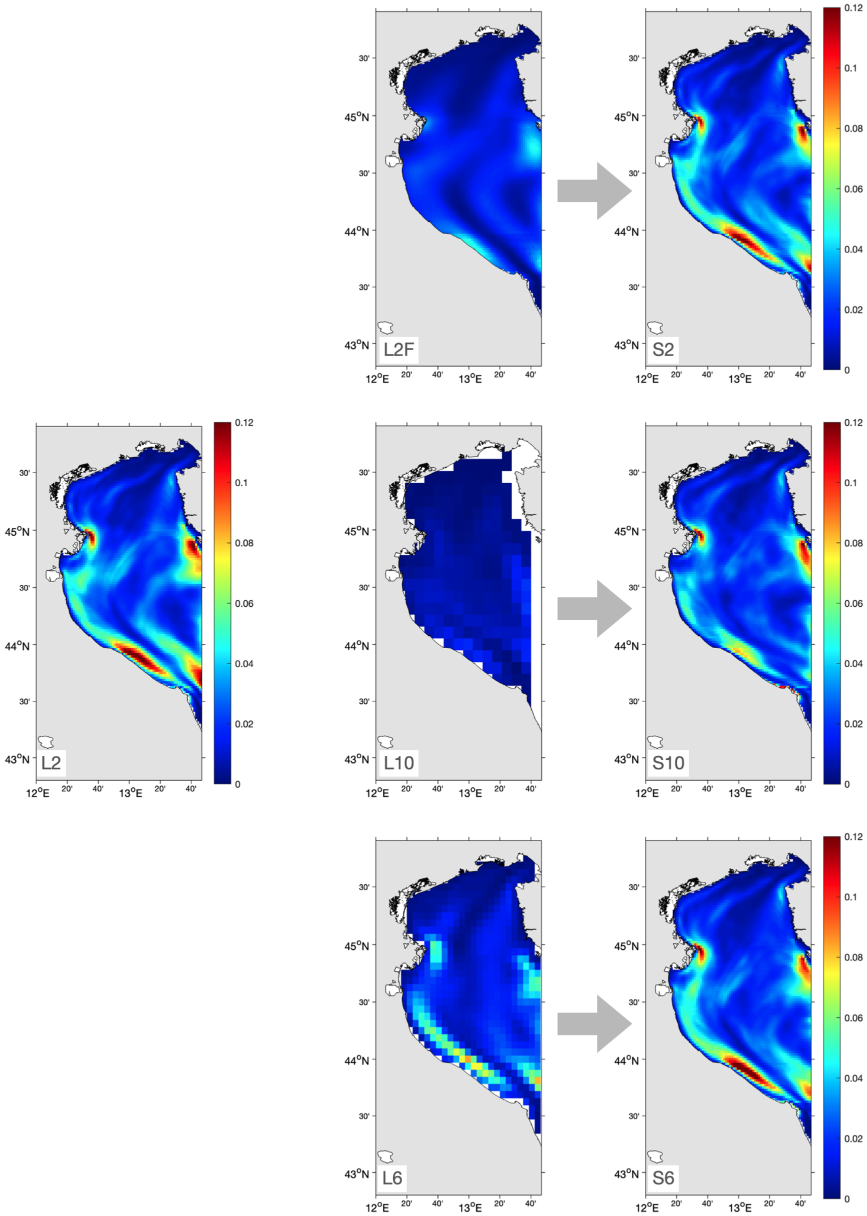

Figure 2.9: Maps of EKE spectrum [$\mathrm{m^2\,s^{-2}}$] associated with the 6 months frequency, for: truth L2 (left); parent (middle) and their respective child (right) experiments. L2 and parent experiments domain was cut to focus on the Northern Adriatic (child domain). Depth averaged fields were used for this analysis.

figuration from relative to absolute wind would result in increase of the overall KE (Munday et al., 2021; Renault et al., 2016, 2020). This was proved in new test experiment with absolute wind configuration, and can be seen in the appendix section in Figure A.3.

Much of the energy in the Northern Adriatic domain, especially at surface, is probably associated to the atmospheric forcing (i.e. winds). It was shown that, when it comes to different horizontal resolution, the ability of coarse model in reproducing the surface energy fields is very limited, even in features which are driven by atmosphere.

We know that sometimes perturbations can be trapped within the domain leading to unrealistic recirculation near the open boundaries. Here our relaxation strength seems to be adequate for allowing the outflow through the south of the lateral open boundary, as can be seen from Figures 2.8 and 2.9. It was seen, however, that energy overshooting occurred for the 4 month period, especially in S1 child experiment (Figure 2.7), and at northern part of the lateral boundary (Figure 2.8), which is mostly associated with inward flow due to the cyclonic nature of the circulation. For this specific time frequency it was identified that parent L10 provides an inflow that is probably unrealistic for the local circulation, and follows a path that is dynamically consistent with the inner domain solution but that diverges from the truth L2. So we can assume that, in this case, the near boundary feature is being “wrongly fed” by the boundary forcing fields.

Future sensitivity tests could be performed regarding the implementation of the lateral open boundary, in terms of sponge zone and relaxation strength. Strong relaxation would be expected to place the outflow consistent with the truth, however it could lead to more unrealistic circulation near the boundaries. Very weak relaxation, on the other hand, can avoid recirculation but could lead to features that are inconsistent with the truth.

Experiment S2, from the filtered L2F, was not capable of recovering the same energy as truth L2. We can possibly accredit this to the filtering applied for creating L2F since the smoothed boundary conditions were not able to sustain the 4 month frequency scales. Interestingly, we were able to demonstrate that a different scenario occurs when using a dynamically generated (i.e. from new modeling experiment) boundary condition strategy with very coarse resolution boundary fields (L10) for the nesting experiment (S1). This high resolution ratio (i.e. 1:5) downscaling strategy in fact resulted in overshooting of energy at this specific frequency, leading to a degradation of the child solution.

We can compare the different outcomes for the nesting strategy of generating S2 from the filtered L2F by exemplifying the two different driving sources for the generation of small scales features in nested domains (Pham and Hwang, 2020). Apparently, for the 6 months frequency, the local stimulating sources prevail, so that even experiment S2, downscaled from smoothed boundary conditions L2F, was able to regenerate the EKE field according to truth L2. We can assume that this frequency is more associated with local driving sources inside the nested domain such as atmospheric forcing (e.g. winds), river, coastlines, etc.

In the 4 month frequency, on the other hand, probably remote stimulating sources, more associated with the information coming from the boundary conditions, prevailed for feeding the inner domain features at this time scale. In this sense, the smoothed solution of L2F was not sufficient to sustain an EKE field of the nested model comparable to truth L2.

2.5 Conclusions

Although it is very important to evaluate the performance of downscaling in regional ocean modelling configurations, we know that it is not always addressed in many studies. Once we are able to target the study to the nesting implementation, it is possible to compare different numerical strategies, quantify possible limitations associated and investigate tailored solutions for our regional climate models.

In a perfect model framework (Figure 2.1), we here propose a large domain high resolution (2 km) experiment, for the entire Adriatic Sea. This experiment, named L2, is considered as our truth reference. Further small domain downscaling experiments for the Northern Adriatic Sea, with the same high resolution as our truth, are performed nested on different parent driving models. The perfect model approach implemented was followed by comparing child small domain experiments with truth large domain L2.

By means of results on kinetic energy and spectral analysis, we could assess the performance of the different nesting strategies for the Northern Adriatic Sea. This study has shown that a ratio in resolution of 1:3 between parent and child is feasible for the representation of the energy structure in the nested domain. Child experiment S6 (2 km) was able to recover the spatial and temporal energy variability in good accordance with truth L2, with significant improvement when compared to parent L6 (6 km), giving confidence about the downscaling strategy.

It was seen that higher resolution jump (1:5), from parent L10 (10 km), resulted in propagation of errors in the downscaling experiment S10 (2 km). Even though lateral open boundaries were provided at a much lower energy than the truth experiment L2, misrepresentation and misplacement of the features at the open boundary resulted in an overshooting of energy in the nested experiment at specific time frequencies. On the other hand, inner domain features more related to the local sources of variability (i.e. atmospheric forcing, coastlines, rivers) were able to evolve and were comparable to the truth L2.

With the set of experiments we were able to demonstrate that the 1:3 ratio of resolution was a proper approach for a dynamical downscaling in the Northern Adriatic Sea reaching the mesoscales. Coarser resolution jump (i.e. 1:5) is found to result in overshooting of the eddy kinetic energy (see Figures 2.6 and 2.7) and misrepresentation of specific features at the inner domain (see Figure 2.8). Although this result concerns the Adriatic Sea domain, previous authors (e.g. Pham et al., 2016; Spall and Holland, 1991; Trotta et al., 2017) have also assumed this as a suitable grid ratio for nested ocean models.

Finally we reinforce the large seasonal variability of our coastal domain and the importance of a high resolution ocean model for representing the local mesoscale features. With the computation of the first baroclinic Rossby radius of deformation (*Rd*), it was also possible to asses the model requirements in terms of spatial resolution for representing the small scales in the Northern Adriatic Sea.

Rd in this shallow region varies significantly throughout the year. During summer, when the vertical profile assumes a stratified pattern, *Rd* reaches large values of approximately 6 km, meaning that our high resolution model (i.e. 2 km) is eddy-resolving. In winter seasons, on the other hand, the mixed vertical profile leads to very small *Rd* of less than 2 km. It is therefore understood that our high resolution model is still at a grey zone from eddy-permitting to eddy-resolving.

3 Reproducibility study for the Adriatic Sea: a physical overview

With the proposed perfect model experiment presented in Chapter 2, we aim at assessing the downscaling performance in the nested domain with respect to well known physical processes occurring in the Adriatic basin. Different than a predictability study, the perfect model approach allows for a “reproducibility” study, which is intended at investigating the capacity of the dynamical downscaling experiment in representing the inner domain processes accordingly to the “truth” experiment L2. In this way, it is possible to demonstrate the strengths and limitations of the downscaling design and implementation of lateral open boundaries.

In the experimental settings described in the previous chapter, the nesting strategy reaching 2 km in the child experiment with a resolution ratio of 1/3 (from 6 km to 2 km) outperformed the one with ratio 1/5 (from 10 km to 2 km) and proved to be an adequate choice for downscaling purposes in the Northern Adriatic Sea. Therefore, in a physical perspective, this chapter will investigate the reproducibility of the child experiment S6 for specific physical processes and extreme events. This investigation is accomplished by analysis of dense water formation and marine heat waves.

3.1 Sea water properties of the Northern Adriatic Sea

Before looking at dense water formation in the Northern Adriatic basin, it is important to understand the preconditioning factors and the sea water properties in the target area, the Northern Adriatic sub-basin. Figure 3.1 contains the monthly mean temperature and the respective anomaly for each experiment, in the Northern Adriatic downscaling domain. The seasonal pattern of the vertical structure is evident from the temperature profiles on the left panels. Anomalies were calculated relative to the annual cycle (right panels), evidencing the interannual variability over these 19 years of experiment.

The seasonality of the temperature profiles is the most evident feature, changing from a stratified pattern in summer-autumn to a vertically mixed water column in winter. Such characteristic is associated with the shallowness of the sub-basin and the predominance of strong and cold wind regime in winter (Artegiani et al., 1997a; Bergamasco et al., 1996; Cushman-Roisin et al., 2013). As discussed in Chapter 2, this seasonal variability over the Northern

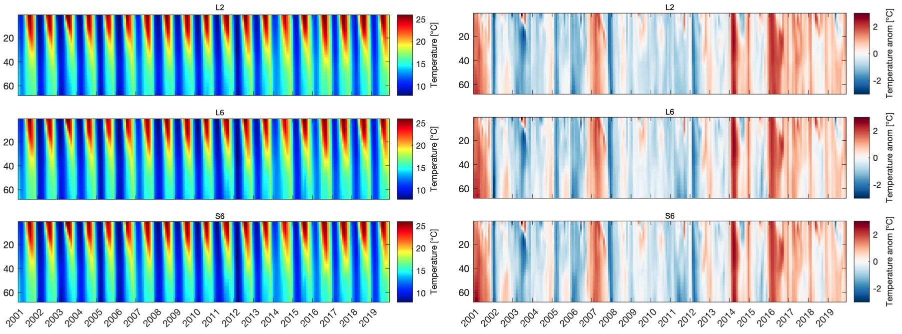

(a) (b)

Figure 3.1: Vertical profiles of temperature monthly mean (a) and anomaly from its annual cycle (b), for truth L2 (top), parent L6 (middle) and child (S6) experiments in the Northern Adriatic area covered by the nested domain.

Adriatic significantly affects the vertical density structure of the water column and the Brunt-Vaisala frequency, leading to time variation of the internal radius of deformation.

The average temperature structure does not differ significantly between the parent experiment L6 and the truth experiment L2. There is, however, an overall underestimation of temperature in the order of less than 1°C, which is also noticeable in the child S6 experiment. Some interannual to decadal variability and a general warming trend in time is also present in all experiments. As would be already expected, average surface temperature is very similar among all experiments due to the same atmospheric forcing. Specific events of extreme temperatures and the reproducibility by the child experiment S6 will be covered in a dedicated section (3.2.4) on marine heat waves.

Looking for the predisposed conditions for increase in water density, favouring water sinking and dense water formation, peculiar years can be listed here. Such years include 2012, well known for strong Bora winds episode and extremely low winter temperatures (Cushman-Roisin et al., 2013; Janeković et al., 2014; Mihanović et al., 2013; Vilibić et al., 2016); 2006 as an extended period of negative anomalous temperatures, with evidence of Modified Levantine Intermediate Waters (MLIW) in the southern sub-basins and large dense water formation in all Adriatic Sea (Oddo and Guarnieri, 2011); and 2008 with significant low temperatures along the entire water column, identified as a year of high production of North Adriatic Deep Water - NAdDW (Cardin et al., 2011).

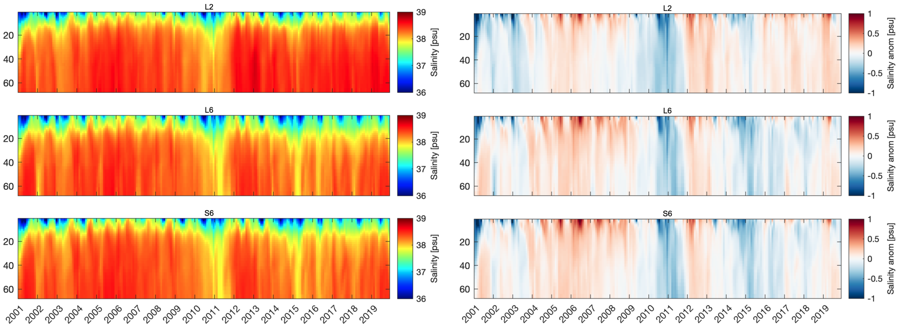

(a) (b)

Figure 3.2: Vertical profiles of salinity monthly mean (a) and anomaly from its annual cycle (b), for truth L2 (top), parent L6 (middle) and child (S6) experiments for the Northern Adriatic area covered by the nested domain.

Within the salinity field (Figure 3.2), the water column structure differs from temperature, and the seasonal shape is not obvious anymore. At this time freshwater input to the basin modulates the vertical profile and there is a clear variability throughout the years. Precipitation but mostly river runoff lower the surface salinity and introduce stratification, creating the so called barrier layer, i.e. a mixed layer shallower than the isotherm, due to the presence of a halocline above the thermocline. A barrier layer in the Northern Adriatic can be easily distinguished by comparing panels (a) on Figures 3.1 and 3.2.

Density profiles (Figure 3.3) give an overview of the dense water variability in the sub-basin and how temperature and salinity are modulating it. The results indicate the importance of low temperatures for the increase in water density during winter and at the specific events (i.e. 2006, 2008, 2012), most frequent at the first decade of experiments. For these particular events the entire water column is dominated by high density values above the threshold. The final years instead are regulated by overall lower densities, much more pronounced in L6 and its child S6.

At a first comparison parent model L6 tends to deepen the fresher water influence to higher depths when compared to L2, and also shows a fresh anomaly in the second decade. In the child S6 the freshwater layer depth is closer to L2, however it is evident that, especially on the second decade, salinity profile tends to follow the parent conditions. Although climatologies of river discharge were used for most of the river catchments, the Po River delta runoff was introduced

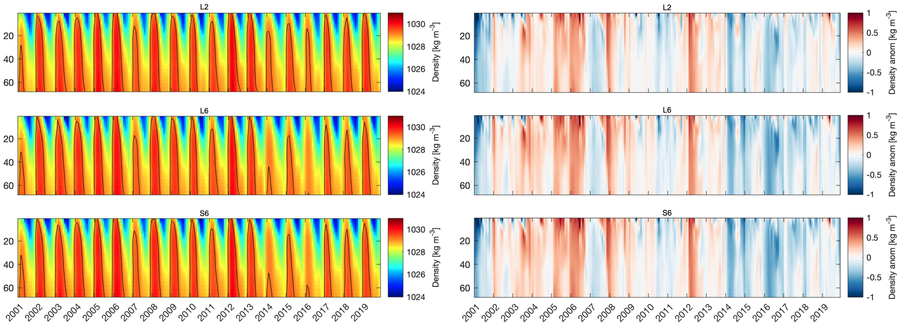

(a) (b)

Figure 3.3: Vertical profiles of density monthly mean (a) and anomaly from its annual cycle (b), for truth L2 (top), coarse L6 (middle) and downscaling (S6) experiments for the Northern Adriatic area covered by the nested domain. Black contour line in left represents the density anomaly of 1029.2 $\mathrm{kg\,m^{-3}}$

to the model from daily observational data. Additionally, a constant salinity is prescribed at river mouths through all years of experiment. Indeed, the variability in the surface fresh water of the northern sub-basin along the years of simulation can be associated with changes in the Po River discharge (Figure 3.4). In Figure B.1 it is clear the overall negative correlation between surface salinity in the Northern Adriatic (demonstrated by truth L2 outputs) and Po River discharge.

L6 underestimate the overall salinity of the basin, and to some extent this information advances from the boundaries to the nested domain. It becomes clear that the freshening on the basin that we observe in parent L6 and child S6 is not only modulated by the local atmospheric forcing (e.g. heat loss and wind outbreaks as in 2002, 2006, 2008 and 2012) and rivers (e.g. high runoff in 2003, 2009, 2011 and 2013-2015) anymore, but relies on the remote salinity properties of the parent model. All three experiments (i.e. L2, L6 and S6) have the same atmospheric forcing conditions imposed, which suggests that the inner circulation features are being misrepresented by the L6 model dynamics (covered in more details in the next sections).

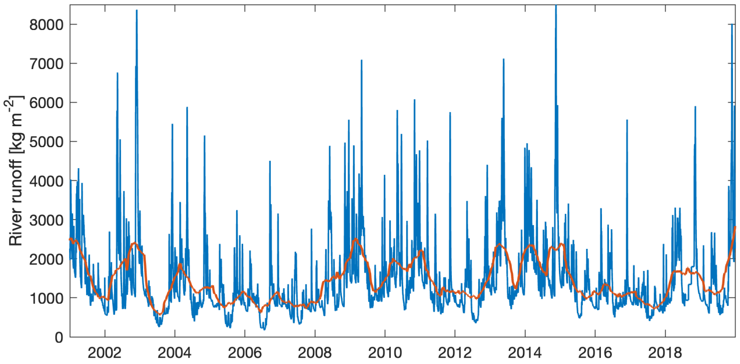

Figure 3.4: Daily river runoff for Po River based on observations from the Pontelagoscuro station, located 40 km upstream of river mouths. Red line corresponds to a running average with 180 days window.

3.2 *What is the reproducibility for selected physical processes and extreme events?*

3.2.1 Dense Water Formation

The first study of reproducibility that will be covered in this section is here presented by analysis of dense water formation in the Northern Adriatic. Dense water volume for each Adriatic sub-basin was calculated based on a potential density anomaly threshold for newly formed dense water (NAd: $\sigma_t > 29.2$ $\mathrm{kg\,m^{-3}}$, MAd: $\sigma_t > 29.2$ $\mathrm{kg\,m^{-3}}$, SAd: $\sigma_t > 29.0$ $\mathrm{kg\,m^{-3}}$), following Artegiani et al. (1997a), Janeković et al. (2014), and Vilibić et al. (2016).

The choice of about 2 km horizontal resolution (in L2 experiment) and a fine vertical discretization (equal for all experiments) is foreseen to accurately represent the dense water dynamics in the sub-basins. It is important to acknowledge that, from a total of 120 z-levels for the entire model domain (maximum depth approximately 2500 m at the southernmost area covering the Ionian Sea), the shallow waters of the Northern Adriatic sub-basin (maximum depth of 75 m) account for a reduced but still significant number of 35 vertical layers. This is a result of unevenly spaced z-layers with higher resolution at the top levels, expected to better resolve the mixing and stratification processes in the Northern Adriatic Sea. Moreover, the vertical configuration with partial steps contribute to a better representation of the bathymetry and bottom dynamics.

The horizontal resolution, on the other hand, differ between experiments. Not only the better capacity in resolving the smaller scale dynamics inside the domain, the increase in resolution may also contribute to a more accurate representation of dense water deposition and pathways inside the modeled domain (Pranić et al., 2023). In the Northern sub-basin, as the Rossby radius of deformation is lower than 2 km in most of the area during winter and spring, when dense waters are generated and spreading, the chosen resolution is in a "grey-zone" for solving the mesoscales and we could be, eventually, partially misrepresenting the dense water dynamics. However, the aim here is to evaluate a methodological approach for dynamical downscaling having L2 as benchmark. The ability of the child experiment S6 to correctly represent the dense water production is thus assessed by comparison with the truth L2.

Figure 3.5 shows the volume, temperature and salinity of dense water computed for each of the experiments in the Northern Adriatic, the same area covered by the child experiments. The frequency of variability in dense water volume follows the seasonal pattern of the density field for this region, mainly related to the decrease in temperature in winter. As previously mentioned, dense water production in the Northern Adriatic is associated with the significant heat loss during winter, enhanced in the presence of strong and/or persistent Bora winds event (Cushman-Roisin et al., 2013; Vilibić and Supić, 2005). The year of 2012, for example, is well know for high volume of dense water observed especially in the northwestern shelf, triggered by a long lasting Bora event (Cushman-Roisin et al., 2013; Mihanović et al., 2013). This year of exceptional cold temperatures and dense water formation in the Northern Adriatic was well captured by the experiments.

Together with the seasonal shape in dense water volume, a lower frequency variability is present in the Adriatic Sea. A multi-annual fluctuation is also evident in the basin, mostly through the dense water salinity time series in Figure 3.5. Interestingly, this variations are not equally represented among the experiments, and reveal different capability to represent the mechanisms influencing the dense water formation.

In the first decade of experiment, dense water production is triggered by low temperature episodes, well captured by both large domain experiments (L2 and L6), resulting in large dense water volume which saturates the volume of the Northern Adriatic sub-basin. Slight underestimation of dense water volume by parent experiment L6 is subsequently overcome by the child experiment S6, indicating that downscaling accounted for a correct representation of the dense water computation in the sub-basin.

After 2011, dense water formation in the Northern Adriatic reduces. The

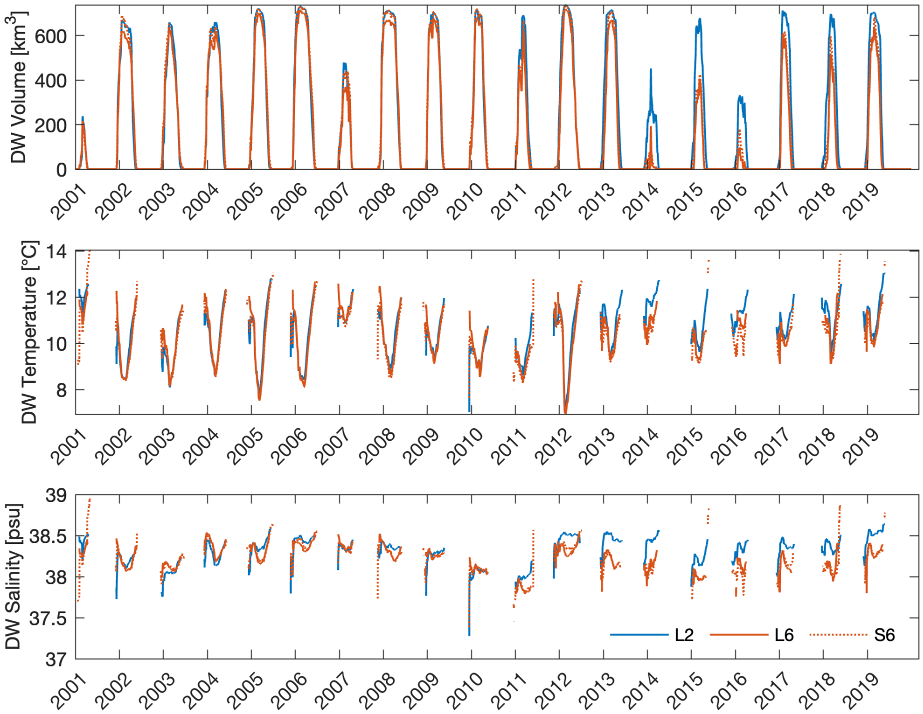

Figure 3.5: Dense water volume (top), dense water temperature (middle) and dense water salinity (bottom) computed for each experiment for the area covered by the nesting experiments in the Northern Adriatic Sea. Solid and dashed lines represent, respectively, large domain (entire Adriatic Sea) and downscaling (Northern Adriatic) experiments.

dense water modulation corroborates to the overview of the vertical profiles from the previous section. Interestingly, salinity between L6 and L2 diverge considerably in the last decade, giving space to some speculations regarding the processes behind density modulation in the region.

As known from literature, atmospheric forcing (i.e. wind stress and evaporation) is the main driver for dense water formation in the Northern Adriatic. Until 2013 the child experiment S6 is capable in reproducing dense water volume comparable to the truth L2 and most of it can be associated to the drops in temperature seen in Figure 3.5.

The process of dense water formation through cooling of waters is again well exemplified by the 2012 case. This year was characterized by strong and cold Bora wind events and therefore high volume of dense water was observed in the Adriatic Sea in winter, especially in the northwestern shelf (Cushman-Roisin et al., 2013; Mihanović et al., 2013). Despite the salinity discrepancies between large domain L2 and L6 experiments, dense water volume was similar for both cases due to the very low temperature as main driver. Reproducibility of dense water events thus has shown to be high under local atmospheric preconditioning factors.

In the second decade, however, a different scenario arise where salinity diverges considerably between L2 and L6, as well as the dense water volume. From 2014 onward the dense water formed by the child experiment S6 is also lower than L2, indicating that a different mechanism is affecting the reproducibility capability of the downscaling strategy in the two distinct periods. The last period was characterized by higher density stratification, and under this condition, salinity seems to play a more significant role in the dense water dynamics of the basin. The discrepancy between the parent L6 and the truth L2 experiments is not fully recovered by the downscaled S6, which instead tends to follow the characteristics of its parent L6.

It can be assumed that, in addition to the local atmospheric condition, an external component is also shaping the dynamics for dense water formation. It becomes clear that reproducibility of child S6 is dependent on the water mass properties that enter the nested domain from the lateral open boundary. The limitation of L6 in correctly representing the density profile in the Adriatic Sea is propagating to the nested S6. Even though the internal dynamics of the downscaling experiment was able to evolve and small scale features were regenerated inside the nested domain, the characteristics of salt content of water mass entering through the boundaries from the parent L6 conditioned the stratification in the child experiment S6 as well.

The fact that the pictures in Figure 3.1 are almost equal while pictures in Figure 3.2 differ confirm the fact that the temperature variability is locally driven, while the salinity variability is remotely driven. Thus the dense water formation triggered by temperature drops are well captured by child S6, while dense water triggered by salt inflow from southern regions are missed.

In Appendix B dense water analysis is performed for all experiments proposed in Chapter 2. As a control framework, either in S0 and S2 (nested experiments from parent L2 and L2F, respectively) the dense water volume computed is the same as the truth L2. These experiments prove that the misrepresentation of the sea water properties in the child experiment are related to weaknesses of parent L6, but not to the downscaling experiments and implementation of lateral open boundary conditions.

We observe that the reproducibility of the Northern Adriatic dense water formation in a dynamical downscaling exercise depends on the capability to properly represent both the local drivers at the air-sea interface (heat losses, wind stress, low runoff) and eventually the remote ocean driver entering through the lateral open boundary (i.e. the salt water inflow). Eastern or western Mediterranean Sea waters entering the Adriatic Sea from the Ionian region play an important role in the modulation of the local thermohaline properties, mainly for the Southern sub-basin.

The perfect model approach underscores that when the Northern Adriatic dense water formation is triggered by local drivers, the child experiment successfully reproduces the truth experiment. Conversely, when the remote driver is playing a role but it is missed by the parent model, the child model fails the reproducibility of local dense water.

The following chapters are then dedicated at investigating the overall contribution of this remote drivers to the Northern Adriatic properties and consequently dense water computation. Directing interest to the large domain experiments L2 and L6, we will be able to investigate this interannual to decadal variability and the limitations of L6 in correctly representing the salt water inflow.

3.2.2 Looking at the “bigger picture”: The entire Adriatic Sea

Limitations on the downscaling experiment S6 were found to be associated with the misrepresentation of water mass properties in its parent model L6. This is

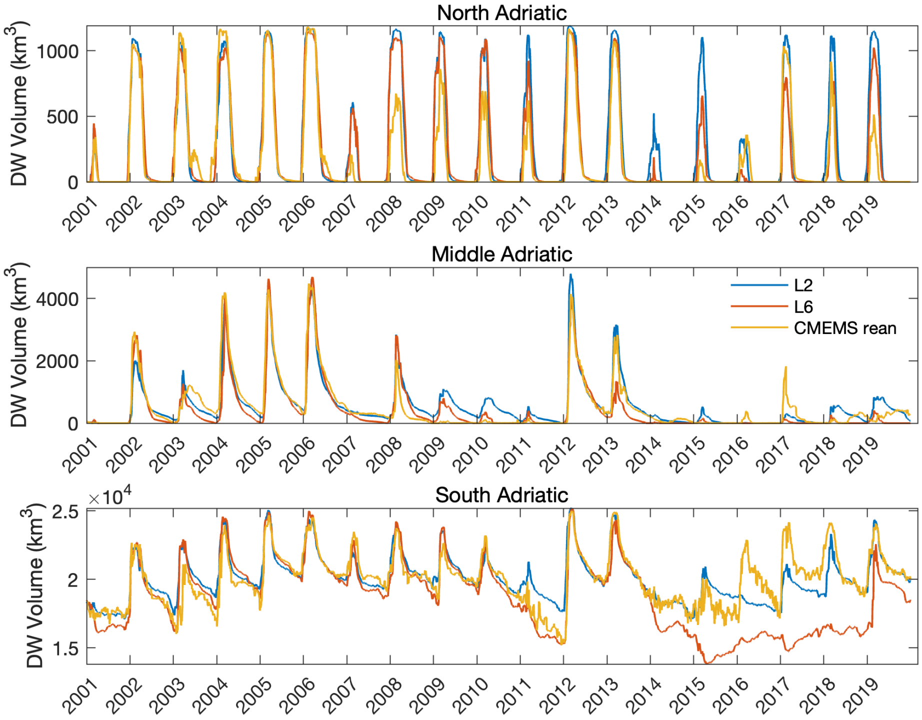

Figure 3.6: Dense water volume computed for each large domain experiment (L2 and L6) compared with reanalysis data, for the three Adriatic sub-basins. The potential density threshold is 29.2 $\mathrm{kg\,m^{-3}}$ for Northern and Middle Adriatic, and 29.0 $\mathrm{kg\,m^{-3}}$ for Southern Adriatic.

also evident from the multi-annual variability seen in the dense water formation in the Northern Adriatic Sea. In order to understand the mechanisms associated with this thermohaline variability and the consequent changes in model reproducibility, Figure 3.6 contains the dense water volume computed for all Adriatic sub-basins, in each large domain experiment (L2 and L6) together with reanalysis data (CMEMS). Delimitation of the sub-basins for the dense water computation in the large domain experiments can be found at the appendices in Figure B.2.

It is clear the seasonal pattern of dense water formation in the Northern Adriatic, associated with temperature drops in winter. Although there is the presence of the seasonal cycle in the other sub-basins, other frequencies of variability affect the water mass properties. Different than the Northern Adriatic, the seasonal variability of dense water in the Southern basin creates a particular shape with rapid increase in volume in winter and slow decrease towards lower values in the following seasons.

The sudden increase in density and consequently dense water volume in the southern sub-basin is probably due to the intrusion of dense water from the northern sub-basins followed by mixing process that create a slower gradual decrease in density (Querin et al., 2016). Moreover, the Southern Adriatic dense water is also highly sensitive to the thermohaline characteristics of the water mass that is entering the basin from the south, especially the amount of Levantine Intermediate Water - LIM (Gunduz et al., 2013).

At a much lower frequency, a quasi-decadal pattern in dense water can be noticed for the Southern Adriatic (bottom panel of Figure 3.6). This variability resembles the multi-annual oscillation in salinity and temperature that was also present in Figure 3.5. Interestingly, the last decade is a period of high discrepancies in dense water volume between coarse (L6) and high resolution (L2) experiments. The different representation of this physical process by the experiments in the southern basin suggests that the external contributor to the multi-annual variability of sea water properties in the Adriatic Sea is predominant in the southern sub-basin.

Figure 3.7 contains the temperature and salinity of the computed dense water volume by the different experiments for each Adriatic sub-basin. Again the major differences between experiments L2 and L6 are in the Southern Adriatic Sea: they start to deviate after a few years of simulation with an underestimation of both salinity and temperature by coarse L6. However, it is after 2012 that the discrepancies become even more pronounced. From this specific year there is a significant increase in salinity and temperature in "truth" L2, in accordance to what is also seen in the reanalysis data. Different than the previous period of simulations, the last few years correspond to an overall increase in the basin temperature and salinity, which is probably explained by a prevailing role of the inflow of salt and warm Modified Levantine Intermediate Water (MLIW) from the Ionian Sea towards the Adriatic basin.

As an attempt to understand the processes behind the differences between experiments, a set of analysis was performed in time. The first one is a time series of the basin average salinity of the Northern Adriatic sub-basin (Figure 3.8), which can also support the results on dense water formation in the Northern Adriatic Sea. We continue here the discussion with focus on the reproducibility study by comparison between the different model's result. Further discussion by comparing our model outputs with observations will be covered at a validation

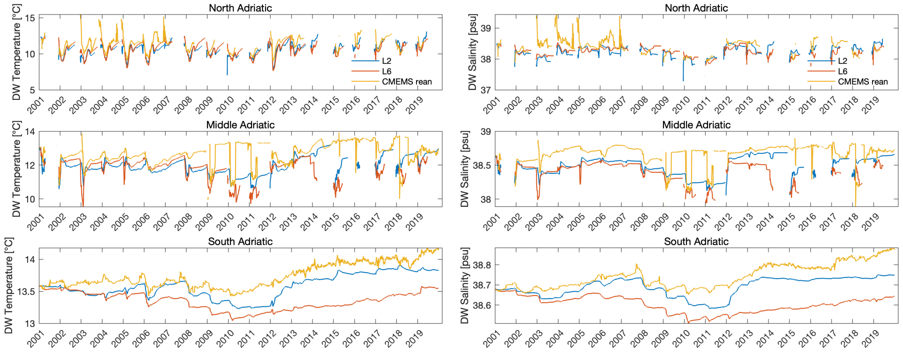

(a) (b)

Figure 3.7: Dense water temperature (left) and salinity (right) for "truth" L2 and parent L6 experiments, compared with reanalysis from CMEMS.

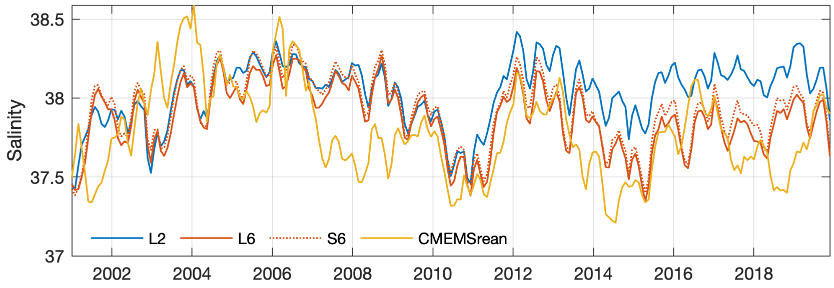

Figure 3.8: Basin average salinity [psu] for three different experiments ("truth" L2, parent L6 and child S6) and CMEMS reanalysis, computed for the area covered by the downscaling Northern Adriatic sub-domain. Solid and dashed lines represent, respectively, large domain (entire Adriatic Sea) and downscaling (Northern Adriatic) experiments.

section at the end of this chapter.

Figure 3.8 also confirms a freshening of L6 experiment after 2011 with respect to L2, that is transferred through the boundaries to the downscaled S6. Considering that both large domain experiments (L2 and L6) have the same atmospheric forcing fields, lateral open boundary conditions and river inputs, the differences in salinity in the Northern Adriatic among experiments is due to a misrepresentation of the inner domain circulation by the coarse model L6.

In order to understand the reason of the L6 discrepancy on the second decade (2011-2019), seasonal transects along the Otranto Strait were performed for each experiment (Figure 3.9). The water exchange at the Otranto Strait is dominated by water inflow on the eastern side and outflow on the western side (Ferentinos and Kastanos, 1988; Zavatarelli and Pinardi, 2003). This narrow passage is the only communication between the Adriatic Sea and the entire Mediterranean, and therefore its accurate representation by the ocean model is crucial for correctly accounting for the water mass exchange between the Adriatic and the Ionian. Delimitation of the Otranto Strait can be seen in Figure 1.1.

Due to the average heat loss that prevails in the Adriatic Sea, the Otranto Strait has a significant role in heat storage of the basin through the transport of heat from the Ionian Sea (Artegiani et al., 1997a). With the large freshwater influence from river runoff that characterizes the Adriatic as a dilution basin (Artegiani et al., 1997a; Verri et al., 2018), the strait is also essential for the salt exchange with the Mediterranean Sea. A fresh water bias has been reported by Oddo et al. (2005) in their numerical model and one of the causes was associated to the misrepresentation of saltier waters entering from the Ionian Sea with eastern Mediterranean origin.

Some important features of dense water masses are expected to be seen along the section of the strait: outflow of dense water originated from the cooling of the Northern Adriatic shallow waters (NAdDW) and the Adriatic Deep Water (ADW) produced in the southern sub-basin. On the western shelf there is an outflow of fresh water with Adriatic characteristics that is compensated by the eastern inflow of saltier waters coming from the Ionian Sea. The entrance of relative saltier water inside the Adriatic Basin is known to be associated with a dipole of surface circulation in the Ionian Sea, that will be explored in the next section. The phases of the dipole favours the entrance of western waters with Atlantic Ocean influence or eastern waters with Levantine Basin characteristics.

The vertical salinity and meridional velocities structures already differ quite significantly among experiments. There is well defined intrusion of saltier water at approximately 150-400 m depth in L2 which is not properly represented in L6. These profiles in L2 have the clear shape and salinity values of the intermediate waters with Levantine basin origin (MLIW), that enter the Adriatic Sea mainly during the cyclonic phase of the Adriatic-Ionian Bimodal System (BiOS). The intrusion of these warmer and saltier waters explain the increase in temperature and salinity in L2, as it was seen in Figure 3.7, causing the changes in dense water volume and properties inside the basin.

From the vertical transects along the Otranto Strait we can investigate how the horizontal resolution of the model interferes in the correct representation of the local density driven circulation. This very narrow passage that has to allow for the outflow of waters from the Adriatic Sea in the west and inflow of

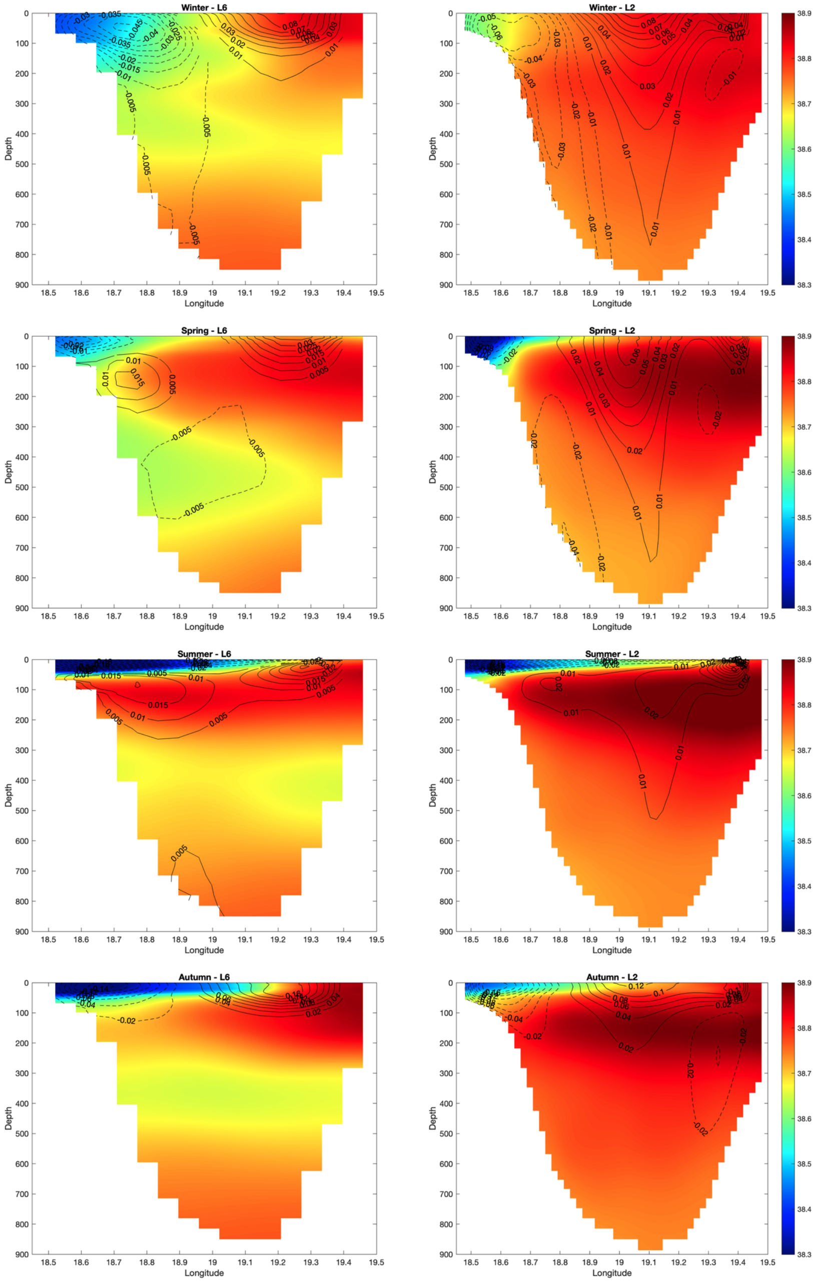

Figure 3.9: Seasonal transects for salinity [psu] (shaded) and meridional velocity [$m^2\,s^{-1}$] (contour) along the Otranto Strait during the period 2011-2019, for coarse L6 (left) and “truth” L2 (right) experiments.

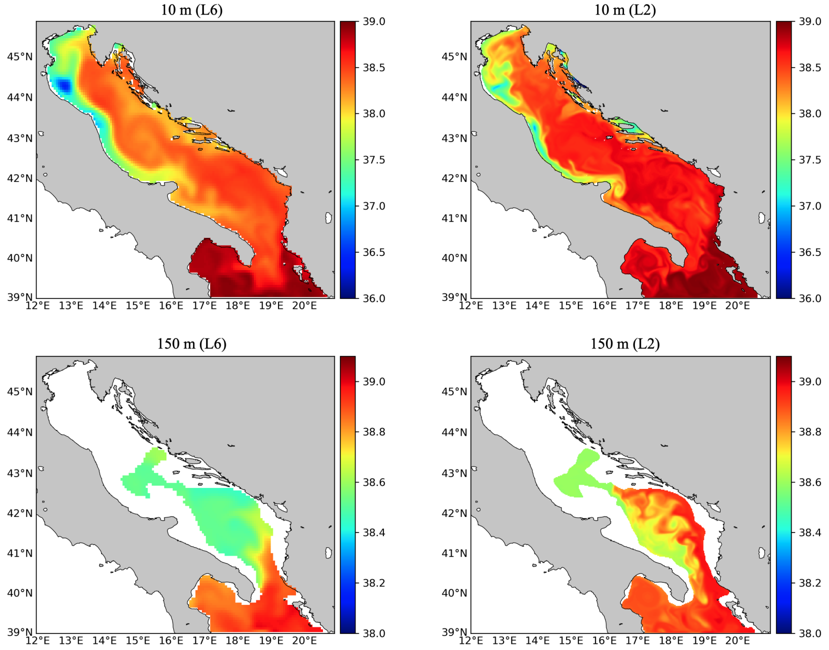

Figure 3.10: Maps of salinity [psu] at 10 m (top panels) and at 150 m depth (bottom panels) for coarse L6 (left) and "truth" L2 (right) at a daily output in 21/06/2012. (Updated color bar with depth)

waters from the Ionian Sea in the east. The coarse resolution in L6 seems to be a limiting factor for the inflow-outflow dynamics. Even with the same high vertical resolution in both experiments (L2 and L6), the strait is very narrow and the topography remains in a "step-like" representation in L6.

From daily outputs we can have a clear picture of how the Adriatic Sea circulation is being reproduced by each experiment. Comparison of salinity fields at 150 m, depth of MLIW entrance, is performed in Figure 3.10 for the beginning of summer 2012. The low horizontal resolution of L6 limits the representation of the meandering structures that are clearly reproduced by L2 and contribute to the advection of saltier waters inside the Southern Adriatic. With a radius of deformation not lower than 6 km (Figure 2.3), the circulation mechanism between Northern Ionian and Southern Adriatic is well resolved by the "truth" L2 model.

It is clear that the coarse model L6 is not capable of representing the thermohaline circulation especially along complex coastline features, affecting the distribution of salt and heat across the basin and, consequently, the dense water formation. Moreover, the high resolution model L2 resolves inner domain circulation and dynamics, probably contributing to water masses exchange along the Otranto Strait. This can be seen by the near surface salinity maps in Figure 3.10 and also from kinetic energy and vorticity fields in Chapter 2. In a narrow, attached to the Italian coast feature, a western current is able to carry northern fresh water southwards, leaving the Adriatic basin through the Otranto Strait. L6 model, on the other hand, due to its low resolution produces a fresh water plume that expands towards the inner domain. The model in this case is unable to properly resolve this western feature associated with a very low radius of deformation of this western feature. Without the strong western freshwater outflow, the model is probably limited in correctly representing the entrance of southern saltier waters likewise.

In general, this multi-annual pattern in salinity variability at the basin can actually provide some answers, or at least bring upon new intriguing questions regarding the variability of the sea water properties in the Adriatic. The next section is thus devoted to analysing the variability mode that affects the circulation at the Ionian-Adriatic region, influencing the water mass properties in the Adriatic Sea.

3.2.3 Interannual thermohaline variability in the Northern Adriatic Sea

Temperature and salinity variability in the Northern Adriatic may vary depending on a series of local or remote drivers under different time scales (Vilibić et al., 2020). The net heat flux at the air-sea interface is the most important contributor for the temperature modulation. River runoff is an important local driver for salinity variability, however such changes may also be associated to remote patterns including the Ionian Sea circulation regime.

Considering that the experiments proposed in this thesis follow a methodological approach for downscaling studies, the obtained results allowed also to derive some straightforward conclusions on the proper way to reproduce the Adriatic Sea dynamics and dense water formation. To support the speculation on the crucial role of the horizontal resolution with respect to the model capability to represent the thermohaline variability of the water masses entering the Adriatic Sea through the narrow Otranto Strait from 2001 to 2019, time series of average salinity and temperature at a zonal section of the southern boundary connecting the Adriatic domain with the Ionian Sea can be found in Figure 3.11.

There is an already known multi-annual pattern in the Adriatic Sea sea thermohaline characteristics associated with the Northern Ionian Gyre (NIG). Near surface circulation in the Ionian Sea determines the proportion of water masses that will enter the Adriatic Sea, whether from western (i.e. Atlantic Ocean) or eastern Mediterranean (i.e. Levantine basin) characteristics. It has been proposed a feedback mechanism between the upper ocean circulation in the Ionian sea and dense water formation in the Southern Adriatic Sea, called the Adriatic-Ionian Bimodal Oscillating System - BiOS (Gačić et al., 2010).

From the material discussed in the previous section, we can already associate the interannual to decadal changes of salinity and temperature observed for the Adriatic with the shifts in the Ionian circulation. The southern open boundary of the large domain experiments cover part of the northern Ionian Sea, and the average fields in Figure 3.11 can give an indication of the thermohaline variability in this region.

Dense water formation in the Southern Adriatic seems to follow this multi-annual variability of water mass properties in the Adriatic-Ionian site. From 2001 to 2005, the warmer and saltier waters present at the southern boundary (Figure 3.11) and overall increase in dense water formation in the Southern Adriatic sub-basin (Figure 3.6) could indicate a cyclonic phase of the NIG, with

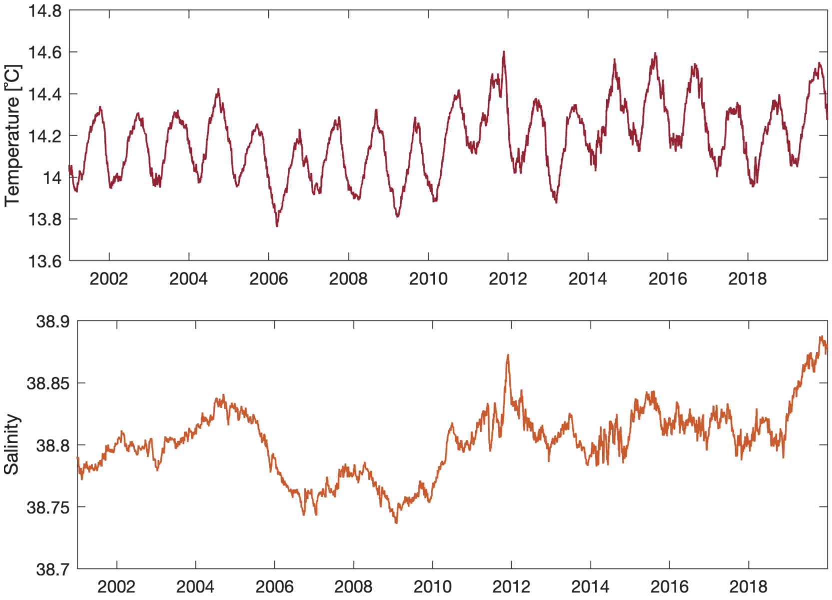

Figure 3.11: Mean salinity and temperature at a zonal section at 39°N which are based on CMEMS reanalysis and correspond to the time series provided at the southern open boundary of the parent L6 experiment. The Otranto Strait is 2° north of this open boundary.

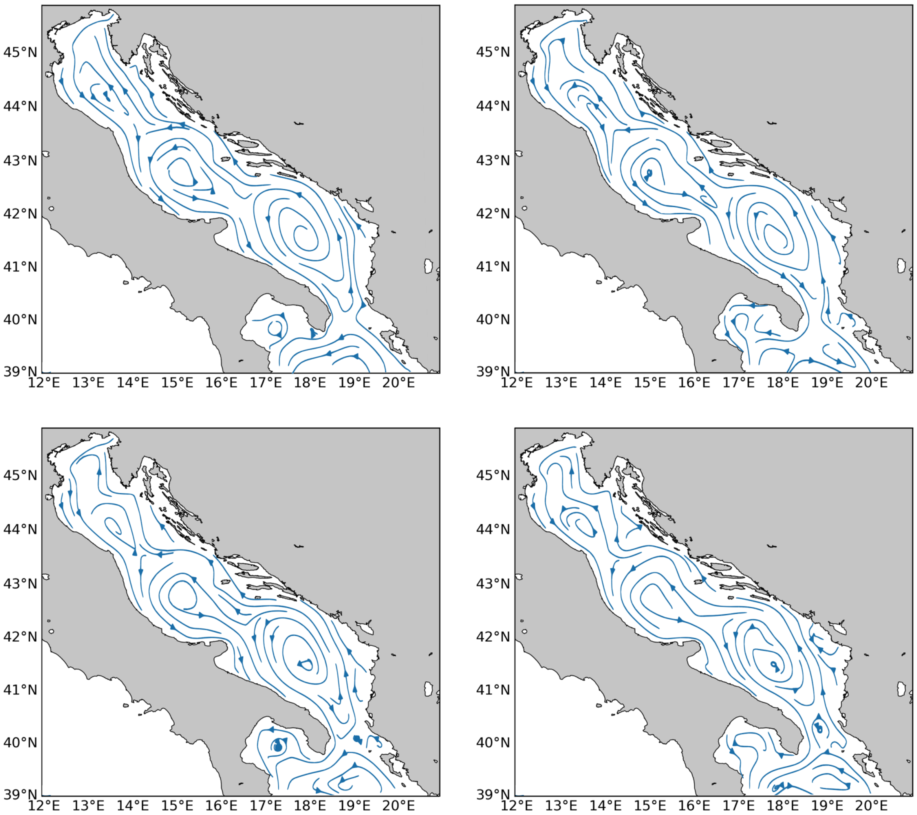

Figure 3.12: Mean surface circulation for period 2001-2005 (top-left), 2006-2010 (top-right),2011-2015 (bottom-left) and 2016-2019 (bottom-right) obtained from L2 experiment.

waters from the Levantine Basin entering the Adriatic. Indeed, for this respective period composites of surface circulation (Figure 3.12) indicate that cyclonic circulation is predominant in the northern Ionian Sea, even if the computational domain does not cover the Northern Ionian Sea south of 39 °N. Pinardi et al. (2015) have also identified a cyclonic near surface circulation for the same period, which according to the authors started in 1997.

For the period from 2006 to 2010, however, the overall decrease of the Southern Adriatic dense water (Figure 3.6) and lower temperature and salinity at the southern open boundary (Figure 3.11) suggest the reversal to an anticyclonic phase. This is confirmed by the surface circulation maps (Figure 3.12). In fact, this short period of anticyclonic phase have been identified before (Denamiel et al., 2022; Gačić et al., 2010). This clockwise circulation phase is associated with the presence of a northward meander of the Atlantic Ionian Stream (AIS) that brings less saline waters to the North Ionian sea (Borzelli et al., 2009; Pinardi et al., 2015).

The first ten years of experiments seem to reproduce well the variations in the thermohaline properties in the Adriatic Sea and its association with the shifts in the NIG. However, for the second period (2011-2019) the circulation reversal is not so trivial in all experiments. Eusebi Borzelli and Carniel (2023) actually understand the BiOS cycle as a damped oscillation, with a damping time of approximately 11 years. The authors sustain that the BiOS was damped to nearly disappearing, followed by a revitalization phase that would have started in 2017.

In our experiments there is evidence of a reversal to a cyclonic mode around 2011-2012, contributing to the entrance of saltier waters from the eastern Mediterranean to the Adriatic Sea. Such process, as previously seen, was not correctly captured by the coarse model L6 specially along the Otranto Strait (Figure 3.10), causing the lower salinity at the basin with respect to L2. Mesoscale eddy activity is actually quite significant during the NIG transition phase period, and can even cause uncertainties in the timing of reversal (Gačić et al., 2014; F. Liu et al., 2022). We can presume that the lack of resolved mesoscale features in L6 probably contributed to the limitations in reproducing the processes associated with the BiOS inversion when compared to L2.

2012 is known to be a year of very low temperatures in the Adriatic Sea, with a sudden increase in dense water volume well captured by the truth L2 experiment (3.5). Northern Adriatic dense water formation in 2012, however, was dominated by the local atmospheric process and heat loss, and did not differ between experiments. In the following years instead, with no significant cold winds outbreaks and an overall warmer sea water, Northern Adriatic dense waters apparently were more impacted by the intrusion (or lack of intrusion in L6 case) of the saltier waters coming from the Levantine basin.

2012 is a very peculiar year due to the extreme winter conditions, but also with respect to river runoff. Specifically for this year Po River runoff was significantly low (see Figure 3.4), that contributed to increase in salinity in the Northern Adriatic. This year also follows and is followed by a period of opposite salinity conditions in the sub-basin, with large discharge from Po River.

Different authors have tried to understand the mechanisms associated with the BiOS regime (Borzelli et al., 2009; Denamiel et al., 2022; Gačić et al., 2021;

F. Liu et al., 2022). There are mainly two theories for the reversal of the NIG: the first one is associated with internal dynamics due to the outflow of very dense water from the Southern Adriatic Sea (Gačić et al., 2010; Gačić et al., 2021; Rubino et al., 2020); the second one is more related to the wind stress curl effect (Eusebi Borzelli and Carniel, 2023; Pinardi et al., 2015).

Gačić et al. (2014) proposed a theory for shift of BiOS mode due to extreme dense water formation event such as the one in 2012. From a laboratory experiment it was proven that local mechanisms as extreme dense water formation and outflow could trigger inversion in circulation (Gačić et al., 2021). Years later, however, Eusebi Borzelli and Carniel (2023) brought evidence that such event itself was not capable of ensuring the shift in the Northern Ionian circulation from cyclonic to anti-cyclonic. The authors instead support the relevance of the wind stress curl effect on the inversion of the Ionian Sea circulation, supporting the idea that winds rotating in the same direction may provide the necessary energy and momentum to create changes in the sea surface height.

The limitations in L6 experiment, i.e. the problems in representing the complex coastline dynamics under a low resolution configuration, actually led to a pertinent question: *Are the BiOS effects on the NIG able to influence the shallow northern Adriatic?* This study could bring evidence of the influence of shift in phases of the BiOS mode and dense water volume formed in the Northern Adriatic. From our results, we could speculate that the circulation in the Ionian Sea and shift in the BiOS phase is also capable of influencing the Northern Adriatic properties and consequently its dense water formation.

In scenarios of strong winds and cold winters, local atmospheric conditions were the most important driver in conditioning dense water formation in the Northern Adriatic Sea. Under this situation, reproducibility is high and the child experiment S6 was capable of correctly representing the dense water volume. However, under warmer conditions with overall higher temperatures and less Bora winds outbreaks, together with a shift to cyclonic phase of the BiOS regime, the remote drivers start to become more important. In this situation, the ability of the parent model of representing the thermohaline circulation entering the Northern Adriatic is crucial for the proper representation from the downscaling experiment too.

3.2.4 Marine Heat Waves

This section will focus on a reproducibility study in terms of extreme events, i.e. marine heat waves (MHW). MHW mean and maximum intensities have increased in all Adriatic sub-domains during 2001-2010, with increase in duration and number of events over 2012-2020 (Hobday et al., 2016; Juza et al., 2022). With considerable high maximum intensity values, the Northern Adriatic can be considered a hot spot for MHW detection in the Mediterranean Sea. With this study we wish to explore the capability of the downscaling experiment S6 in correctly reproducing such important events, having again truth L2 as reference, and evaluate the possible gains when compared with parent L6.

Associated with anomalous warming conditions, MHW can be triggered by local processes, large-scale climate modes and teleconnections (Holbrook et al., 2019). MHWs are strongly modulated by the local atmospheric forcing, when processes such as warm surface air temperatures and reduced wind stress can contribute to anomalous warming of the ocean. Although they are mainly associated with atmospheric forcing, ocean processes and circulation also play a role in the local temperature modulation (Oliver et al., 2021). Horizontal and vertical advection of heat and mixing processes can be associated to the generation and duration of the MHWs.

The main definition of MHW has been proposed by Hobday et al. (2016), and are characterized by anomalous warm ocean temperatures lasting for prolonged periods of time. The way MHW are computed is based on a statistical decomposition of temperature time series, in which it is defined a baseline period (e.g. climatology) and a threshold value (i.e. 90^{th} percentile in this study). Episodes of temperature anomalies above this threshold and lasting for at least 5 days are then classified as MHW.

Different approaches have been proposed for defining this baseline, being either fixed or variable (e.g. Oliver et al., 2021; Rosselló et al., 2023). By using a fixed baseline we are not accounting for the possible trend in time that the temperature might present. We can assume that there is no right or wrong method, and the choice in reality depends on the purpose of the study. Thinking on an impact study, for example, it is interesting a fixed baseline, in which it is important to keep the trend (e.g. warming) to understand the possible consequences of that. On the other hand, if there is an already known trend and it is wanted to investigate specific events and how extreme they are when compared to the overall average warming, it might be useful the choice for a moving baseline.

In this study, as seen in Figure 3.1, there is a clear warming trend in the Northern Adriatic basin. To some extent we could possibly associate it to the overall global warming trend. However, as it was also covered in the previous section, the Adriatic Sea thermohaline conditions are highly influenced by interannual variability and shifts in the Ionian circulation. There is a clear change in the Adriatic basin in the two decades of experiments between 2001-2019. Therefore, for this specific study it was opted for a fixed baseline for the MHW computation, to enhance the peculiarities on sea water temperature for each period and their representation by the different experiments.

The analysis was performed for the Northern Adriatic Sea for truth L2, parent L6 and child S6, for the region covered by the downscaling domain. The computed baseline for the MHW detection is the climatology of the entire 19 years (2001-2019), calculated for each of the experiments, with a 90^{th} percentile as threshold. Following the proposed perfect model framework, the MHW events identified in L2 are then considered as the truth anomalous events for the Northern Adriatic. By comparison with our truth reference we can assess the ability of the downscaling experiment in reproducing these events.

Figure 3.13 contains the mean intensity of MHW events encountered for the period 2001-2019 and the total duration of these events. This first analysis was performed for sea surface temperature and considering the entire Northern Adriatic basin.

Before differentiating the experiments, it is clear the unanimous increase in number of MHW events with time. Since the trend was not removed from the time series, a positive tendency in frequency of the extreme events was expected. Climate projection studies have shown that atmospheric conditions over the Adriatic Sea might change, with expected less episodes of Bora winds in the Northern Adriatic during winter season (Belušić Vozila et al., 2019). In the previous dense water analysis it was seen that the second decade was dominated by most frequent mild winters and overall lower dense water volume computed. We can associated it partially with the outcomes in MHW.

Although parent L6 could not represent the entrance of saltier and warmer waters with Levantine origin, the Northern Adriatic region in this experiment also experienced a warming trend over the last years (Figure 3.1). We can speculate that in future scenarios, with warming of temperatures and less cold wind outbreaks in the Northern Adriatic Sea, the remote driver (i.e. water masses entering the southern basin through the Ionian Sea) will probably have

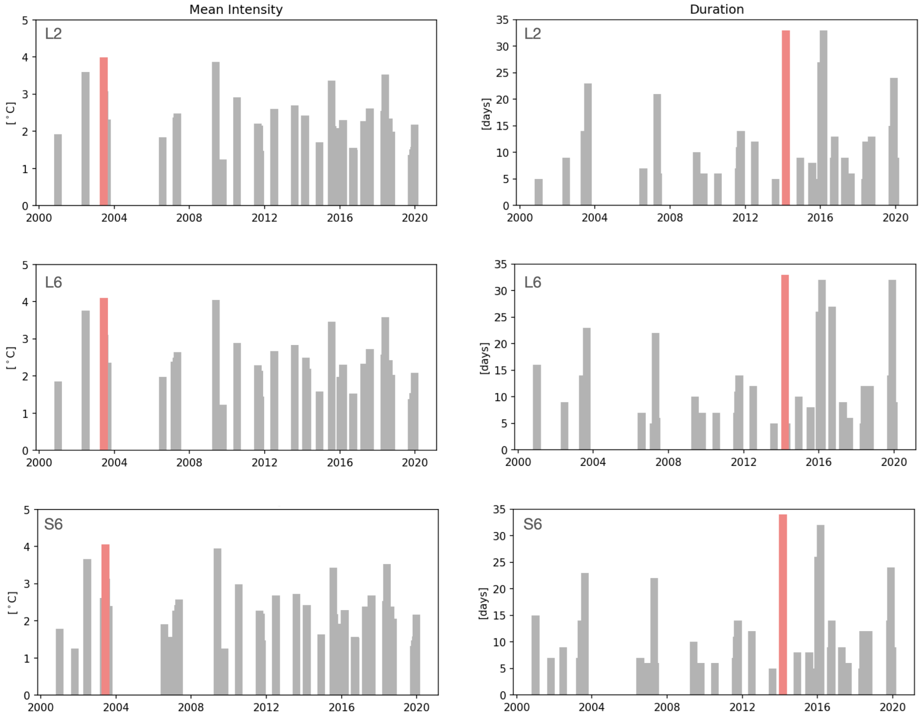

Figure 3.13: Mean intensity [°C] (left) and duration [days] (right) of MHW events computed for each experiment: truth L2 (top), parent L6 (middle) and child S6 (bottom), for the events encountered in the period 2001-2019. Red bar indicates the most intense and longest MHW event, in left and right panels, respectively.

a higher effect in preconditioning dense water formation.

Slight differences can be noticed in the mean intensity of MHW events among experiments. These are usually associated with the particular episodes of short duration, which may stay around the threshold (i.e. 5 days) for being computed as a MHW event or not. However, no significant disparities occurs for MHW intensity between experiments. Since the sea surface temperature is mainly driven by the atmospheric forcing conditions, which do not differ, all experiments have good agreement in the mean temperature of the surface episodes.

Highest intensity was found in 2003, a well known year of intense atmospheric heat wave over Europe (García-Herrera et al., 2010; Olita et al., 2007; Stott et al., 2004). 2003 was a clear marine event influenced by local atmospheric heat wave. From Figure 3.1, at the beginning of this chapter, we can identify the positive anomalous temperature present at the surface layers only. It can be characterized mostly as a summer event that occurred during the stratified water column. This MHW episode was considered the largest in the Mediterranean Sea during the period reported from 1982 to 2014 (Hobday et al., 2016), with mean (maximum) intensity higher than 1°C (2.5°C) in the Adriatic Sea (Juza et al., 2022). As it was an event forced by the local atmospheric forcing, it was well captured by all experiments.

Moving towards the duration of MHW events (Figure 3.13, right panels) few differences occur between the two large domain experiments L2 and L6. Coarse L6 tends to overestimate the duration of some events, such as 2001, 2017 and 2019. In most cases, as it occurs in 2017 and 2019, child S6 is able to overcome this issue and reproduce results similar to truth L2. Very short lasting events may differ between experiments, however the reason for that is probably that they stay around the threshold of duration for being characterized as a MHW event (i.e. 5 days).

The next analysis will focus on the spatial MHW detection, and for that we will have a look also at results in depth (i.e. 20 m). With deeper study we can evaluate cases where extreme events may persist for longer even though the upper layers have changed due to the more rapid atmosphere variation above; and with that we can also have a more clear perception of the downscaling performance. For this comparison the examples of 2007 and 2017 will be shown, as in this period there are some divergences between models (Figure 3.13) and we can understand the reason for that by having a spatial overview.

The next sequence of figures contain spatial metrics of MHW events computed for different years. The idea here is not to focus on the years of most extreme MHW events identified in Figure (3.13). It is instead proposed an overview of the spatial representation of peculiar years of MHW events where the experiments may differ among each other. Results for 2007 and 2017, that will be covered here, bring upon some interesting thoughts regarding the dynamics associated with the MHW events.

Starting with 2007, at surface (Figure 3.14) we do not see large discrepancies between experiments, although some limitations in L6 representation of specific events is evident due to the lack of horizontal resolution. From the downscaling it becomes clear the improve in representation of specific events, especially near the coast (e.g. northeastern region). This spatial representation is important in a prospective of local impacts.

At 20 m depth (Figure 3.15) we now see the main limitation of parent L6, especially in the total number of days. As noticed previously, the coarse experiment tends to overestimate the duration of MHW events and deviates from truth L2. The larger differences in MHW events between the two large domain experiments L6 and L2 as we move to deeper layers could be also associated to the vertical stratification and mixed layer depth.

From the bottom panels it is clear the large improvement in S6 and it is evidence that the downscaling allows for a much better representation of the extreme episodes. Temperature anomaly in deep layers can be associated to the mesoscale activity (e.g. warm core eddies) (Elzahaby and Schaeffer, 2019), for example, and improving the horizontal resolution through a downscaling strategy is crucial to allow the representation of these features.

We can assume that L6 is able to capture most of the MHW events, however does not precisely represent its duration and location. The downscaling in this scenario represents an important tool for a local study of extreme events, especially if we consider deeper vertical levels.

In this particular year of 2007 we could notice that the MHW events are concentrated in the western coastal region. S6 in this scenario is very similar to L2 because it captures the atmospheric conditions and the circulation adjusts to the local forcing. If we now move for 2017 (Figure 3.16), for example, the events computed by the model are located on the eastern part. Therefore, the correct representation of S6 at this time is more dependent on the parent experiment (i.e. L6) conditions.

At this time we see a clear improvement with respect to parent L6, and child S6 is closer to truth L2. However, for this period it is more evident the boundary influence in the inner domain MHW events.

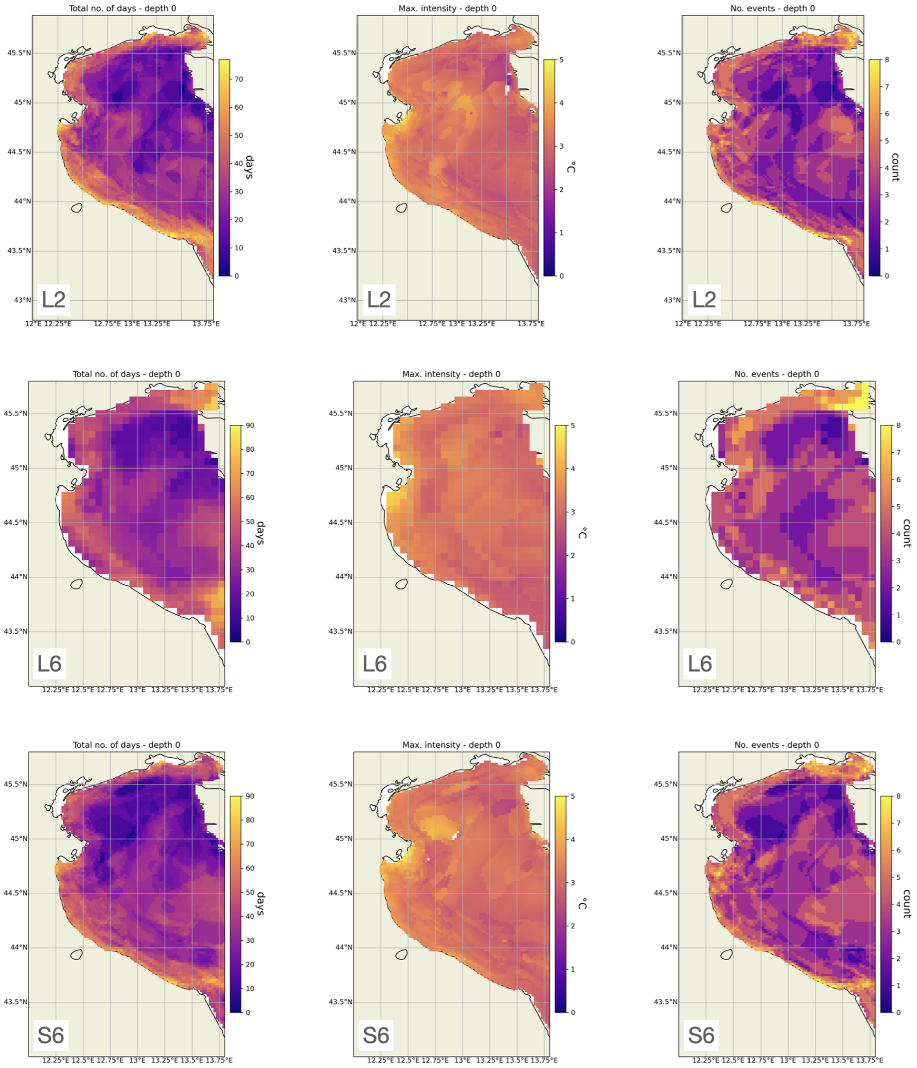

Figure 3.14: Spatial MHW computation for the year 2007 at the sea surface, by means of total number of days (left), maximum intensity [°C] (middle) and number of events (right) for the experiments: truth L2 (top), parent L6 (middle) and child S6 (bottom).

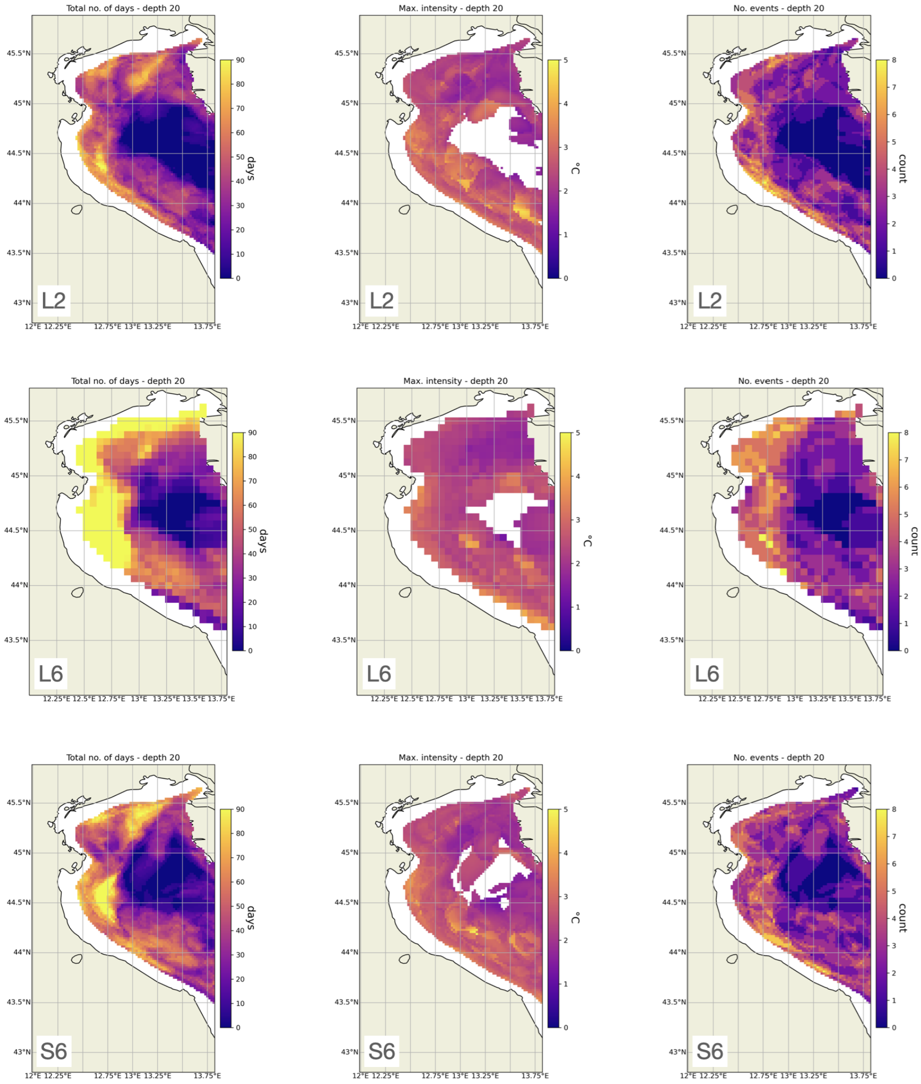

Figure 3.15: Spatial MHW computation for the year 2007 at 20 m depth, by means of total number of days (left), maximum intensity [°C] (middle) and number of events (right) for the experiments: truth L2 (top), parent L6 (middle) and child S6 (bottom).

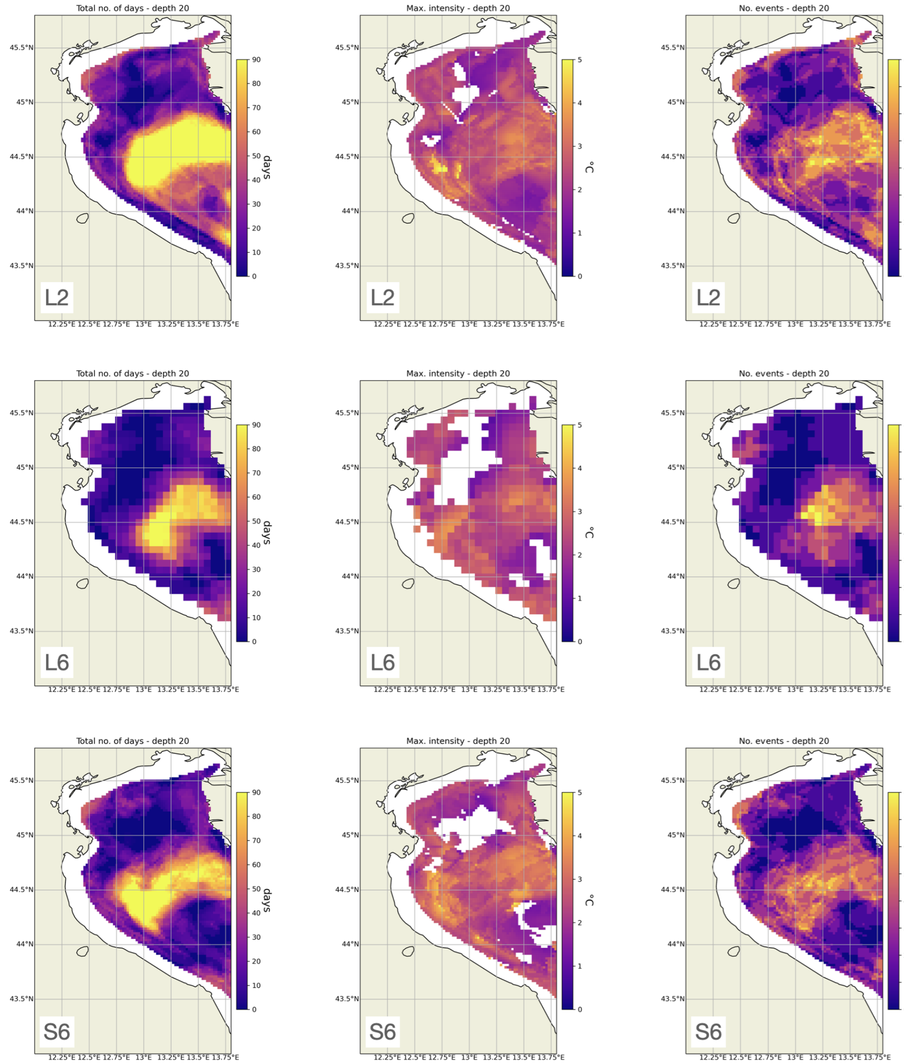

Figure 3.16: Spatial MHW computation for the year 2017 at 20 m depth, by means of total number of days (left), maximum intensity [°C] (middle) and number of events (right) for the experiments: truth L2 (top), parent L6 (middle) and child S6 (bottom).

Again we can arrive to a similar conclusion as in the dense water study. When the MHW events are locally driven by the atmospheric conditions and dependent on the ability of the model in representing the local circulation (e.g. mesoscale features), S6 results are probably more inclined to get outcomes similar to the truth L2. On the other hand, if the occurrence of MHW events derive from outer domain, i.e. advection of warm temperatures towards the northern domain from southern regions, reproducibility of child may vary according to the parent model.

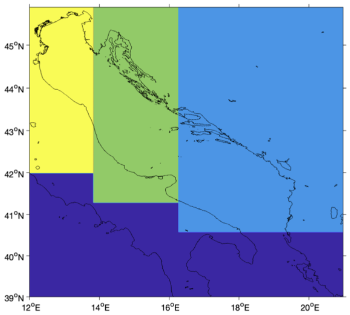

Figure 3.17: Delimitation of the three Adriatic sub-domains (North – yellow, Middle – green, and South – blue) used for the validation. The Northern Adriatic sub-region corresponds to the same domain of the child experiments set up. The entire figure is the parent experiments domain, but the southern area which contains the Ionian Sea was ignored for the validation (dark blue).

3.3 Our regional model for the Adriatic Sea: Validation

The previous sections focused on the perfect model nature of this study, with comparison between downscaling experiments and a truth reference run. This final section is dedicated to the validation of the main large domain experiments proposed, truth L2 and parent L6, for a complete assessment of our model setup and further discussion on the thermohaline results. Validation is presented here in terms of Root Mean Square Deviation (RMSD) and bias by comparison of our model results with in situ observations. Temperature and salinity fields were validated considering the three Adriatic sub-domains, at the areas delimited in Figure 3.17.

Before starting the validation it is important to account for the limitations in observation regarding the Adriatic sub-basins. In the first decade of experiments (2001-2010) significantly more observation datasets were available for the Northern Adriatic, due to the number of campaigns available at that time, with much less for the southern regions (Figures 3.20 and 3.23, top right panels). After 2008 there was a substantial increase in the number of Argo profiling floats for the Ionian and Adriatic Seas, which reflected in large number of in situ data for the Southern Adriatic Sea (Figures 3.20 and 3.23, bottom right panels). In the shallow regions of the Northern Adriatic Sea, however, very few observations are available.

Moreover, when comparing our model daily average results with in situ data it is important to consider that the Northern Adriatic consists of a very shallow region, with lack of vertical profiles available. In very shallow and close to coastline stations the in situ measurements may also be vulnerable to daily variability and tidal effect, which may impact the validation results.

For this study we rely on the CMEMS reanalysis dataset as well, which is a consolidated product with a trustful data assimilation. We understand, however, that the second decade is very limited assimilated for the Northern Adriatic due to the lack of observations in this sub-domain.

From the final outcomes based on dense water variability (Figure 3.5) and the main salinity for each experiment (Figure 3.8) in the Northern Adriatic, we can conclude that our high resolution experiment L2 tends to overestimate the salinity at the Northern Adriatic sub-basin when compared to reanalysis and observations, and slightly underestimate the temperature. This is also confirmed by RMSD and bias (Figure 3.20). The high average salinity and lower temperatures in truth L2 can explain the larger dense water production computed for this experiment in the second decade when compared with CMEMS reanalysis (Figure 3.6).

With data assimilation the CMEMS reanalysis fields are corrected towards observations and are expected to produce higher skill than our model results. But apart from that, there are some differences that could also contribute to disparities. Reanalysis uses climatological values for all rivers, for example, including Po, while in our experiments daily observations are provided for Po River. The atmospheric forcing fields used by CMEMS reanalysis also differs from our experiments, which are, respectively, reanalysis ERA5 (Hersbach et al., 2020) with 25 km resolution and analysis IFS with 12 km resolution (ECMWF products). This is a potential contribution to changes in the surface sea water properties and preconditions for dense water formation. Due to the highly dependence of the atmospheric fields and wind regime for the modulation of the shallow water thermohaline properties, the Northern Adriatic is highly vulnerable to the choice of atmospheric forcing fields (i.e. product and horizontal resolution).

The use of different atmospheric products can change substantially the wind stress and heat loss in the Adriatic Sea, and consequently the thermohaline properties in the basin (Pranić et al., 2023; Vodopivec et al., 2022). The horizontal resolution, especially for the wind fields, is a decisive factor to avoid the underestimation of the wind stress (e.g. Bora winds) and the associated heat flux (Ivatek-Sahdan and Tudor, 2004; Pranić et al., 2023; Vilibić et al., 2016). In study conducted by Pranić et al. (2023) different atmospheric datasets were investigated. The authors found out that ERA5 data showed minimum values for surface wind stress, which could be explained by the low resolution and inability in reproducing the Bora jets; however in upward turbulent fluxes analysis it reached maximum heat losses when comparing to others.

The constant salinity values prescribed at the river mouths in our model are also a source of uncertainties, and could partially explain the overestimation of salinity at surface. Especially in the northern sub-basin where there is the Po River runoff with daily observations provided at the river mouths, the overall salinity is highly dependent on the river variability. As an alternative, the use of sea surface salinity at rivers instead of a constant value could possibly reduce bias near river mouths, however it could cause a drift in the mean basin salinity (Tseng et al., 2016). This was confirmed by a test study performed for our coarse experiment L10 (not shown), which proved not to be an accurate approach for this study. Future improvements could involve time dependent salinity provided at river mouths and better representation of the estuarine processes based on estuary models (e.g. Verri et al., 2020, 2021), for example.

Finally, the constant viscosity and diffusivity coefficients are also another limited factor on our model configuration for accurately represent the mixing at the basin. Space and time variable coefficients could possibly provide a more realistic representation of the local features and could potentially improve the model validation. This is expected to be implemented in future studies.

When looking at the vertical profiles of the other Adriatic sub-basins and at deeper layers in the comparison for the entire Adriatic domain validation we see, however, that the overall validation is not equal as the northern sub-basin. It was seen that, for the Northern Adriatic sub-domain, our model tends to slightly overestimate the salinity at surface levels. As we move to deeper layers or even to the other Adriatic sub-basins we can notice that this scenario changes.

Figure 3.18 contain the validation in terms of Hovmoller plot, and the model seems to represent well the salinity of the basin on average, with low RMSD from 2011 to 2019, mainly. Again the first years (2001-2010) correspond to localized observations in the Northern Adriatic which is more sensible to local atmospheric forcing.

Overall temperature validation is also reasonable (Figure 3.19). Major values of RMSD can be found in depths around 20-30 m, which is probably associated to uncertainties in the stratification of the water column. The deepening of the mixed layer depth in late summer/beginning of autumn, for example, can be a source of uncertainties.

Although there are some bias in our model, we can assume that the values are acceptable and presume that the truth experiment L2 is a good approximation of the thermohaline dynamics of the Adriatic basin. The same does not happen with parent L6, as expected. From Figure 3.21 it is clear the overall freshening of the basin with respect to observation, due to the misrepresentation of saltier water entrance through the Otranto Strait. Hovmoller of temperature can be seen in Figure 3.22, where the RMSD also indicates uncertainties in the stratification.

In the Northern Adriatic validation for L6, however, we see a slightly different scenario than in L2. As we learned from L2 validation, our model tends to slightly overestimate salinity at surface in the northern sub-basin. As in L6 there is the lack of salt water intrusion from the Ionian Sea, the freshening of the basin actually counterbalances the positive salinity bias of the model, and what we see is a slightly better salinity bias in the Northern Adriatic (Figure 3.23. This accounts also for less dense water formation in the second decade of experiment and, in years of low dense water production (e.g. 2014, 2015), L6 results may be closer to CMEMS reanalysis (Figure 3.6 top panel). A yet misleading result, since we know that L6 model is not reproducing the reality as it should.

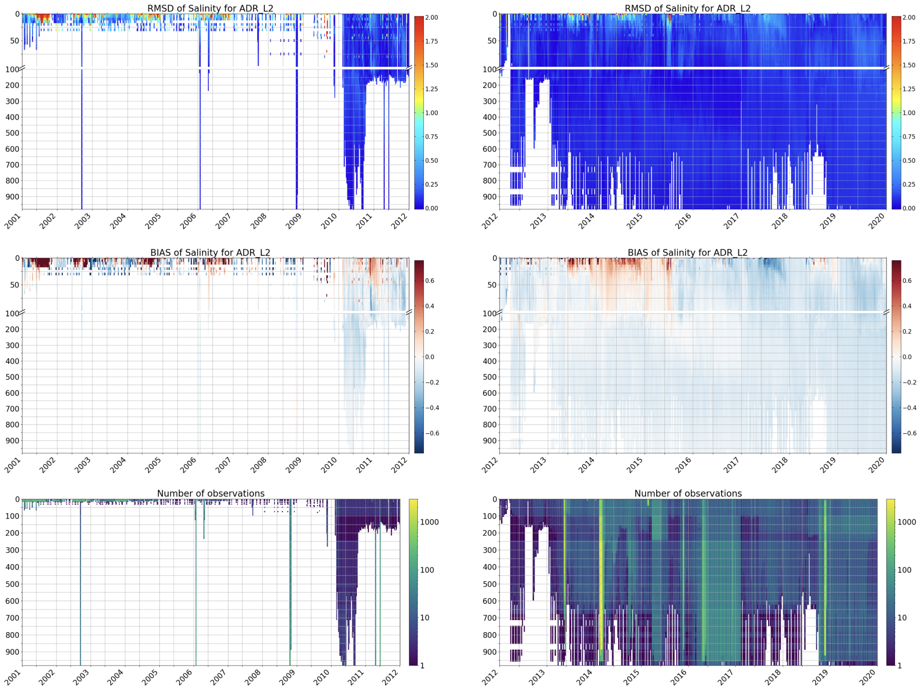

Figure 3.18: Salinity RMSE and BIAS for truth experiment L2 compared with in situ observations, for the entire Adriatic Sea. Left and right panels separate two periods (2001-2011 and 2012-2019) which are linked to the multi-annual variability in the thermohaline properties identified.

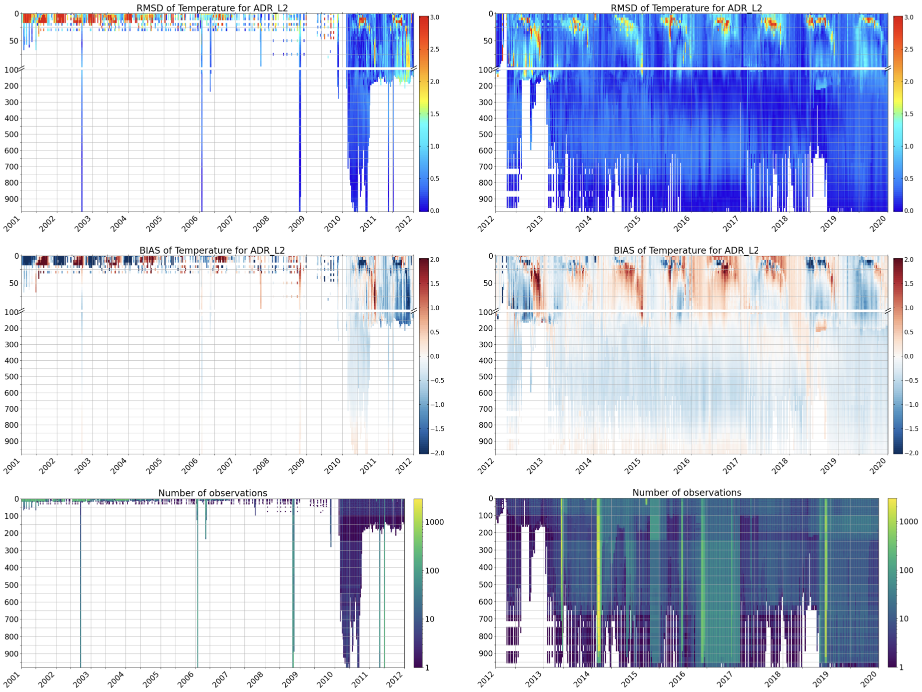

Figure 3.19: Temperature RMSE and BIAS for truth experiment L2 compared with in situ observations, for the entire Adriatic Sea. Left and right panels separate two periods (2001-2011 and 2012-2019) which are linked to the multi-annual variability in the thermohaline properties identified.

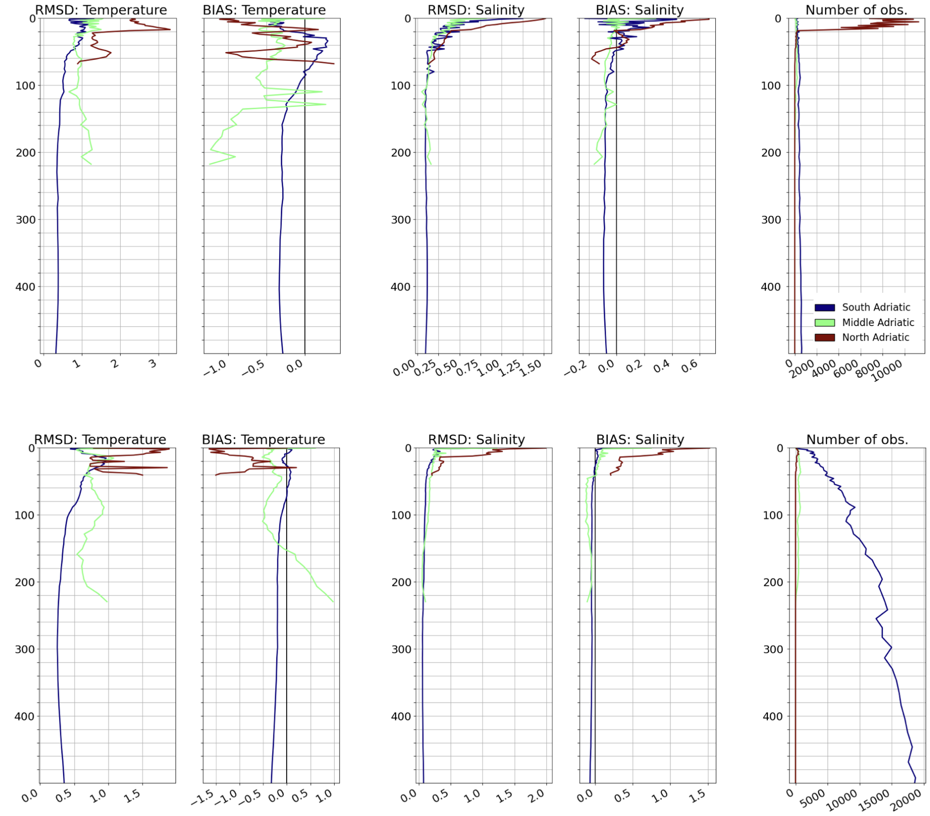

Figure 3.20: Vertical profiles of Temperature and Salinity RMSE and BIAS for truth experiment L2 compared with in situ observations, computed for the each of the Adriatic Sea sub-basins (sub-domains delimitation can be seen in Figure 3.17). Top and bottom panels correspond to periods 2001-2011 and 2012-2019, respectively, which are linked to the multi-annual variability in the thermohaline properties identified.

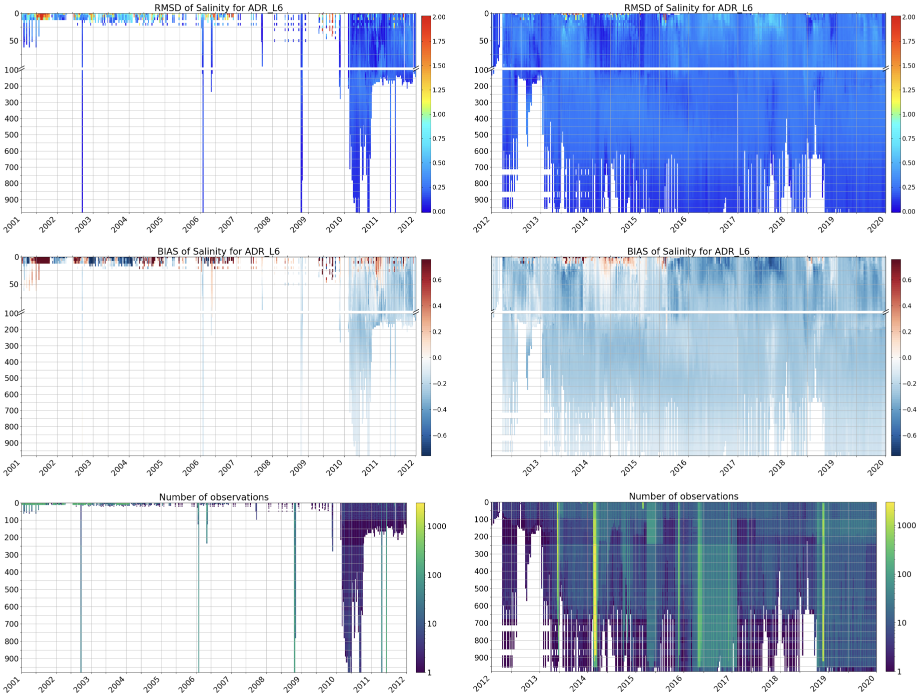

Figure 3.21: Salinity RMSE and BIAS for parent experiment L6 compared with in situ observations, for the entire Adriatic Sea. Left and right panels separate two periods (2001-2011 and 2012-2019) which are linked to the multi-annual variability in the thermohaline properties identified.

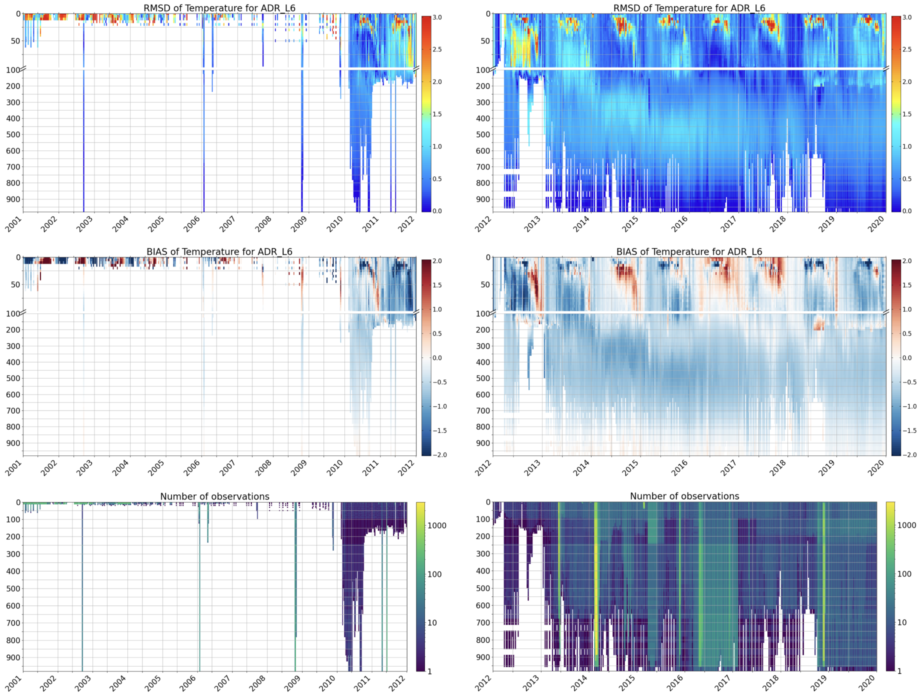
RMSD of Temperature for ADR_L6

RMSD of Temperature for ADR_L6

BIAS of Temperature for ADR_L6

BIAS of Temperature for ADR_L6

Number of observations

Number of observations

Figure 3.22: Temperature RMSE and BIAS for parent experiment L6 compared with in situ observations, for the entire Adriatic Sea. Left and right panels separate two periods (2001-2011 and 2012-2019) which are linked to the multi-annual variability in the thermohaline properties identified.

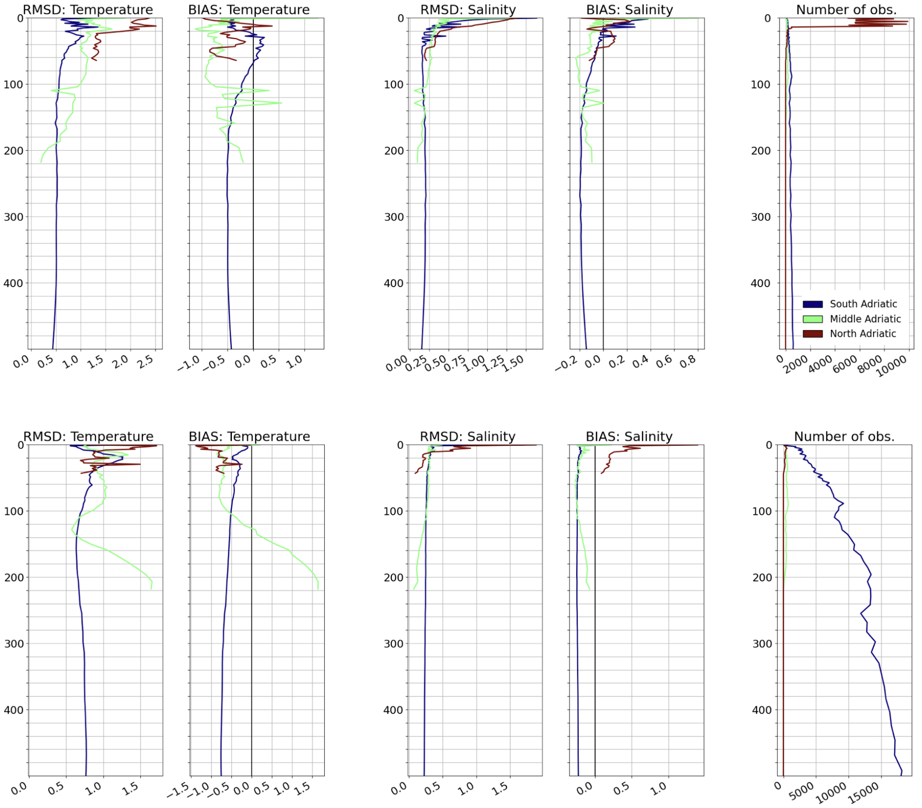

Figure 3.23: Vertical profiles of Temperature and Salinity RMSE and BIAS for parent experiment L6 compared with in situ observations, computed for the each of the Adriatic Sea sub-basins (sub-domains delimitation can be seen in Figure 3.17). Top and bottom panels correspond to periods 2001-2011 and 2012-2019, respectively, which are linked to the multi-annual variability in the thermohaline properties identified.

3.4 Conclusions

This study has shown that reproducibility of the downscaling experiments for the Northern Adriatic Sea with respect to physical processes varies depending on the main drivers of the local thermohaline properties.

Following the clear example of dense water formation, when the main preconditioning factors are associated with local condition (i.e. atmospheric forcing), child S6 outperforms its parent model L6. In this scenario, S6 is able to recover the equivalent dense water volume as the "truth" L2.

On the other hand, when remote drivers (i.e. saltier water intrusion from the Ionian Sea) are more decisive on the dense water formation, the reproducibility of the downscaling experiment relies on the thermohaline circulation from the parent. If under this condition the parent model has limitations, as it was identified in L6, it propagates to the downscaled domain.

We could speculate that the changes in phase of the Adriatic-Ionian Bimodal Oscillation System (BiOS) not only modulates thermohaline properties of the water masses in Southerns Adriatic Sea through the shift of Northern Ionian Gyre (NIG); it also contributes to changes in the density driven circulation that will then affect salinity in the Northern Adriatic. As a result, dense water formation in the northern sub-basin seemed to be remotely affected by the cyclonic phase of the BiOS. During this configuration, saltier waters with Levantine Basin origin enter the Adriatic Sea and contribute to increase in salinity of the basin, further affecting also the Northern Adriatic.

In Marine Heat Waves (MHW) study, although here instead of addressing a local mechanism we are just considering a statistical overview based on temperature anomalies, we can still relate to some of the previous findings. When MHW events can be attributed to local factors, reproducibility of child S6 is higher and the spatial representation of these events is similar to truth L2. This example was found for episodes attached to the coastline, and seem to rely on the atmospheric conditions and the ability of the model in reproducing the small scale features. However, when the MHW events are computed at deeper regions close to the open boundary, the metrics tend to follow to some extent the parent experiment L6.

Finally, the errors associated with the coarse model L6 actually led to an interesting investigation on the interannual variability of temperature and salinity in the Adriatic. We were able to demonstrate the importance of the correct representation of inner domain complex coastline and bathymetry, such as the

Otranto Strait. The misrepresentation of the dynamics at this narrow passage by parent L6 due to the lack of horizontal resolution compromised the salt water inflow towards the Adriatic Sea, causing a relative freshening of the basin with effect towards the northern sub-basin.

4 Spectral nudging application for coastal ocean modelling

4.1 Coastal modelling and the “inner” value problem

As it was seen previously in Chapter 3, numerical models may present limitations in correctly representing the dynamics along complex coastlines. Indeed, many authors have previously investigated solutions for improving overflow conditions and circulation along straits and channels. Some can be listed here such as: localised different vertical coordinate system (Bruciaferri et al., 2023); Reckinger et al. (2015) have found that z-coordinate levels tend to produce more mixing than a sigma coordinate, for example; local grid refinement, more straightforward in finite element models (e.g. Haid et al., 2020) but also available for finite difference codes (e.g. Debreu et al., 2008); increase of vertical resolution.

Many sensitivity studies have been performed by Colombo et al. (2020) for the above mentioned changes and also for the advection and diffusivity schemes, as well as for vertical mixing. For the case of overflow, the adjustment of vertical viscosity can actually have a more powerful result (e.g. Reckinger et al., 2015) than the resolution for the representation of mixing at a slope bathymetry.

It is not the first time that a misrepresentation of the entrance of eastern Mediterranean waters have been reported in numerical models for the Adriatic Sea. In work conducted by Oddo et al. (2005) and Oddo and Guarnieri (2011) the authors highlight a tendency of freshening in their model which was possibly linked to the lack of saltier waters entering with Aegean Sea origin, but also to the overestimation of the vertical/horizontal mixing processes.

The increase in vertical resolution does not necessarily guarantee a better representation of the bottom shape in channels and straits (Colombo et al., 2020). Our L6 experiment is a clear example case that the high vertical resolution was not sufficient for a proper representation of the Otranto Strait due to the steep bathymetry of the region. At a coarse horizontal resolution (i.e. 6 km), the model grid slope was ineffective in reproducing the local topography slope. This is evident by comparison of sections along the Otranto Strait in previous analysis (Figure 3.9).

From what have been covered by the previous chapters of this thesis, different than a “boundary value” problem, we can associate the major discrepancies of thermohaline properties between L6 experiment and its original parent CMEMS reanalysis to what we call here an “inner domain problem”. The main differences are not very much associated to the model drift, but in fact to a misrepresentation of the inner domain features by the nested model L6, more precisely the Otranto Strait circulation.

We already see many differences between L6 and L2 due to the inability of L6 in correctly representing the small scale variability. However, this difference becomes a decisive factor for the Adriatic Sea thermohaline dynamics after 2011 with the reversal of the North Ionian Gyre (NIG) to its cyclonic phase. With the increase number of available in situ observations in the Ionian Sea - Southern Adriatic region during the second decade of simulations (2011-2019), as covered in the validation section in Chapter 3.3, we can trust that the data assimilated product can represent the sea water properties closer to reality.

With the clear limitations of L6 experiment and the aim at looking for innovative solutions in coastal modelling, the spectral nudging technique was found to be an interesting tool. With this study we thus want to evaluate the applicability of using spectral nudging to diminish the limitation of a not ideal resolution model (i.e. L6) in correctly representing the thermohaline circulation inside the domain.

The application for the Adriatic Sea was an opportunity to test a method that has been developed but never applied for a shallow semi-enclosed basin as the Adriatic one, a complex region highly influenced by local (i.e. atmospheric conditions, river discharge) and remote (i.e. Ionian Sea waters entrance) forcing. The spectral nudging is expected to directly affect the energy of the large scales, and indirectly affect the small scales through the model's nonlinear dynamics. Moreover, this approach is intended to place the large-scale features at the right locations, suppress unrealistic re-circulation near lateral open boundaries and correct thermohaline circulation at the inner domain.

4.2 Design and implementation of spectral nudging

As proposed for the overall structure of this thesis, this last chapter was developed mainly after the key findings of Chapter 3. The limitations encountered for parent experiment L6 motivated us to move back on the generation of this large domain model and try to recreate it with a “little help” from spectral nudging. It is important to keep in mind that now the focus is on the nested experiment that covers the entire Adriatic Sea, which lateral open boundary conditions are provided by CMEMS reanalysis.

One of the pillars when opting for spectral nudging is to trust the parent model for the large-scale predictions. For example, coarse resolution models that include data assimilation capture the position of the large-scale ocean features in good agreement with observations. In this sense, our parent model (CMEMS reanalysis) is expected to provide a good representation of the Adriatic Sea fields for the nested new L6 experiment, named L6+. The new experiment L6+ have exactly the same forcing fields and numerical choices as the previous experiment L6 (detailed in Chapter 2.2.1), except for the spectral nudging implementation. A schematic representation of the new experimental design with spectral nudging can be seen in Figure 4.1.

The time step of spectral nudging was set to 1 h, in a procedure that is done entirely on the fly. Further details on the spectral nudging tool that was developed for NEMO ocean model is in Appendix C.1.

It is expected that the nudging of salinity and temperature fields will correct the density gradient inside the domain, and this by itself may already have an impact in the velocities. To evaluate that response on the density field, two different approaches can be made: applying spectral nudging only for tracers (i.e. temperature and salinity), and applying spectral nudging both for tracers and velocity fields.

Wright et al. (2006) computed the two different approaches and observed that spectral nudging of tracers would give better results than the correction for the momentum fields. In the current study, the main idea was to make corrections only on tracers and expect that the density driven circulation would evolve from that. In case the results would not be as expected, the second approach (i.e. apply correction terms to the momentum equations) could be explored.

The correction applied with spectral nudging resembles the usual relaxation technique broadly used in ocean modelling, when the inner domain field is

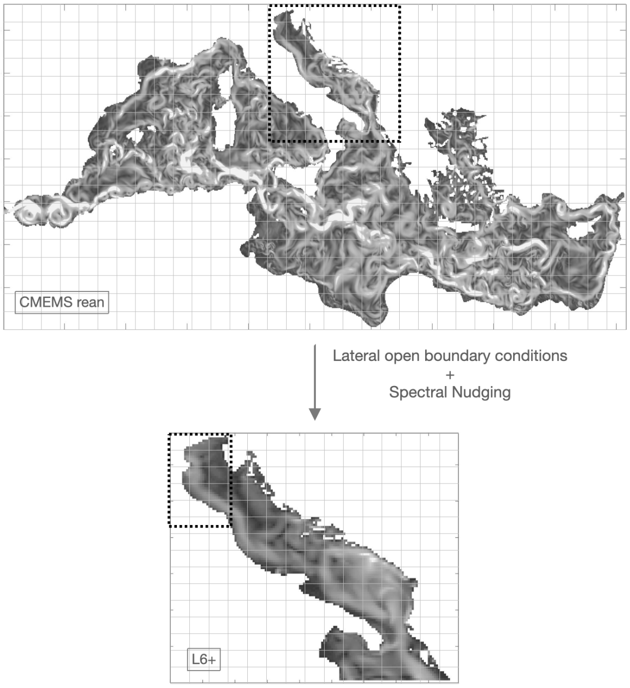

Figure 4.1: Schematic representation of the nesting strategy for new experiment L6+, with inner domain being nudged towards the parent model (CMEMS reanalysis). Shading is a daily output of surface velocities, for illustration.

nudged towards a trustful climatology or observations to avoid model drift. Spectral nudging, however, is applied only to the large scales, to allow the smaller scales not to be directly affected and evolve prognostically with the model's dynamics. Moreover, this correction will be made for a previously stipulated time step and according to the time frequency of the parent model fields.

The model temperature and salinity will be, thus, updated according to the following equations 4.1 and 4.2:

$$T_t = D_t(T_{t-1}) + \gamma \langle T_t^{PM} - D_t(T_{t-1}) \rangle_L \tag{4.1}$$

$$S_t = D_t(S_{t-1}) + \gamma \langle S_t^{PM} - D_t(S_{t-1}) \rangle_L \tag{4.2}$$

Where T_t and S_t are the updated temperature and salinity at the specific time step that the spectral nudging is being applied, D_t is the nonlinear operator representing the model's dynamics and forcing, T_{t-1} and S_{t-1} are the model outputs of temperature and salinity at prior time step, and T_t^{PM} and S_t^{PM} are the temperature and salinity of the parent model (CMEMS reanalysis). In the formula $\langle\rangle_L$ denotes the quantity that has been spatially smoothed to extract the large scale component.

We can reformulate the previous spectral nudging formulation in the form of model tendencies, following equations 4.3 and 4.4.

$$\frac{\partial T}{\partial t} = f(T) + \kappa \langle T^{PM} - T \rangle_L \tag{4.3}$$

$$\frac{\partial S}{\partial t} = f(S) + \kappa \langle S^{PM} - S \rangle_L \tag{4.4}$$

In the previous equations 4.1 and 4.2, D_t is written as a discrete operator representing the tracer solution, that is the result of all the model's dynamics and forcings. If we wish to write it as a continuous function, we can reformulate it as $f(T)$, and our spectral nudging coefficient is now over a time scale and referred to as κ.

Note that in Equations 4.1 and 4.2 linearity of the $\langle\rangle$ operator is assumed such that $\langle A + B \rangle = \langle A \rangle + \langle B \rangle$ (this assumption and validity is discussed further in the Appendix section C.1.2).

The strength of the spectral nudging varies according to a spectral nudging coefficient (γ), defined as:

$$\gamma = \gamma_0 \Gamma(x, y, z) \tag{4.5}$$

Represented by two components: a constant part called γ_0 which accounts for the ratio of the nudging time step divided by the nudging relaxation time scale; and a variable one ($\Gamma(x, y, z)$), which varies in space according to the three dimensional position in the domain. The spatial nudging dependency (detailed in section 4.2.2) was defined for our Adriatic Sea domain based mainly on the bathymetry and the depth of saltier water influence.

4.2.1 Filtering the small scales

The main purpose of the filter is to actually avoid damping eddy variability, since we are nudging only the large scales. To obtain the large scale components of the tracers, a two-dimension low pass filter has to be applied for each vertical depth. Due to the limits of the coastlines in ocean modeling that differs to the practice on atmospheric modeling, special attention is needed when applying the spatial filter. The recursive, second order Butterworth filter was found to be a suitable option (Katavouta and Thompson, 2016; Thompson et al., 2006) to spatially smooth the oceanic variables which will be nudged, and at the same time offers a good optimization of computer time (Roberts and Roberts, 1978).

Since only large scales are nudged, a cutoff wavelength (λ_c) needs to be settled. This wavelength was stipulated from some sensitivity analysis based on the features of the Adriatic Sea and its seasonality, and how smoothed we wanted our fields. For this step it is important to consider the size of the domain, the first baroclinic Rossby radius of deformation (Rd) of the Adriatic Sea, and the seasonality of the basin dynamics (i.e. river plume, heat fluxes and winds). The computation of Rd (Chapter 2) based on the experiment's results is in good agreement with literature (Bergamasco et al., 1996), with approximately 5 km in summer and less than 2 km in winter for Northern Adriatic, and much larger values at the order of 10 km in the southern area of the domain.

The Butterworth filter is a recursive filter that has been already applied to oceanography fields (Katavouta and Thompson, 2016; Roberts and Roberts, 1978). The Butterworth filter signal allows to have a flat response at the pass band (in this case the large scales), and below this it will smoothly reach the smaller scales at the transition to the stop band. This means that above the cutoff wavelength no filter will be applied, and below it will increase the smoothing towards the smaller scales. The gain G corresponds to the magnitude of the

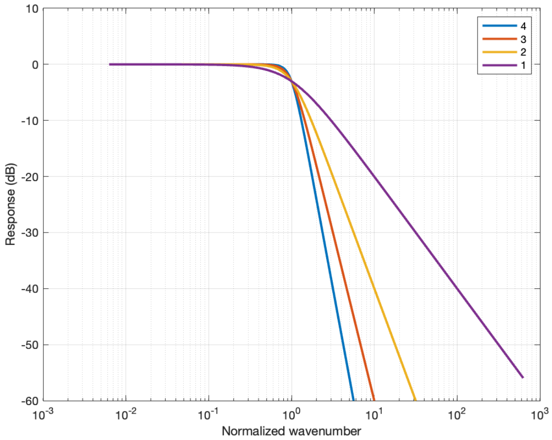

Figure 4.2: Signal response of the Butterworth filter for 1st, 2nd, 3rd and 4th order.

frequency (wavelength) response. The power gain G^2 is thus defined in terms of the square of the transfer function H_B, given by:

$$G^2(\lambda) = |H_B(j\lambda)|^2 = \frac{1}{1 + (\lambda/\lambda_c)^{2n}} \tag{4.6}$$

Where $j = (-1)^{1/2}$ and n is the order of the filter. The order will determine the slope of the transition from pass to stop band, exemplified in Figure 4.2. After performing some sensitivity tests, the best choice for this experiment was the second order filtering.

A cutoff wavelength (λ_c) of 40 km was decided to be used for filtering the small scales in our domain, which corresponds to 3-4 times the Rd of the southern region in the Adriatic Sea. The filter was applied iteratively 5 times.

Another advantage of using the Butterworth filter is that it is close to acting as a linear operator. The spectral nudging increment in Equations 4.1 and 4.2 based on the large scales is obtained from a linear relationship. This means that the low pass filtering can be applied either before or after computing the difference between parent and child fields. Both approaches should lead to the same result, as covered in Appendix C. However, computing first the difference between models and filtering the difference afterwards means considerable reduction in computational time.

4.2.2 Spatial variability of nudging

The criteria for developing our spectral nudging strategy for the new experiment L6+ is based mainly on the outcomes of Chapter 3. Previous experiment L6 was not capable in correctly representing the saltier water entering through the Otranto Strait resulting in inaccurate thermohaline properties inside the Adriatic Sea. Therefore, with spectral nudging we expect to nudge new experiment L6+ inner domain towards the reanalysis fields that were provided previously (in L6) just at the open boundaries.

As mentioned previously, the nudging coefficient will specify how strong the spectral nudging will be in each grid cell of the domain. It may vary along the spatial domain, depending on horizontal and vertical position based on a condition previously stipulated. From Equation 4.5, $\Gamma(x, y, z)$ is a function of position. This space variable parameter was decided based on analysis of modeling results and dynamics of the Adriatic basin. The nudging can vary depending on the bathymetry (e.g. Katavouta and Thompson, 2016), for example, or even based on the distance from the lateral boundary, decreasing towards the interior of the integration domain (e.g. von Storch et al., 2000).

For the Adriatic Sea domain, due to the large influence of river discharge and coastlines, a good approach would be strong nudging close to the boundary, decreasing towards the inner domain with a particular attention to be devoted to the shallow Northern Adriatic areas and the Po river region of freshwater influence.

A space variable nudging parameter ($\Gamma(x, y, z)$) is calculated for the domain, varying in grid point depending on how strong the spectral nudging should be for each specific region. For that a two-dimensional mask was created based on the bathymetry, so that nudging would be higher as the bathymetry increases (Figure 4.3(a)). In this way we are actually putting a stronger constraint towards the southern open boundary, covering the critical region of misrepresentation by the model (i.e. Otranto Strait).

For a three-dimensional space dependency of the nudging, expected to better reproduce the features that were missing in previous experiment, a vertical condition was also imposed. Spectral nudging was set to be stronger at the main depth of salt water entrance in the inner domain, i.e. 150 m according to the truth L2 experiment results. After this critical depth nudging decreases towards maximum depth. Zero nudging was applied for surface levels from 0-50 meters, so that very shallow areas in the Northern Adriatic Sea would not be

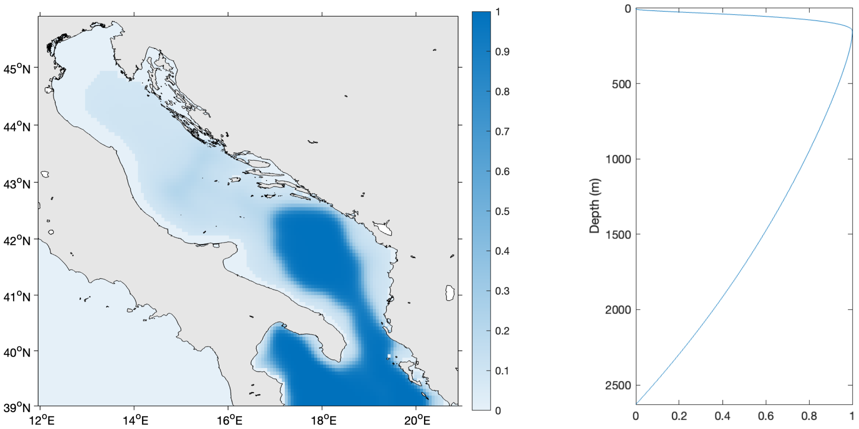

(a) (b)

Figure 4.3: Horizontal (a) and vertical (b) variability of nudging parameter.

directly affected by spectral nudging, and nor would coastal, river influenced, areas. So that a final vertical dependency of nudging can be illustrated in Figure 4.3.

The final mask used for the spectral nudging computation was thus a three-dimensional one, which corresponds to the product of the horizontal and vertical values of the nudging parameter. This choice was made as an attempt to improve the representation of intermediate waters influence from the eastern Mediterranean characteristics, at the same time accounting for all the peculiarities of the Adriatic Sea basin (e.g. river influence, coastline complexity, shallowness).

The entire spectral nudging tool was prepared as a new key configuration for the NEMO ocean model. Details of the procedure and its implementation are covered in Appendix C.1.

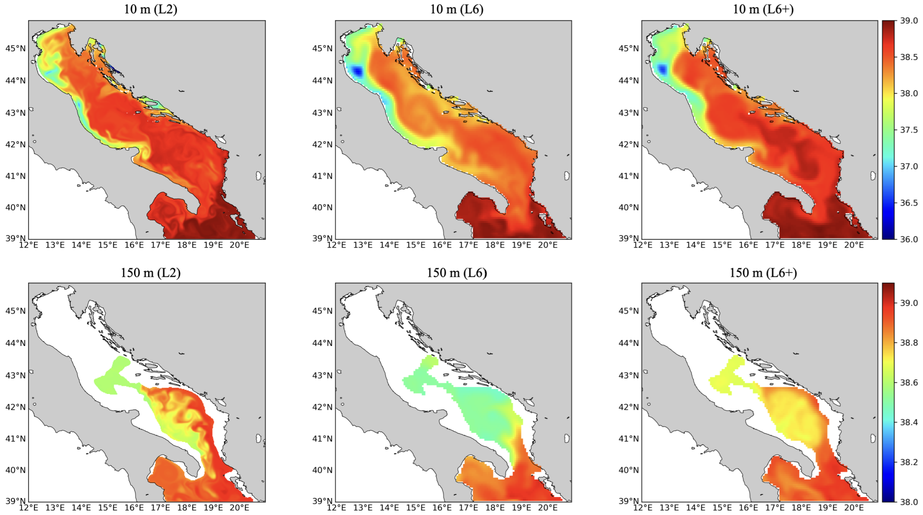

Figure 4.4: Maps of salinity at 10 m (top panels) and at 150 m depth (bottom panels) for L2 (left), L6 (middle) and L6+ (right) at a daily output in 21/06/2012. (Updated color bar with depth)

4.3 *Are we able to improve the representation of water mass structures with spectral nudging?*

In order to focus on the efficiency of the method and how it would affect the thermohaline properties and circulation in the domain, a shorter simulation was performed in this study. The new experiment L6+ starts in 2012, covering exactly the critical period observed in the dense water computation and sea water properties in Chapter 3. The initial condition (temperature and salinity) was provided from daily output of previous experiment L6 for the day 01/01/2012 and the experiment lasted 8 years, ongoing until 2019.

Maps of salinity (Figure 4.4) from summer 2012 already indicate the improvement in representing the saltier water entrance through the Otranto Strait in the nudged experiment L6+. Different than the missed feature entering the Adriatic Sea in L6 which resulted in overall freshening of the basin, the new experiment L6+ was able to account for the salt water intrusion with Levantine Basin origin. Further comparison between experiments and CMEMS reanalysis salinity can be found in Appendix C.2.

The goal here was not to replace the model's condition and implement completely new features, but to improve the representation of internal features that

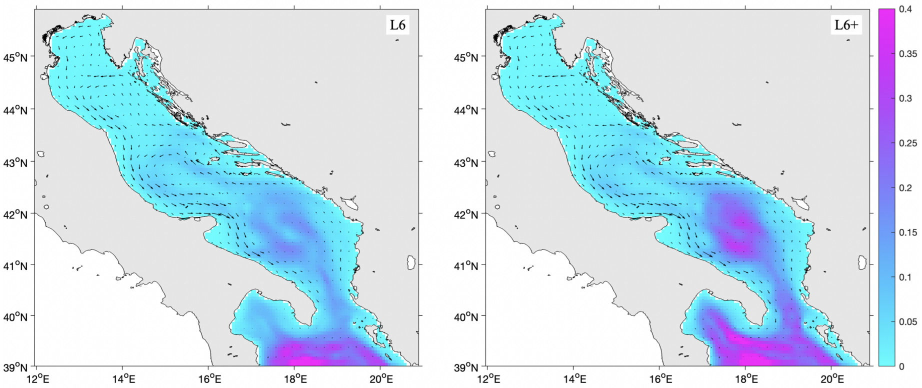

Figure 4.5: Mean circulation in L6 (left) and L6+ (right) experiments. Vectors indicate depth averaged velocity of currents $[\mathrm{m\,s^{-1}}]$ and shaded fields correspond to depth integral of volume transport [Sv].

were being missed by the model. And this objective was accomplished: although spectral nudging was applied only to temperature and salinity, the corrected fields resulted in an updated density gradient that affected the circulation at the basin.

Maps of currents (Figure 4.5) indicate that we are enhancing the volume transport along the southern domain and at the Otranto Strait in L6+. While in L6 the volume transport at the domain was localized at the southernmost part with no strong enough inflow at the Otranto Strait, in L6+ the transport towards the Southern Adriatic sea and cyclonic gyre was improved considerably. This is an indicative that in L6+ there is a better representation of the inward flow at the Otranto Strait.

Looking more specifically at the Otranto Strait (Figure 4.6) inflow of saltier waters towards the Adriatic Sea is evident. In temperature no significant changes occur but the new experiment is closer to truth L2. The improvements become very clear at the salinity profile, where now the intermediate saltier water is present and well captured by the experiment in the eastern inward flux at 100-300 m depth. We bring attention to the average inflow of water at the eastern side and outflow from west which cover much higher levels in depth, meaning that the deeper saltier waters are actually moving towards the Southern Adriatic.

The next analysis of performance of the spectral nudging is with respect to the representation of physical processes. Again we can judge the new experiment

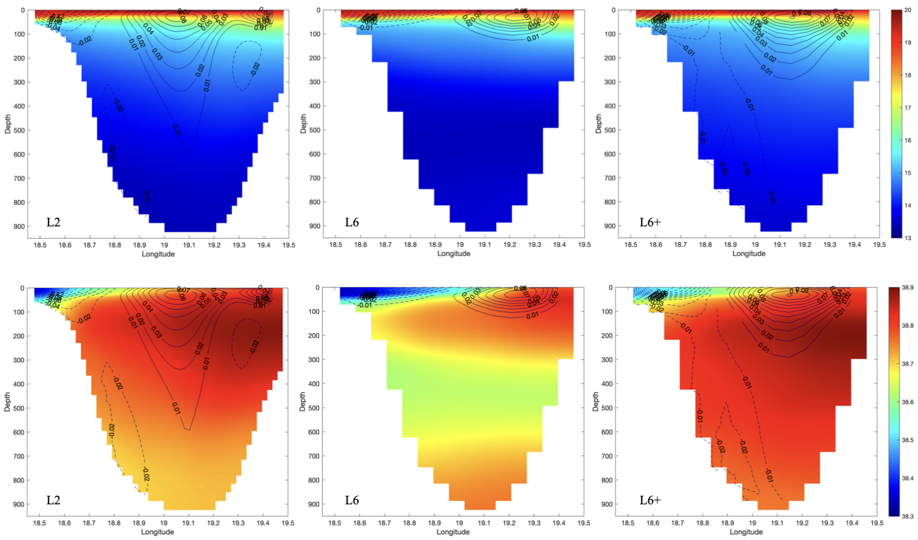

Figure 4.6: Vertical transect along the Otranto Strait with mean temperature [°C] (top) and salinity [psu] (bottom) fields for L2 (left), L6 (middle) and L6+ (right). Contour lines correspond to meridional velocity [$\mathrm{m}^2\,\mathrm{s}^{-1}$].

L6+ computation of dense water in the Northern Adriatic having truth L2 and CMEMS reanalysis as reference. At this point it is important to remember that the spectral nudging was applied only at deeper levels, i.e. more than 50 m (Figure 4.3), in order to avoid a direct modification of surface properties and at the shallow Northern Adriatic sub-basin. It means that any divergence in the coastal northern features between L6 and L6+ would be associated to the internal dynamics indirectly influenced by the spectral nudging.

In Figure 4.7 there is the dense water volume computed for each of the Adriatic sub-basins for the new experiment L6+. With the changes in the thermohaline circulation with spectral nudging, dense water formation in L6+ improved when compared with L6. This is noticeable especially for the Southern Adriatic, where the previous model setup failed in representing the inner domain features at the Otranto Strait.

As expected, dense water in the southern and middle sub-basins, where spectral nudging of the tracers was stronger, is close to CMEMS reanalysis, as it is directly influenced by the correction of tracers in L6+. In the future further experiments can be performed with different filtering options or time stepping for the nudging. For the purposes of the current study, we could demonstrate that the procedure is working and the salinity and temperature fields are being

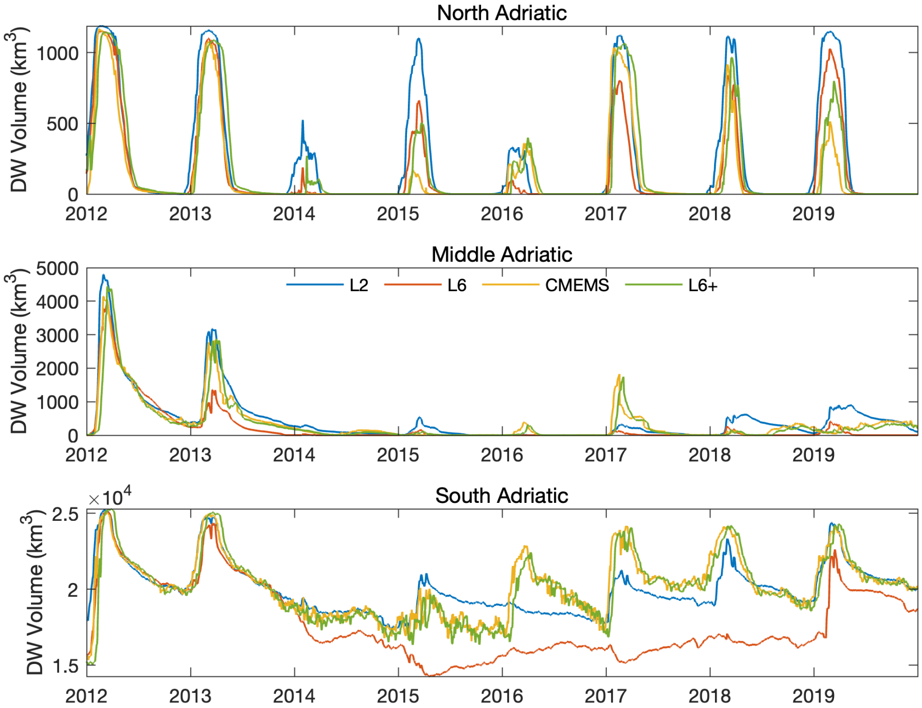

Figure 4.7: Dense water volume computed for L2, L6 and L6+ compared with CMEMS reanalysis, for the three Adriatic sub-basins. The potential density threshold is 29.2 $\mathrm{kg\,m^{-3}}$ for Northern and Middle Adriatic, and 29.0 $\mathrm{kg\,m^{-3}}$ for Southern Adriatic.

corrected towards the large scales of the parent reanalysis solution.

In the Northern Adriatic dense water volume (Figure 4.8), however, there is almost no direct update on the fields but instead updated water masses coming from south and entering the shallow sub-domain. In fact, the differences or similarities between new experiment L6+ and original L6 can give us an indicator of the influence of remote or local drivers for dense water formation.

In 2015 both L6 and L6+ present very similar dense water volume, both lower than the L2. In CMEMS reanalysis the volume computed was also much lower than L2, but even lower than L6 and L6+. This result is thus an indicator that the rather low dense water production in this period was mainly influenced by local forcings. This year specifically presented large Po river discharge (Figure 3.4), and indeed all experiments had the lowest salinity values.

2017, for example, is a year of both local and remote influence of dense water formation. In this year the drop of temperature in winter favoured dense

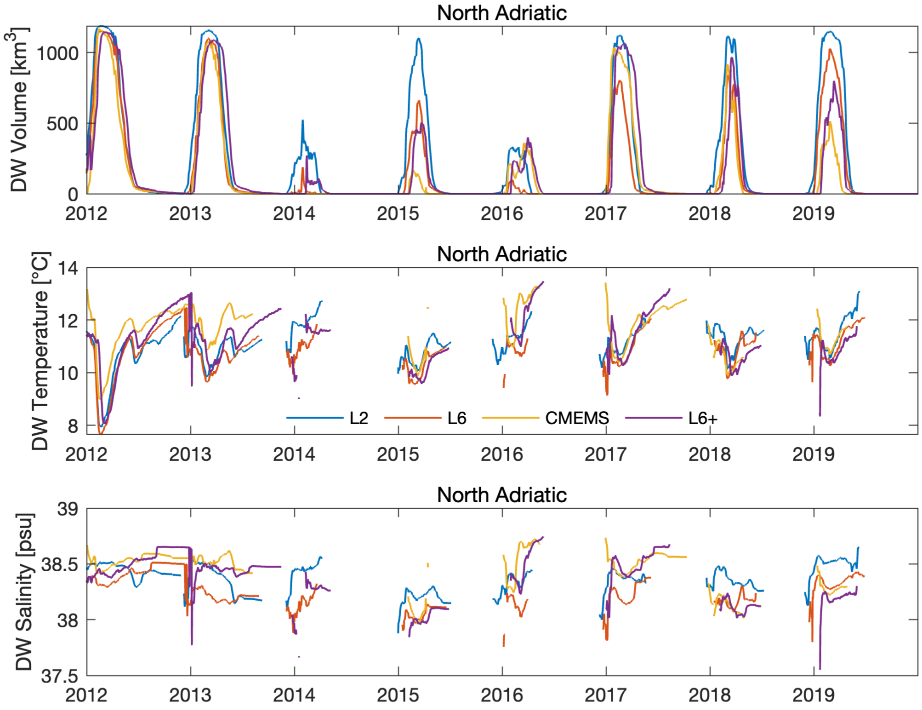

Figure 4.8: Dense water volume (top), temperature (middle) and salinity (bottom) computed for L2, L6 and L6+ compared with CMEMS reanalysis, for the Northern Adriatic sub-basin. The potential density threshold is 29.2 $\mathrm{kg\,m^{-3}}$.

water, however the cooling event was not so strong as it in 2012 in order to saturate the Northern Adriatic volume. Salinity in L6 was lower than all other experiments, and with spectral nudging the increase in salinity for the new experiment L6+ favoured dense water production with volume analogous to truth L2 and reanalysis. We can speculate that was thus also influenced by remote driver.

Not many in situ data are available for the Northern Adriatic Sea covering all the eight years of experiments. Looking at one specific point at a fixed platform in northeastern coast, time series of temperature and salinity at approximately 2.5 m depth were evaluated in Figure 4.9. We can see some considerable improvements in the root mean squared error (RMSE) and bias of experiment L6+ when compared to L6. Interestingly, at this location no spectral nudging was applied, which means that no correction of tracers has been made directly at this point. The model however would evolve from the remote update of the fields and the inner dynamics respond to that.

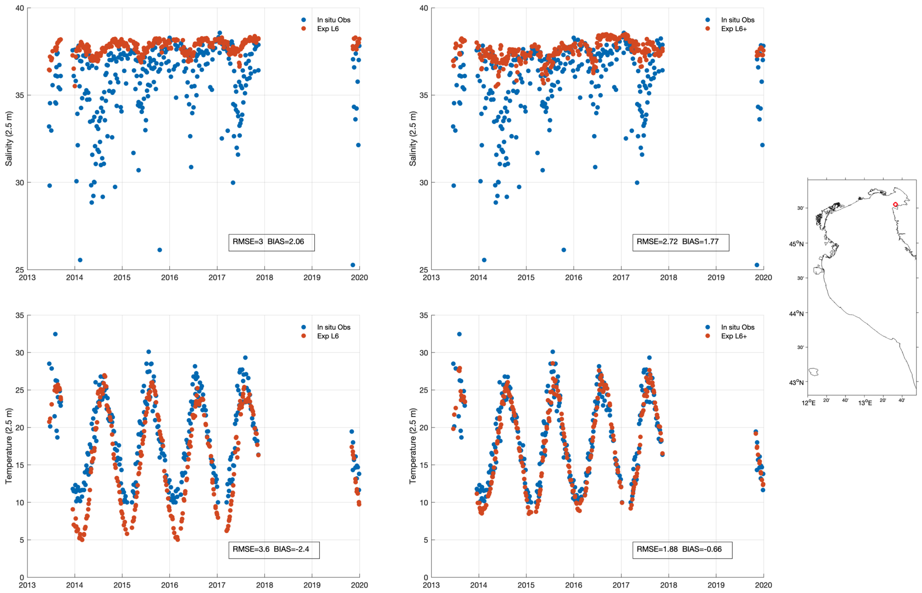

Figure 4.9: Time series of salinity (top) and temperature (bottom) at 2.5 m depth for experiment L6 (left) and L6+ (right) compared with in situ observations from fixed platform (45.5488°N 13.5505°E, indicated by the red mark on map).

Major improvement is observed for temperature, which was underestimated by experiment L6 but much better represented by L6+. In the salinity the RMSE diminishes but not significantly. We have to consider, however, that this is a very coastal station and a single observation at any time of the day, while the model outputs are daily averages. Moreover, we understand that there are sources of uncertainties from river inputs in our model (as covered in Chapter 3.3) such as the prescribed constant salinity or the use of climatologies as it is the case for this particular region, which could be affecting the local salinity too.

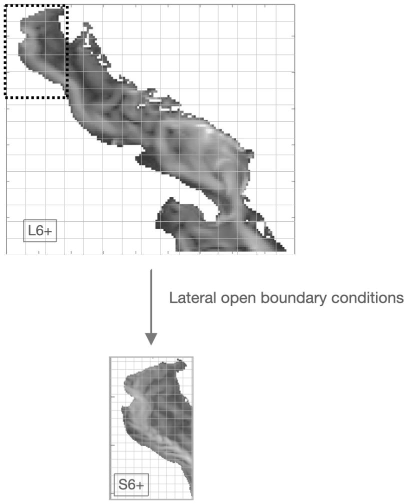

Figure 4.10: Schematic representation of the downscaling experiment S6+ nested in parent L6+. Shading is a daily output of surface velocities, for illustration.

4.4 A new downscaling experiment

Finally, a new downscaling experiment was performed for the Northern Adriatic Sea, again following the methodology proposed in Chapter 2.2.2. This time, however, the new child experiment (S6+) was downscaled from L6+. The experimental design is represented in Figure 4.10.

Temperature and salinity at the fixed platform evidence the improvement of S6+ with respect to former S6 (Figure 4.11). We can assume that the corrected sea water properties of the parent L6+ were able to provide the ideal boundary conditions for the nested experiment. Moreover, with the downscaling the information from the parent experiment propagated towards the inner domain reaching the near coast of the Northern Adriatic Sea.

Since dense water formation on this decade of experiment is much influenced by the external drivers, as it was seen in Chapter 3, we do not expect significant changes between parent (L6+) and child (S6+) experiments. In fact dense water volume in S6+ is quite similar to L6+, although we can see the improvements due to the increase in resolution mainly regarding the years of local forcing influence (Figure 4.12).

In 2012 and 2013 we see the main importance of local atmospheric forcing driving dense water production since all experiments have similar results, with

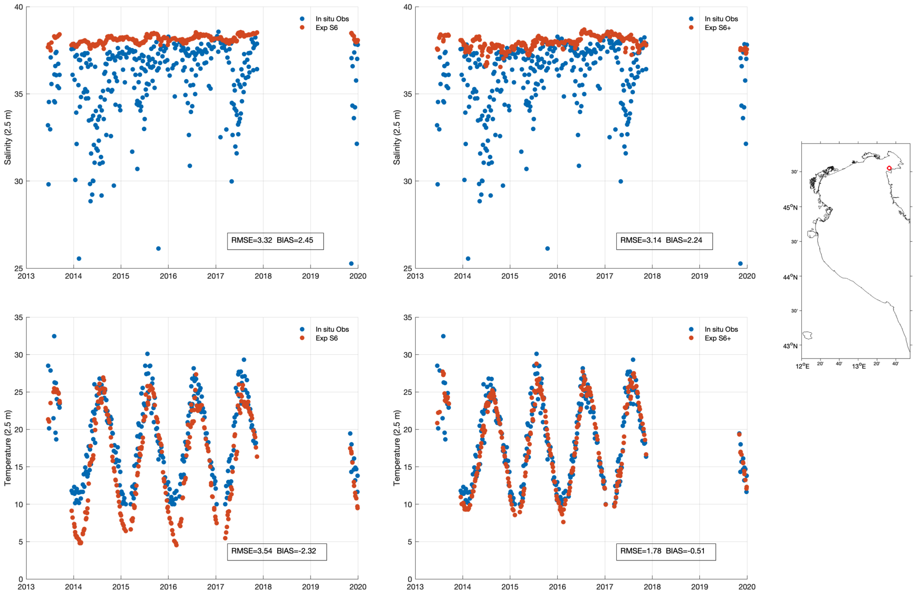

Figure 4.11: Time series of salinity (top) and temperature (bottom) at 2.5 m depth for child experiments S6 (left) and S6+ (right) compared with in situ observations from fixed platform (45.5488°N 13.5505°E, indicated by the red mark on map).

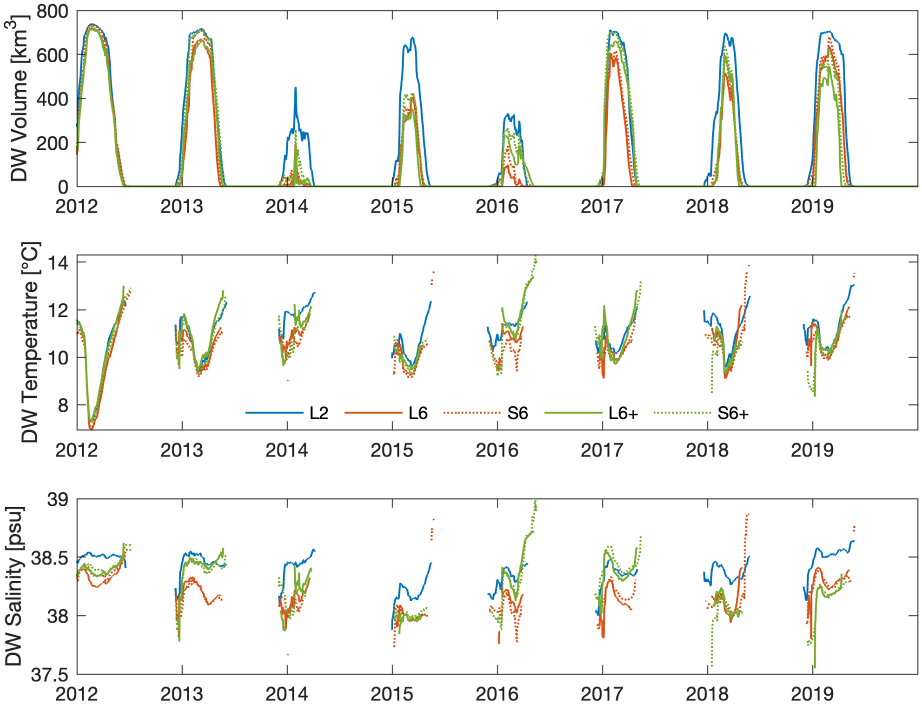

Figure 4.12: Dense water volume (top), temperature (middle) and salinity (bottom) computed for truth L2, parent L6 and L6+, and child S6 and S6+, for the Northern Adriatic sub-basin. The potential density threshold is 29.2 kg m^{-3}.

improved condition in 2013 from the downscaling experiments. In 2017 we again see the influence of both local and external contributors, as the new downscaling experiment S6+, nested in the nudged L6+, is now reaching L2 values which was not achieved by the previous nesting (parent L6 and child S6).

The differences that we see in the new experiment S6+ with respect to L2 are due to the already known differences between truth L2 and CMEMS reanalysis. In years of strong wind outbreaks and large heat loss and evaporation, the local drivers will dominate dense water production in the nested experiment (e.g. 2012, 2013). On the other hand, in periods of mild winters and larger influence of salinity in the basin and external contributors, dense water in the downscaling experiment will follow its parent model conditions (as occurs for most of the period 2014-2019).

This proposed multiple nesting experiment may raise the question on how would an experiment directly nested in CMEMS reanalysis perform. Results and discussion of a new single nesting experiment can be found in Appendix C.2.1.

4.5 Conclusions

The overall aim of this study was to assess the feasibility of spectral nudging for climate predictions in coastal water marine environments. It has been shown by previous studies the importance of this method in downscaling strategies for placing large scales at the correct location. With this experiment we were able to prove that spectral nudging can be useful to improve the thermohaline circulation of the inner domain, known to be limited due to the inner geometry in the model.

As a result of the lack of representation of inner domain features (i.e. inflow of saltier waters at the Otranto Strait), the correct salt transport that enters from the southern open boundary does not propagate from the Ionian towards the Adriatic Sea. Instead of a boundary value problem, we are actually facing an "inner domain problem" related to the geometry of the domain and coarse resolution of the regional model. The spectral nudging thus acts introducing information at the inner domain that should be consistent with what comes from the lateral boundary of the model.

This study was mainly inspired on the work conducted by Katavouta and Thompson (2016), this time implemented to a shallow semi-enclosed bay, i.e. the Adriatic Sea, as an attempt to overcome the "inner value problem" encountered in the model. It is important to highlight that spectral nudging requires that we trust the large scales of the driving model which provides the boundary conditions for our our nested domain. In this case, CMEMS reanalysis consist of trustful fields for the Adriatic Sea and are a good representation of the local tracers.

In reality, “trusting the fields” apply to any forcing in the model, including the lateral boundary conditions and the atmospheric forcing (“garbage in, garbage out” problem, Hall, 2014). However, in spectral nudging it is crucial that we trust the “parent” model fields introduced along the lateral boundaries since the freedom of the nested model is further constrained based on the large scales of those fields.

For a perspective of climate projections we can think of the spectral nudging tool to be applied to restoring large scales towards the parent model. With the scenario of improving thermohaline circulation at complex coastline features, the current outcomes can have broader implications for ameliorating regional to local climate projections beyond the Adriatic Sea.

5 Conclusions and future perspectives

The Perfect Model approach is a methodology largely adopted in atmospheric modelling studies, however with still few applications to ocean studies. It allows to judge the capability of reproducing multi-scale features within a downscaled modelling system. We applied this approach to the Adriatic Sea which is a permanent laboratory for numerical modelling, with coastline complexity and thermohaline variability characterising in particular the Northern sub-basin.

The downscaling exercise here proposed provides useful insights on how to apply the dynamical downscaling methodology to the specific area of interest with the aim of reproducing all the small-scale and large-scale features of the local circulation and dynamics. This study offers the chance to judge the downscaling weaknesses/strengths by looking at the energy budget as well as by analysing specific physical processes.

The energy spectrum analysis served as the scope of judging the reproducibility of multi-scale circulation in the Northern Adriatic and it has been found that with a proper downscaling ratio the energy field is well reproduced. By comparing the downscaled and “truth” experiments within the perfect model framework, a downscaling ratio of 1:3 has proven to be suitable for allowing the regeneration of the kinetic energy in the inner domain. At larger resolution jump (i.e. 1:5), drawbacks associated with the lateral open boundaries are propagated resulting in overshooting of energy at specific frequencies.

The analyses of local physical processes (e.g. the dense water formation) and extreme events (e.g. the marine heat waves occurrence) served the scope of judging the capability of reproducing the thermohaline variability of the Northern Adriatic Sea by looking at the effects of the local drivers at small scales and/or the remote drivers at large scales. The perfect model approach underscores that when remote drivers are missed by the parent model, i.e. the salt water inflow through the Otranto Strait during the cyclonic phase of the Northern Ionian Gyre, the child model fails the reproducibility of local dense water formation.

A second aim of this study is to design a strategy to improve dynamical nesting performance and/or to prevent decouple between parent and child large scales over long simulations. Thus, the application of the spectral nudging technique here proposed is considered a preliminary step towards coastal climate downscaling strategies. It is expected that spectral nudging could be embed in the nesting phase by using the reanalyses fields or the bias corrected results of a global/regional climate model as the boundary forcing. In this way we can prevent decoupling between parent and child models over long simulations, while increasing resolution with respect to available climate drivers at the boundaries.

In this study the low resolution parent experiment, which is forced with reanalysis at the open boundary, has shown to not properly represent the inner domain dynamics. The lack in reproducing the water exchange at the Otranto Strait resulted in unrealistic freshening at the basin. By applying the spectral nudging technique, the large scales of the inner domain tracer fields were nudged towards the reanalysis fields. No change was made to velocity components, and still the circulation (e.g. meridional velocities) at the critical region adjusted accordingly to the updated density field. The entrance of saltier waters with Levantine basin origin during the cyclonic phase of the Northern Ionian Gyre were enhanced, resulting in an overall improvement of the thermohaline properties of the basin. Moreover, even though no further nudging was applied to the subsequent downscaled experiment in the Northern Adriatic Sea, the local fields benefit from the new lateral open boundary conditions coming from the nudged parent model results and they show a substantial better validation.

It is worth to mention that the downscaling exercise here proposed shed light on a specific issue related to the numerical modelling of the Adriatic thermohaline dynamics, investigated after the analysis with the perfect model approach. In fact, by comparing the “truth”, the parent and the child experiments with the reanalyses and with the few available observations in the Northern Adriatic Sea, it has been found that all the experiments are affected by an overestimate of sea surface salinity over some years. We speculate this could be the result of the prescribed constant values of salinity at the river mouths which are based on previous sensitivity study performed over the Adriatic region (Simoncelli et al., 2011) and do not account for seasonal to interannual variability. However, the parent experiment underestimates the salt inflow through the Otranto Strait during the cyclonic phase of the Northern Ionian Gyre, and this may balance the aforementioned overestimate of sea surface salinity, leading to a parent model representing the Northern Adriatic dense water volume only apparently better than the “truth” and the child experiment during some specific years.

As a dilution basin, the Adriatic Sea is sensitive to a proper representation of the river release in terms of runoff, temperature and salinity. These results point out the importance of an integrated modelling of the air-land-sea water cycle for the Adriatic Sea with a specific care of the representation of river discharge, if we want to properly reproduce the high thermohaline variability of this marginal sea and its sub-basins at different time scales.

As a plan for the future, the river release at the land-sea interface is expected to be provided in a more reliable way by coupling the mesoscale ocean model here proposed with an intermediate complexity estuarine box model (Verri et al., 2020, 2021, Maglietta, 2024 under review). It is thus able to solve the estuarine water exchange in terms of volume and tracer fluxes and to provide the net release at the river mouths in a more reliable way.

Finally, the spectral nudging tool, developed to be on-the-fly used by NEMO model, is planned to be shared with the modelling community. Moreover, the potential of the spectral nudging approach, here proven to be a valuable technique for improving nested regional model results, will be further explored within the coastal climate downscaling as it can serve as basis for: (i) training machine learning algorithms to produce downscaled results at very local scales; (ii) computing Pseudo Global Warming (PGW, Brogli et al., 2023) projections.

Table A.1: Model setup

Spatial Discratization	Vertical	- Partial steps z-coordinate - 120 levels (1.2 - 2600 m)	
	Horizontal	- 432 x 331 grid points 144 x 111 grid points 87 x 66 grid points - 2 km (L2) 6 km (L6) 10 km (L10)	
Geographical Configuration	Horizontal Grid	Geographical mesh on the sphere with regular grid-spacing	
	Bathymetry	EMODNET, 3.75 arcsec (2020)	
Physical Choices	Free surface equation	Linear free surface	Time-splitting formulation
	Lateral diffusion scheme for tracers	- Bilaplacean operators - horizontal eddy diffusivity for tracers =	-3.e7 m4/s (L2) -2.43e9 m4/s (L6) -1.8e10 m4/s (L10)
	Lateral diffusion on momentum	- Bilaplacean operator - Horizontal (geopotential) - Horizontal bilaplacian eddy viscosity =	-5.0e7 m4/s (L2) -4.05e9 m4/s (L6) -3.1e10 m4/s (L10)
	Vertical Mixing	TKE turbulent closure scheme to compute vertical eddy viscosity and diffusivity coefficients (turbulent eddy kinetic dependent vertical diffusion)	
	Advection scheme for tracer	MUSCL (Monotone Upstream Scheme for Conservative Laws)	
Initial Conditions (IC) and Boundary Conditions (BC)	IC	T, S bilinearly interpolated to the model grid	CMEMS reanalysis (0.042°)
	Surface BC (temperature, momentum salinity and vertical velocity)	Heat fluxes, wind stress and freshwater flux (E-P-R) based on MFS Bulk formulae (Castellari et al. 1998)	ECMWF analysis (0.125°): all fields ECMWF reanalysis (0.25°): precipitation
	Lateral Open BC	- Flather's scheme for the 2D vel and zero-gradient scheme for SSH - Specified for all 3D variables (interpolation contraint for 3D vel)	CMEMS reanalysis (0.042°)
	River Runoff	SBC: salinity and vertical velocity	- Po River = daily averages of runoff based on observations (const. salinity = 17 psu) - Others (63) = monthly climatological runoff (const. salinity 15 psu) (Verri et al. 2017)
	Lateral Coastal BC	No-slip boundary condition	
	Bottom BC	Nonlinear friction	
Simulation setup and performance	Running procedure	Concatenation procedure with weekly restart	Time-step baroc. & barot.: 120s & 2s (L2); 200s & 3s (L6); 240s & 4s (L10)
	Resource usage	- Run time = 1'14"/day of simulation (L2) and 0'14"/day (L6) - 288 cores	

Appendices

A Supporting material for Chapter 2

A.1 The model setup

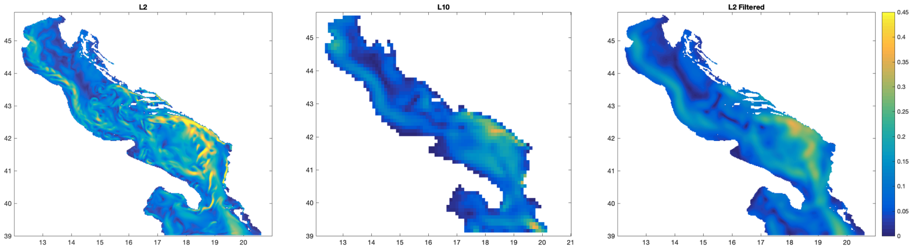

Figure A.1: Winter daily surface velocity $[\mathrm{m\,s^{-1}}]$ field for means of qualitative comparison between for truth L2 (left), parent L10 (middle) and filtered solution L2F (right).

A.2 Complementary figures

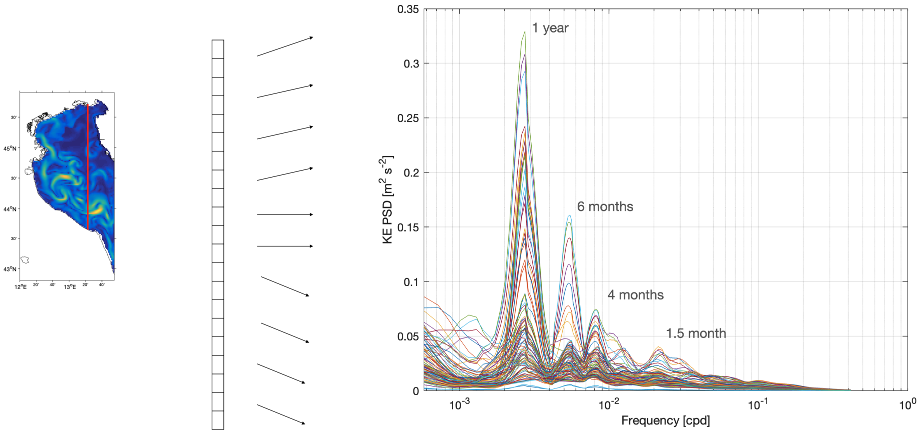

Figure A.2: Schematic representation of how the spectral analysis was performed along the longitudinal transect in the frequency domain [cycles per day]. Middle figure is an illustration of the grid cells along the transect, indicating that the procedure is done for each grid point generating a spread of spectrum (right panel). The spectrum is the resulting PSD of depth averaged eddy velocities, having here S6 experiment as example.

A.3 Kinetic energy under different wind stress computation

For the experiments performed, the wind stress computation used at the surface boundary condition for momentum is based on the relative wind approach. This means that the surface wind stress (τ_s) will be dependent on the difference between the atmospheric wind and the surface ocean velocity according to the following equation:

$$\tau_s = \rho_a c_d |u_w - u_s|(u_w - u_s) \tag{A.1}$$

Where ρ_a is the atmospheric density, c_d is the drag coefficient, u_w is the atmospheric wind and u_s is the ocean surface velocity.

The use of absolute wind approach means that the ocean surface velocity is not considered for the wind stress computation in Equation A.1. The use of absolute wind instead of relative wind approach contributes to higher kinetic energy (approximately 30% increase) since it does not account for the damping effect of the ocean currents (Chassignet et al., 2020). This can be seen by comparison of the two different approaches computed for L6 and S6 experiments in Figure A.3.

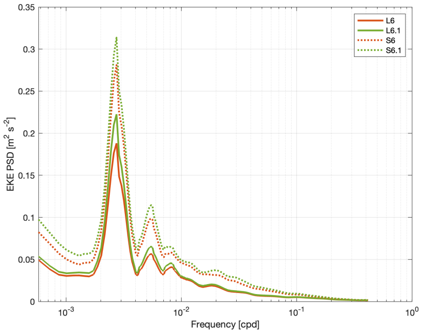

(a) (b)

Figure A.3: Power spectral density of eddy velocity in the time (frequency) domain [cycles per day], computed for surface (a) and depth average (b). Solid and dashed lines indicate parent and child experiments, respectively; in orange (green) there are the experiments with relative (absolute) wind stress formulation.

The motivation of this analysis was to understand the different peaks of energy in the spectral analysis (Figure 2.7), especially the overshooting of energy identified mainly in the large downscaling ratio strategies. With this we, however, also able to evaluate if the different horizontal resolution of the ocean model would imply in distinct "damping" effect when moving from absolute to relative approach formulation.

Although these results are not decisive for the discussion on the energy spectrum, some interesting results were identified and are worth to be mentioned. We identified that moving to the relative wind approach in a high resolution model (e.g. S6) corresponds to overall larger damping effect in most frequencies when compared to a coarse resolution model (e.g. L6). This, however, is not true for all frequencies, since in some cases the damping effect was basically the same for both experiments case.

This was just a test study, but it can be assumed though that the representation of the mesoscale features by higher resolution model probably contribute to slightly stronger damping effect. Further studies would still be necessary for concluding remarks, relying on extensive review of literature on this topic (e.g. Munday et al., 2021; Renault et al., 2016, 2020). We presented here some insights for future work perspectives to be considered.

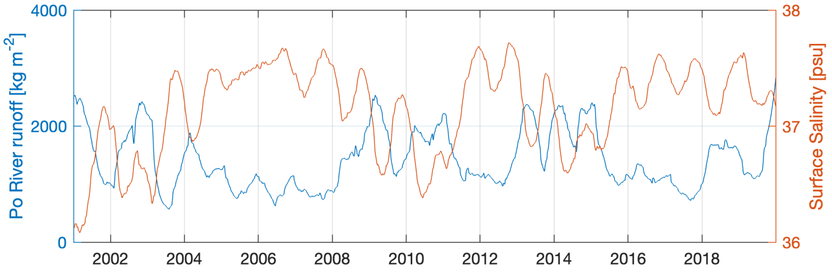

Figure B.1: Time series of daily values for Po River discharge and basin average surface salinity computed for truth L2, in the Northern Adriatic Sea domain (Correlation between the two fields is -0.68).

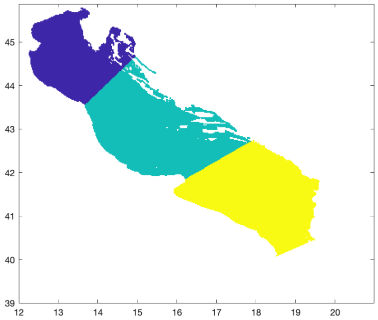

Figure B.2: Delimitation of Northern, Middle and Southern Adriatic sub-basins, used for the dense water computation of the large domain experiments covering the entire Adriatic Sea.

B Supporting material for Chapter 3

B.1 Complementary figures

B.2 Further discussion on dense water formation

In order to evaluate our nesting setup and nesting approach, dense water formation of other two nesting strategies were computed: parent L2 and child S0, and parent L2F and child S2 (more information on the experiments setup is available in Chapter 2).

In Figure B.3 we can demonstrate that the dense water volume of each child experiment overlaps with truth L2. Actually no differences are seen among all experiments, indicating that filtered lateral open boundary conditions in L2F were able to provide the necessary sea water properties for preconditioning dense

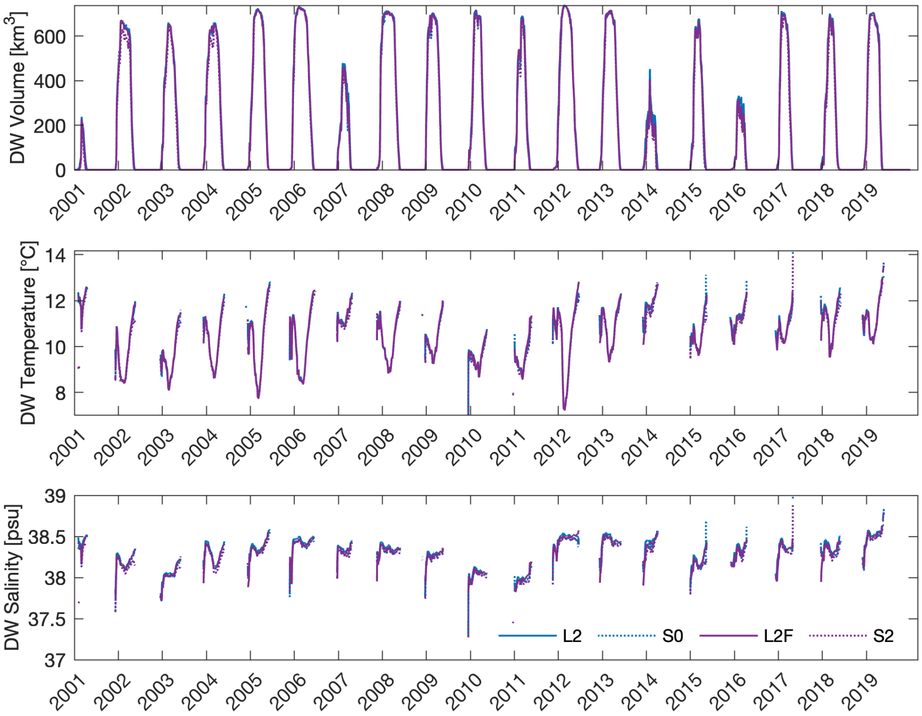

Figure B.3: Dense water volume (top), temperature (middle) and salinity (bottom) computed for each experiment for the area covered by the nesting experiments in the Northern Adriatic Sea. Solid and dashed lines represent, respectively, parent and child experiments.

water formation. We can also assume that instabilities that could be associated with the implementation of the boundaries did not affect the mean dense water computation since there is complete agreement between experiments.

With the very coarse model L10 we found major discrepancies in the overall salinity of the basin (Figure B.4). Firstly, due to the misrepresentation of the salt water intrusion through the Otranto Strait, as also reported for L6. For L10, however, the disparity was even larger since the resolution was considerably low (10 km for L10). Moreover, the mixing processes and the representation of river plume in the coarse L10 is very limited, compromising the thermohaline properties of the basin for the entire period of simulation and in large proportions after the reversal of the BiOS regime to cyclonic phase (2012-2019).

Figure B.5 contains maps of salinity at 150 m in the Mediterranean Sea, covering different periods of anticyclonic and cyclonic phases of the NIG. During the anticyclonic phase, as can be seen from the top panel, clockwise circulation

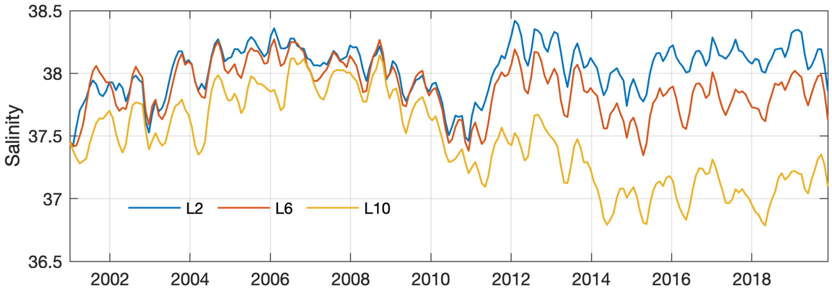

Figure B.4: Basin average salinity for "truth" L2, parent L6 and parent L10 computed for the area covered by the downscaling Northern Adriatic sub-domain.

in the Ionian Sea contributes to western less saltier waters with Atlantic origin to spread towards the Northern Ionian Sea. Under this regime, waters entering the Adriatic Sea have a much larger influence of the western Mediterranean waters, contributing to a decrease of salinity in the basin.

During the cyclonic phase, exemplified by the bottom panel, anticlockwise circulation favors eastern saltier waters with Levantine origin to enter the Adriatic Sea. This contributes to an increase in salinity in the Adriatic basin. The less saline waters from the western Mediterranean under this influence flow at a much narrower path along the southern coastline of the Mediterranean.

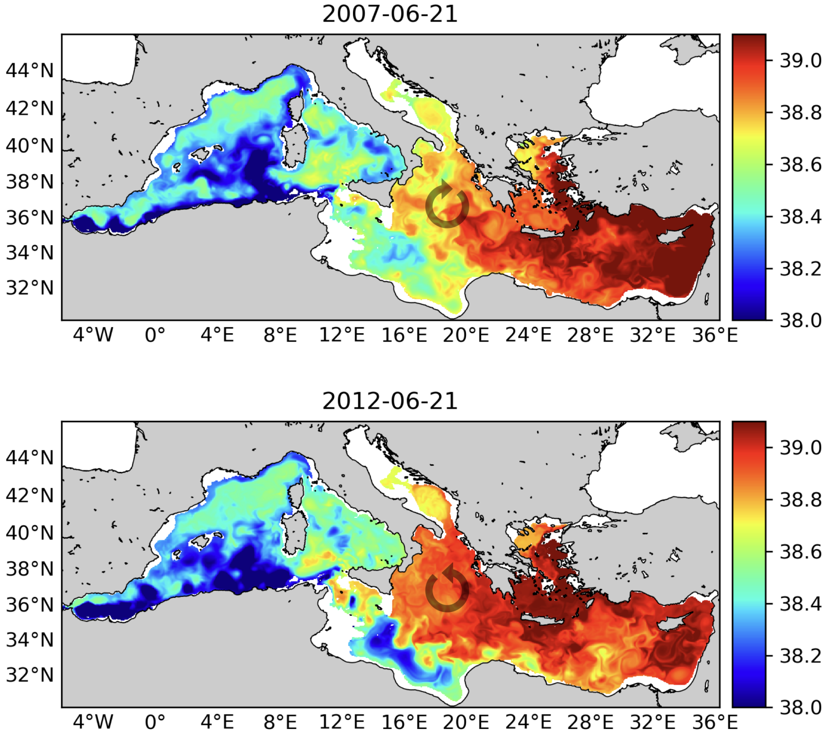

Figure B.5: Salinity [psu] at 150 m from reanalysis of the Copernicus Marine Service for the entire Mediterranean Sea, during periods of anticyclonic (top) and cyclonic (bottom) circulation phase of the Northern Ionian Gyre (NIG).

C Supporting material for Chapter 4

C.1 Spectral nudging implementation on the fly

This section describes the spectral nudging tool developed for NEMO ocean model and its technical specifications.

The procedure was prepared to be entirely performed on the fly, meaning that no pre-processing is needed for the parent model fields to be used by the tool. We need to specify the time step (Δt_{sn}) that we wish the spectral nudging to be applied and the fields will be provided from the namelist of the model. The way the parent model fields are used as inputs for the tool is similar to the way NEMO reads the atmospheric forcing fields and interpolates to the model grid with the use of a weights file. In the same way, the frequency of the fields is provided so that the procedure will interpolate in time to the model time step.

Before applying any filtering or interpolation, the parent model field is flooded, i.e. the ocean fields are extrapolated to land to avoid inconsistencies on sea/land points between parent and nested domain. For that it is necessary to provide a land-sea mask of the parent model. The decision on how many iterations will be performed for the flooding are stipulated by the namelist as well. This step will actually considerably affect the computational time of the procedure, so a reasonable but not exaggerated number of iterations should be set.

After that, the new "flooded" field is horizontally interpolated to the model grid using a weight file to be provided. For this study bi-linear interpolation was applied on tracers, and it is done for each vertical layer. At the end, the field is finally linear interpolated in the vertical coordinate to the vertical levels of the model grid. At this step it is optional to vertically extrapolate at the bottom (further details on this procedure in C.1.1).

Now that we have parent and nested fields at the same grid spacing, the difference between them is performed. To avoid large computational cost, this step is done previously so that the filtering is done only once (see C.1.2 for further discussion on the linearity of this step). The choice of filter coefficients need to be decided primary and provided at the tool. It is recommended to perform some sensitivity tests offline in order to decide for the best filtering option to the particular area of study.

The filter is then applied to the difference resulted from the previous step, and with that we obtain a correction factor for each region. The final equation will condition this correction as dependent on the nudging coefficient γ (Equation 4.5), composed of a constant parameter γ_0 (set to increase or reduce the nudging at same proportion in the domain) and a space varying parameter $\Gamma(x, y, z)$ (stipulates the strength of the nudging depending on the grid position). The three-dimensional nudging parameter $\Gamma(x, y, z)$ is provided also through the namelist as a mask file for the model domain (Section 4.2.2).

The model field is finally updated, at each spectral nudging time step Δt_{sn}, with the correction factor multiplied by the nudging coefficient, as it is seen in Equations 4.1 and 4.2.

C.1.1 Interpolation and flooding at complex bathymetry

In the same way that horizontal interpolation can lead to inconsistencies in the coastlines, when interpolating in the vertical the same attention needs to be done for the bathymetry. Here we show how different approaches in the flooding procedure (i.e. extrapolating sea into land point) can lead to different results at the bottom grid cells.

A flooding procedure is performed for the interpolation to be sure that sea points are exactly the same in the model mask and the interpolated field. However, if the bathymetry differs considerably, some inconsistencies may occur next to the bottom. The flooding procedure, also called “sea over land”, consists in extrapolating the sea points over the land points. With this horizontal flooding, land points that are shifting to ocean point will get an average value of the closest sea points horizontally.

This step needs to be evaluated carefully, as it can be seen in Figure C.1, which contains interpolated reanalysis fields at a section along latitude 42.62°N following two different approaches. We can thus compare them with the original reanalysis field at the bottom image.

The top panel corresponds to the horizontal flooding where bottom values are extrapolated horizontally so that previous land features that would turn to ocean in the new model grid are filled based on the average close horizontal grids. The disadvantage of this method is that you may be filling local grid cells with far oceanic fields at deep regions in the domain; this can be seen around longitude 17.5°E, where bottom temperature is filled with the closest horizontal feature which corresponds to rather far away 16.5°E longitude.

The vertical approach will extrapolate bottom land grid towards its upper ocean field. With this strategy the issue observed previously at longitude 17.5°E

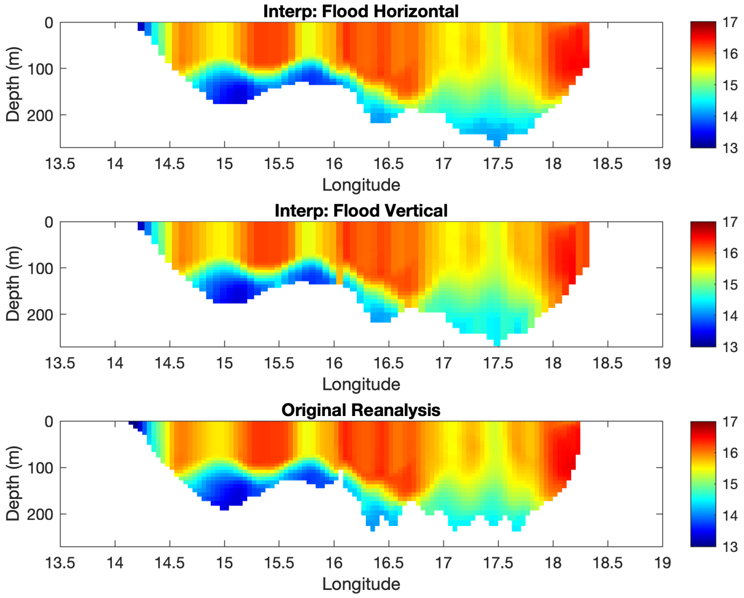

Figure C.1: Example of reanalysis field (temperature) interpolated to the model grid by using the horizontal extrapolation (top panel) or the vertical extrapolation (middle panel). Bottom panel is the original reanalysis grid.

is solved and better represented. But instead, we can notice that at longitude 16°E the extrapolation causes undesired warming of deeper layers. In this case the opposite is happening, since now we have a protuberance (e.g. sea mount) at the original reanalysis bathymetry which is not present in the smoothed model topography. And for this situation the vertical extrapolation is not ideal.

The idea here was not to provide the perfect solution, but instead to address some issues that have been faced. As some of them may vary depending on the domain and the model choices, it was important to point out some problems which may have different ideal solutions. Therefore, there is no right or wrong procedure, but instead the user needs to be aware of the best approach to be implemented for the respective domain of study.

C.1.2 The linearity of the spectral nudging increment

In this experimental study we can demonstrate the linearity of the relationship for the spectral nudging increment, i.e.: $\langle T_t^{PM} - D_t(T_{t-1})\rangle_L$ is equal to $\langle T_t^{PM}\rangle_L - \langle D_t(T_{t-1})\rangle_L$. The linear property of the Butterworth filter is an advantage that also justify its choice, since in general other filters may not act as

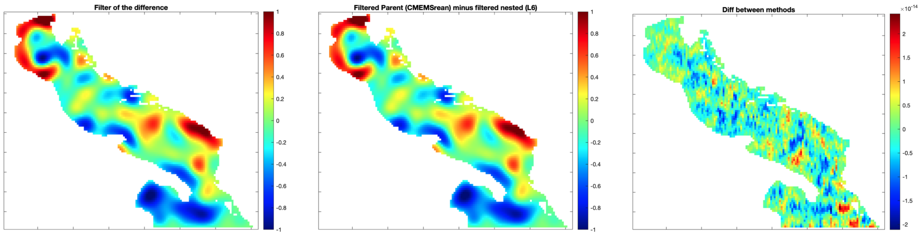

Figure C.2: Example of two different methods for computing the temperature increment for spectral nudging: filter of the difference between the fields (left), difference of the filtered fields (middle). Right panel corresponds to the difference between results of the two approaches. Note the differences in colorbar between the first two panels and the last panel, where values are of the order of 10^{-14} and are essentially noise.

linear operators.

For a specific time step the nudging increment was performed in two different ways: the first one is by calculating the difference between parent and child fields, and filtering this difference afterwards; the second one is by filtering each of the models separately, and computing the difference of the filtered fields subsequently. From Figure C.2 we can show that the results do not differ.

The second approach, however, requires higher computational time since the filtering procedure is performed twice. Therefore, the spectral nudging tool here described follows the first approach, in order to make the process more efficient.

C.2 Additional discussion on thermohaline properties

Figure C.3 illustrates salinity fields from the different experiments as proposed in Figure 4.4, with addition of the CMEMS reanalysis fields for comparison purposes. Near surface results (top panels) evidence very low influence of the spectral nudging applied to L6+, with larger differences when compared with CMEMS reanalysis. At the deeper layer of 150 m (bottom panels), however, where the nudging was stronger, L6+ shares strong similarities with the driving reanalysis fields, as expected. Truth L2 is probably capable of correctly representing the eddy fields and the flow along the Otranto Strait.

These results were surely expected since no spectral nudging was applied at the coast and surface levels (0 to 50m), and it was stronger at 150 m. However, they are also evidence of the driving mechanism of our surface boundary conditions (i.e. atmospheric forcing and rivers) at the surface fields, even in the

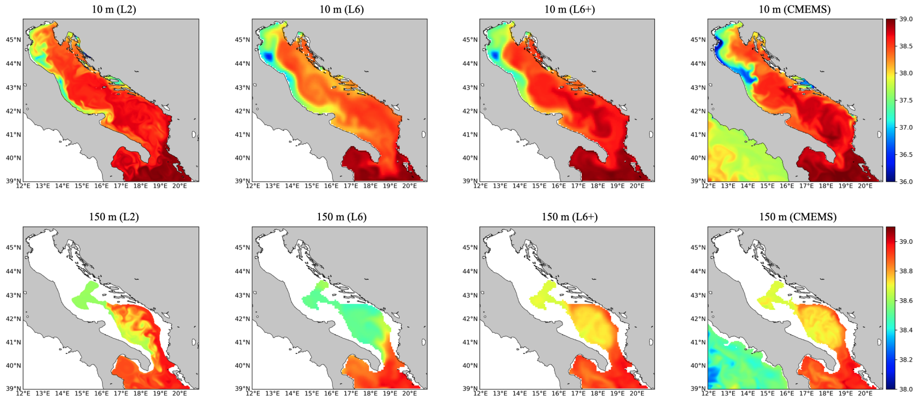

Figure C.3: Maps of salinity at 10 m (top panels) and at 150 m depth (bottom panels) for experiments L2, L6 and L6+ (first panels), compared with CMEMS reanalysis (right panels) in 21/06/2012. (Updated color bar with depth).

nudged experiment L6+. This means that the original surface fields signal is not missed after the spectral nudging. It is understood that comparison with truth L2 is less straightforward in this case, however it can be still successfully used as a benchmark for evaluating L6+.

C.2.1 A new downscaling experiment in single nesting approach

A new downscaling experiment (S4R) in the Northern Adriatic Sea was performed, directly nested in CMEMS reanalysis as a single nesting strategy. As expected, the new experiment S4R results are in good agreement with previous S6+ (Figure C.4). Temperature results in both cases share strong similarities, and for salinity there is a slight improvement on the statistics of the new experiment S4R (BIAS and RMSE values can be seen in each figure panel). This is a quite expected result, as the observations used for comparison are the same that have been assimilated to build the CMEMS reanalysis.

Similarly, by focusing on dense water formation analysis, results of both downscaling experiments S6+ and S4R are quite similar (Figure C.4). This is again expected and it is also a confirmation that the spectral nudging procedure developed for creating S6+ is working properly.

The only year with more relevant differences is 2014. For this particular year very low dense water volume was computed according to our previous experiments, even less for CMEMS reanalysis (Figure 4.12). Since there is no spectral nudging applied to the surface layers on L6+, it can be assumed that the differences in dense water volume in the two downscaling experiments (S6+ and S4R) are probably due to local drivers.

It is important to clarify that the multiple nesting strategy in our study, with intermediate L6+, was not intended at providing the best downscaling approach for our system. The large domain L6+ proposed previously addresses the benefit of the spectral nudging tool for overcoming known systematic errors in nested experiments, for example. The limitations encountered for coarse experiment L6 raised the question whether a better solution could be developed with the same experimental setup. Indeed, the application of spectral nudging to the parent L6 (creating L6+) contributed to significant improvements in terms of representation of the large scales inner domain features. The further downscaling experiment S6+ could afterwards benefit from the improved parent experiment.

Additionally, the reanalysis resolution available in this study area is reasonably high (4.5 km) and close to the child experiment (2 km). Even if not directly shown by these experiments, the proposed results hint that potential benefits may arise in coastal areas not covered by observations and/or with proposed downscaling reaching horizontal resolution much higher than the available reanalysis resolution.

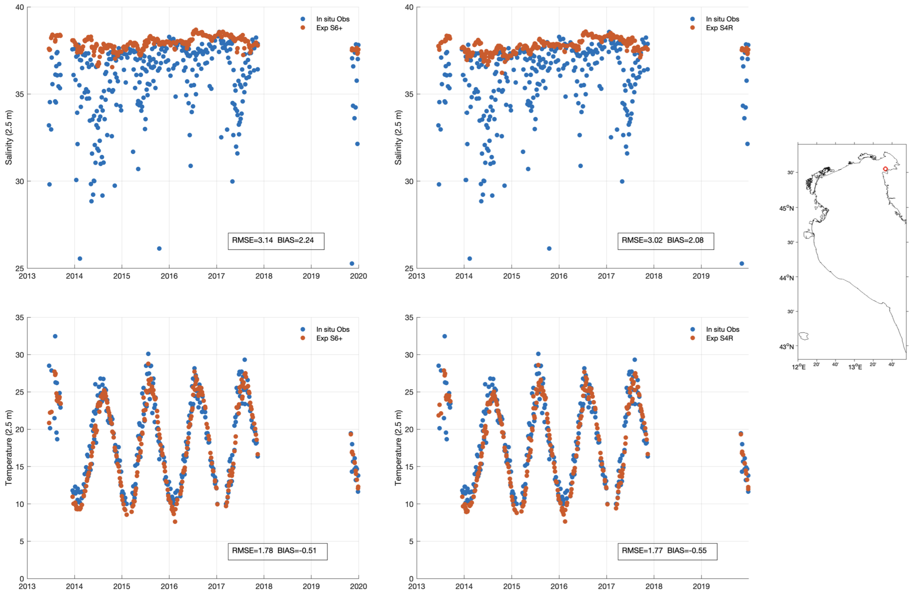

Figure C.4: Time series of salinity (top) and temperature (bottom) at 2.5 m depth for multiple nesting (boundary conditions from L6+) downscaling experiment S6+ (left) and single nesting (boundary conditions from CMEMS reanalysis) S4R (right) compared with in situ observations from fixed platform (45.5488°N 13.5505°E, indicated by the red mark on map).

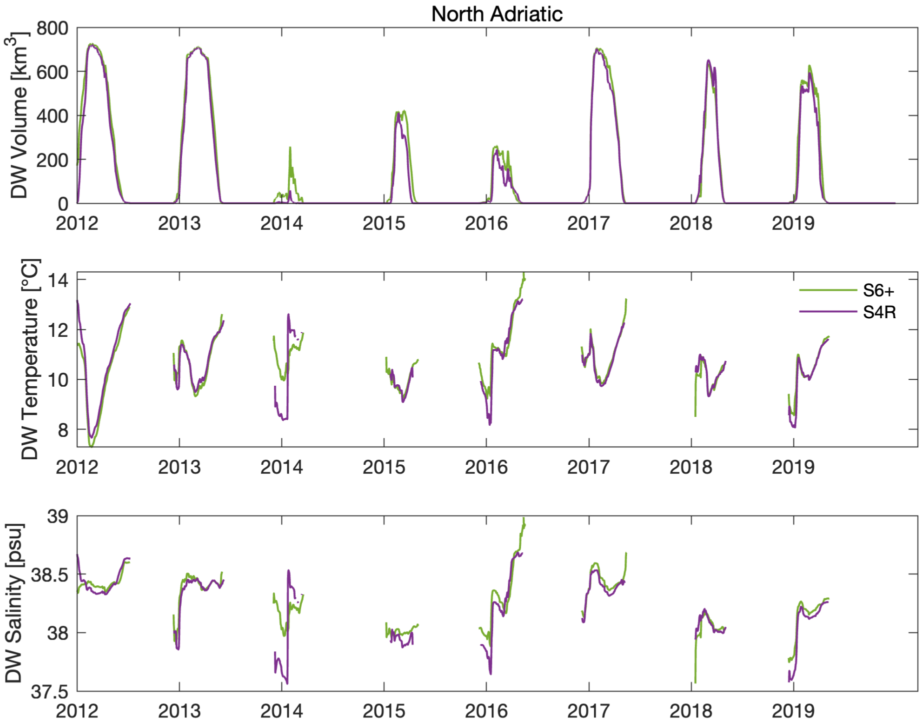

Figure C.5: Dense water volume (top), temperature (middle) and salinity (bottom) computed for the Northern Adriatic sub-basin, for multiple nesting (boundary conditions from L6+) downscaling experiment S6+ and single nesting (boundary conditions from CMEMS reanalysis) S4R. The potential density threshold is 29.2 $\mathrm{kg\,m^{-3}}$.

References

Artegiani, A., Paschini, E., Russo, A., Bregant, D., Raicich, F., & Pinardi, N. (1997a). The adriatic sea general circulation. part i: Air–sea interactions and water mass structure. *Journal of physical oceanography*, *27*(8), 1492–1514.

Artegiani, A., Paschini, E., Russo, A., Bregant, D., Raicich, F., & Pinardi, N. (1997b). The adriatic sea general circulation. part ii: Baroclinic circulation structure. *Journal of physical Oceanography*, *27*(8), 1515–1532.

Astraldi, M., Balopoulos, S., Candela, J., Font, J., Gacic, M., Gasparini, G., Manca, B., Theocharis, A., & Tintoré, J. (1999). The role of straits and channels in understanding the characteristics of mediterranean circulation. *Progress in oceanography*, *44*(1-3), 65–108.

Belušić Vozila, A., Güttler, I., Ahrens, B., Obermann-Hellhund, A., & Telišman Prtenjak, M. (2019). Wind over the adriatic region in cordex climate change scenarios. *Journal of Geophysical Research: Atmospheres*, *124*(1), 110–130.

Bergamasco, A., Gačić, M., Boscolo, R., & Umgiesser, G. (1996). Winter oceanographic conditions and water mass balance in the northern adriatic (february 1993). *Journal of marine systems*, *7*(1), 67–94.

Borzelli, G. L. E., Gačić, M., Cardin, V., & Civitarese, G. (2009). Eastern mediterranean transient and reversal of the ionian sea circulation. *Geophysical Research Letters*, *36*(15).

Brogli, R., Heim, C., Mensch, J., Sørland, S. L., & Schär, C. (2023). The pseudo-global-warming (pgw) approach: Methodology, software package pgw4era5 v1. 1, validation, and sensitivity analyses. *Geoscientific Model Development*, *16*(3), 907–926.

Bruciaferri, D., Guiavarc'h, C., Hewitt, H. T., Harle, J., Almansi, M., & Mathiot, P. (2023). Localised general vertical coordinates for quasi-eulerian ocean models: The nordic overflows test-case. *Authorea Preprints*.

Cardin, V., Bensi, M., & Pacciaroni, M. (2011). Variability of water mass properties in the last two decades in the south adriatic sea with emphasis on the period 2006–2009. *Continental Shelf Research*, *31*(9), 951–965.

Castellari, S., Pinardi, N., & Leaman, K. (1998). A model study of air–sea interactions in the mediterranean sea. *Journal of Marine Systems*, *18*(1-3), 89–114.

Chassignet, E. P., & Xu, X. (2017). Impact of horizontal resolution (1/12 to 1/50) on gulf stream separation, penetration, and variability. *Journal of Physical Oceanography*, *47*(8), 1999–2021.

Chassignet, E. P., Yeager, S. G., Fox-Kemper, B., Bozec, A., Castruccio, F., Danabasoglu, G., Horvat, C., Kim, W. M., Koldunov, N., Li, Y., et al. (2020). Impact of horizontal resolution on global ocean–sea ice model simulations based on the experimental protocols of the ocean model intercomparison project phase 2 (omip-2). *Geoscientific Model Development*, *13*(9), 4595–4637.

Colombo, P., Barnier, B., Penduff, T., Chanut, J., Deshayes, J., Molines, J.-M., Le Sommer, J., Verezemskaya, P., Gulev, S., & Treguier, A.-M. (2020). Representation of the denmark strait overflow in a z-coordinate eddying configuration of the nemo (v3. 6) ocean model: Resolution and parameter impacts. *Geoscientific Model Development*, *13*(7), 3347–3371.

Cushman-Roisin, B., Gacic, M., Poulain, P.-M., & Artegiani, A. (2013). *Physical oceanography of the adriatic sea: Past, present and future*. Springer Science & Business Media.

Cushman-Roisin, B., Korotenko, K. A., Galos, C. E., & Dietrich, D. E. (2007). Simulation and characterization of the adriatic sea mesoscale variability. *Journal of Geophysical Research: Oceans*, *112*(C3).

De Elia, R., Laprise, R., & Denis, B. (2002). Forecasting skill limits of nested, limited-area models: A perfect-model approach. *Monthly Weather Review*, *130*(8), 2006–2023.

Debreu, L., Vouland, C., & Blayo, E. (2008). Agrif: Adaptive grid refinement in fortran. *Computers & Geosciences*, *34*(1), 8–13.

Denamiel, C., Tojčić, I., Pranić, P., & Vilibić, I. (2022). Modes of the bios-driven adriatic sea thermohaline variability. *Climate Dynamics*, *59*(3-4), 1097–1113.

Denis, B., Laprise, R., Caya, D., & Côté, J. (2002). Downscaling ability of one-way nested regional climate models: The big-brother experiment. *Climate Dynamics*, *18*, 627–646.

Elzahaby, Y., & Schaeffer, A. (2019). Observational insight into the subsurface anomalies of marine heatwaves. *Frontiers in Marine Science*, *6*, 745.

Escudier, R., Clementi, E., Cipollone, A., Pistoia, J., Drudi, M., Grandi, A., Lyubartsev, V., Lecci, R., Aydogdu, A., Delrosso, D., et al. (2021). A high resolution reanalysis for the mediterranean sea. *Frontiers in Earth Science*, *9*, 702285.

Eusebi Borzelli, G. L., & Carniel, S. (2023). A reconciling vision of the adriatic-ionian bimodal oscillating system. *Scientific Reports*, *13*(1), 2334.

Ferentinos, G., & Kastanos, N. (1988). Water circulation patterns in the otranto straits, eastern mediterranean. *Continental Shelf Research*, *8*(9), 1025–1041.

Ferrari, R., & Wunsch, C. (2009). Ocean circulation kinetic energy: Reservoirs, sources, and sinks. *Annual Review of Fluid Mechanics*, *41*, 253–282.

Flather, R. (1976). A tidal model of the northwest european continental shelf. *Mem. Soc. Roy. Sci. Liege*, *10*, 141–164.

Fofonoff, N. P., & Millard, R. C. (1983). Algorithms for computation of fundamental properties of seawater. *UNESCO Technical Papers in Marine Science= Documents techniques de l'Unesco sur les sciences de la mer.*

Fox-Kemper, B., Adcroft, A., Böning, C. W., Chassignet, E. P., Curchitser, E., Danabasoglu, G., Eden, C., England, M. H., Gerdes, R., Greatbatch, R. J., et al. (2019). Challenges and prospects in ocean circulation models. *Frontiers in Marine Science*, *6*, 65.

Frigo, M., & Johnson, S. G. (2005). The design and implementation of fftw3. *Proceedings of the IEEE*, *93*(2), 216–231.

Gačić, M., Borzelli, G. E., Civitarese, G., Cardin, V., & Yari, S. (2010). Can internal processes sustain reversals of the ocean upper circulation? the ionian sea example. *Geophysical research letters*, *37*(9).

Gačić, M., Civitarese, G., Kovačević, V., Ursella, L., Bensi, M., Menna, M., Cardin, V., Poulain, P.-M., Cosoli, S., Notarstefano, G., et al. (2014). Extreme winter 2012 in the adriatic: An example of climatic effect on the bios rhythm. *Ocean Science*, *10*(3), 513–522.

Gačić, M., Ursella, L., Kovačević, V., Menna, M., Malačič, V., Bensi, M., Negretti, M.-E., Cardin, V., Orlić, M., Sommeria, J., et al. (2021). Impact of dense-water flow over a sloping bottom on open-sea circulation: Laboratory experiments and an ionian sea (mediterranean) example. *Ocean Science*, *17*(4), 975–996.

García-Herrera, R., Díaz, J., Trigo, R. M., Luterbacher, J., & Fischer, E. M. (2010). A review of the european summer heat wave of 2003. *Critical Reviews in Environmental Science and Technology*, *40*(4), 267–306.

Gascard, J. (1978). Mediterranean deep-water formation baroclinic instability and oceanic eddies. *Oceanologica Acta*, *1*(3), 315–330.

Grilli, F., & Pinardi, N. (1998). The computation of rossby radii of deformation for the mediterranean sea. *MTP news*, *6*(4), 4–5.

Guarnieri, A., Pinardi, N., Oddo, P., Bortoluzzi, G., & Ravaioli, M. (2013). Impact of tides in a baroclinic circulation model of the adriatic sea. *Journal of Geophysical Research: Oceans*, *118*(1), 166–183.

Gunduz, M., Dobricic, S., Oddo, P., Pinardi, N., & Guarnieri, A. (2013). Impact of levantine intermediate water on the interannual variability of the adriatic sea based on simulations with a fine resolution ocean model. *Ocean Modelling*, *72*, 253–263.

Haid, V., Stanev, E. V., Pein, J., Staneva, J., & Chen, W. (2020). Secondary circulation in shallow ocean straits: Observations and numerical modeling of the danish straits. *Ocean Modelling*, *148*, 101585.

Hall, A. (2014). Projecting regional change. *Science*, *346*(6216), 1461–1462.

Hallberg, R. (2013). Using a resolution function to regulate parameterizations of oceanic mesoscale eddy effects. *Ocean Modelling*, *72*, 92–103.

Hersbach, H., Bell, B., Berrisford, P., Hirahara, S., Horányi, A., Muñoz-Sabater, J., Nicolas, J., Peubey, C., Radu, R., Schepers, D., et al. (2020). The era5 global reanalysis. *Quarterly Journal of the Royal Meteorological Society*, *146*(730), 1999–2049.

Hobday, A. J., Alexander, L. V., Perkins, S. E., Smale, D. A., Straub, S. C., Oliver, E. C., Benthuysen, J. A., Burrows, M. T., Donat, M. G., Feng, M., et al. (2016). A hierarchical approach to defining marine heatwaves. *Progress in Oceanography*, *141*, 227–238.

Hoffman, R. N., & Atlas, R. (2016). Future observing system simulation experiments. *Bulletin of the American Meteorological Society*, *97*(9), 1601–1616.

Holbrook, N. J., Scannell, H. A., Sen Gupta, A., Benthuysen, J. A., Feng, M., Oliver, E. C., Alexander, L. V., Burrows, M. T., Donat, M. G., Hobday, A. J., et al. (2019). A global assessment of marine heatwaves and their drivers. *Nature communications*, *10*(1), 2624.

Hurlburt, H. E., Chassignet, E. P., Cummings, J. A., Kara, A. B., Metzger, E. J., Shriver, J. F., Smedstad, O. M., Wallcraft, A. J., & Barron, C. N. (2008). Eddy-resolving global ocean prediction. *Ocean Modeling in an Eddying Regime, Geophysical Monograph*, *177*, 353–381.

Ivatek-Sahdan, S., & Tudor, M. (2004). Use of high-resolution dynamical adaptation in operational suite and research impact studies. *Meteorologische Zeitschrift*, *13*(2), 99–108.

Janeković, I., Mihanović, H., Vilibić, I., & Tudor, M. (2014). Extreme cooling and dense water formation estimates in open and coastal regions of the adriatic sea during the winter of 2012. *Journal of Geophysical Research: Oceans*, *119*(5), 3200–3218.

Jerlov, N. G. (1976). *Marine optics*. Elsevier.

Juza, M., Fernández-Mora, À., & Tintoré, J. (2022). Sub-regional marine heat waves in the mediterranean sea from observations: Long-term surface changes, sub-surface and coastal responses. *Frontiers in Marine Science*, *9*, 785771.

Katavouta, A., & Thompson, K. R. (2016). Downscaling ocean conditions with application to the gulf of maine, scotian shelf and adjacent deep ocean. *Ocean Modelling*, *104*, 54–72.

Killworth, P. D. (1996). Time interpolation of forcing fields in ocean models. *Journal of physical oceanography*, *26*(1), 136–143.

Liu, F., Mikolajewicz, U., & Six, K. D. (2022). Drivers of the decadal variability of the north ionian gyre upper layer circulation during 1910–2010: A regional modelling study. *Climate Dynamics*, *58*(7-8), 2065–2077.

Liu, Y., Donat, M. G., Rust, H. W., Alexander, L. V., & England, M. H. (2019). Decadal predictability of temperature and precipitation means and extremes in a perfect-model experiment. *Climate Dynamics*, *53*, 3711–3729.

Madec, G., Bourdallé-Badie, R., Bouttier, P.-A., Bricaud, C., Bruciaferri, D., Calvert, D., Chanut, J., Clementi, E., Coward, A., Delrosso, D., et al. (2017). Nemo ocean engine.

Malačič, V., Viezzoli, D., & Cushman-Roisin, B. (2000). Tidal dynamics in the northern adriatic sea. *Journal of Geophysical Research: Oceans*, *105*(C11), 26265–26280.

Manca, B., Ibello, V., Pacciaroni, M., Scarazzato, P., & Giorgetti, A. (2006). Ventilation of deep waters in the adriatic and ionian seas following changes in thermohaline circulation of the eastern mediterranean. *Climate Research*, *31*(2-3), 239–256.

Manca, B., Kovaĉević, V., Gaĉić, M., & Viezzoli, D. (2002). Dense water formation in the southern adriatic sea and spreading into the ionian sea in the period 1997–1999. *Journal of Marine Systems*, *33*, 133–154.

Marchesiello, P., McWilliams, J. C., & Shchepetkin, A. (2001). Open boundary conditions for long-term integration of regional oceanic models. *Ocean modelling*, *3*(1-2), 1–20.

Marshall, J., & Plumb, R. A. (1989). *Atmosphere, ocean and climate dynamics: An introductory text*. Academic Press.

Masina, S., & Pinardi, N. (1994). Mesoscale data assimilation studies in the middle adriatic sea. *Continental Shelf Research*, *14*(12), 1293–1310.

Masutani, M., Schlatter, T. W., Errico, R. M., Stoffelen, A., Andersson, E., Lahoz, W., Woollen, J. S., Emmitt, G. D., Riishøjgaard, L.-P., & Lord, S. J. (2010). Observing system simulation experiments. *Data Assimilation: Making sense of observations*, 647–679.

Mihanović, H., Vilibić, I., Carniel, S., Tudor, M., Russo, A., Bergamasco, A., Bubić, N., Ljubešić, Z., Viličić, D., Boldrin, A., et al. (2013). Exceptional dense water formation on the adriatic shelf in the winter of 2012. *Ocean science*, *9*(3), 561–572.

Munday, D. R., Zhai, X., Harle, J., Coward, A. C., & Nurser, A. G. (2021). Relative vs. absolute wind stress in a circumpolar model of the southern ocean. *Ocean Modelling*, *168*, 101891.

Oddo, P., & Guarnieri, A. (2011). A study of the hydrographic conditions in the adriatic sea from numerical modelling and direct observations (2000–2008). *Ocean Science*, *7*(5), 549–567.

Oddo, P., Pinardi, N., & Zavatarelli, M. (2005). A numerical study of the interannual variability of the adriatic sea (2000–2002). *Science of the Total Environment*, *353*(1-3), 39–56.

Olita, A., Sorgente, R., Natale, S., Gaberšek, S., Ribotti, A., Bonanno, A., & Patti, B. (2007). Effects of the 2003 european heatwave on the central mediterranean sea: Surface fluxes and the dynamical response. *Ocean Science*, *3*(2), 273–289.

Oliver, E. C., Benthuysen, J. A., Darmaraki, S., Donat, M. G., Hobday, A. J., Holbrook, N. J., Schlegel, R. W., & Sen Gupta, A. (2021). Marine heatwaves. *Annual review of marine science*, *13*, 313–342.

Oppenheim, A. V. (1999). *Discrete-time signal processing*. Pearson Education India.

Orlić, M., Gacic, M., & Laviolette, P. (1992). The currents and circulation of the adriatic sea. *Oceanologica acta*, *15*(2), 109–124.

Paschini, E., Artegiani, A., & Pinardi, N. (1993). The mesoscale eddy field of the middle adriatic sea during fall 1988. *Deep Sea Research Part I: Oceanographic Research Papers*, *40*(7), 1365–1377.

Pham, V. S., & Hwang, J. H. (2020). Effects and recovery of small-scale fluctuations in one-way nesting for regional ocean modeling. *Ocean Modelling*, *145*, 101524.

Pham, V. S., Hwang, J. H., & Ku, H. (2016). Optimizing dynamic downscaling in one-way nesting using a regional ocean model. *Ocean Modelling*, *106*, 104–120.

Pinardi, N., Arneri, E., Crise, A., Ravaioli, M., & Zavatarelli, M. (2006). The physical, sedimentary and ecological structure and variability of shelf areas in the mediterranean sea (27). *The sea*, *14*, 1243–330.

Pinardi, N., & Masetti, E. (2000). Variability of the large scale general circulation of the mediterranean sea from observations and modelling: A review. *Palaeogeography, Palaeoclimatology, Palaeoecology*, *158*(3-4), 153–173.

Pinardi, N., Allen, I., Demirov, E., De Mey, P., Korres, G., Lascaratos, A., Le Traon, P.-Y., Maillard, C., Manzella, G., & Tziavos, C. (2003). The mediterranean ocean forecasting system: First phase of implementation (1998–2001). *Annales Geophysicae*, *21*(1), 3–20.

Pinardi, N., Zavatarelli, M., Adani, M., Coppini, G., Fratianni, C., Oddo, P., Simoncelli, S., Tonani, M., Lyubartsev, V., Dobricic, S., et al. (2015). Mediterranean sea large-scale low-frequency ocean variability and water mass formation rates from 1987 to 2007: A retrospective analysis. *Progress in Oceanography*, *132*, 318–332.

Pranić, P., Denamiel, C., Janeković, I., & Vilibić, I. (2023). Multi-model analysis of the adriatic dense-water dynamics. *Ocean Science*, *19*(3), 649–670.

Querin, S., Bensi, M., Cardin, V., Solidoro, C., Bacer, S., Mariotti, L., Stel, F., & Malačič, V. (2016). Saw-tooth modulation of the deep-water thermohaline properties in the southern adriatic sea. *Journal of Geophysical Research: Oceans*, *121*(7), 4585–4600.

Reckinger, S. M., Petersen, M. R., & Reckinger, S. J. (2015). A study of overflow simulations using mpas-ocean: Vertical grids, resolution, and viscosity. *Ocean Modelling*, *96*, 291–313.

Renault, L., Masson, S., Arsouze, T., Madec, G., & McWilliams, J. C. (2020). Recipes for how to force oceanic model dynamics. *Journal of Advances in Modeling Earth Systems*, *12*(2), e2019MS001715.

Renault, L., Molemaker, M. J., McWilliams, J. C., Shchepetkin, A. F., Lemarié, F., Chelton, D., Illig, S., & Hall, A. (2016). Modulation of wind work by oceanic current interaction with the atmosphere. *Journal of Physical Oceanography*, *46*(6), 1685–1704.

Roberts, J., & Roberts, T. D. (1978). Use of the butterworth low-pass filter for oceanographic data. *Journal of Geophysical Research: Oceans*, *83*(C11), 5510–5514.

Rosselló, P., Pascual, A., & Combes, V. (2023). Assessing marine heat waves in the mediterranean sea: A comparison of fixed and moving baseline methods. *Frontiers in Marine Science*, *10*.

Rubino, A., Gačić, M., Bensi, M., Kovačević, V., Malačič, V., Menna, M., Negretti, M. E., Sommeria, J., Zanchettin, D., Barreto, R. V., et al. (2020). Experimental evidence of long-term oceanic circulation reversals without wind influence in the north ionian sea. *Scientific reports*, *10*(1), 1905.

Shchepetkin, A. F., & McWilliams, J. C. (2005). The regional oceanic modeling system (roms): A split-explicit, free-surface, topography-following-coordinate oceanic model. *Ocean modelling*, *9*(4), 347–404.

Simoncelli, S., Pinardi, N., Oddo, P., Mariano, A. J., Montanari, G., Rinaldi, A., & Deserti, M. (2011). Coastal rapid environmental assessment in the northern adriatic sea. *Dynamics of atmospheres and oceans*, *52*(1-2), 250–283.

Skamarock, W. C., Duda, M. G., Ha, S., & Park, S.-H. (2018). Limited-area atmospheric modeling using an unstructured mesh. *Monthly Weather Review*, *146*(10), 3445–3460.

Spall, M. A., & Holland, W. R. (1991). A nested primitive equation model for oceanic applications. *Journal of Physical Oceanography*, *21*(2), 205–220.

Stott, P. A., Stone, D. A., & Allen, M. R. (2004). Human contribution to the european heatwave of 2003. *Nature*, *432*(7017), 610–614.

Thompson, K. R., Wright, D. G., Lu, Y., & Demirov, E. (2006). Erratum to "a simple method for reducing seasonal bias and drift in eddy resolving ocean models"[ocean modelling 13 (2006) 109–125]. *Ocean Modelling*, *14*(1-2), 122–138.

Trotta, F., Pinardi, N., Fenu, E., Grandi, A., & Lyubartsev, V. (2017). Multinest high-resolution model of submesoscale circulation features in the gulf of taranto. *Ocean Dynamics*, *67*, 1609–1625.

Tseng, Y.-h., Bryan, F. O., & Whitney, M. M. (2016). Impacts of the representation of riverine freshwater input in the community earth system model. *Ocean Modelling*, *105*, 71–86.

Tsimplis, M. N., Proctor, R., & Flather, R. (1995). A two-dimensional tidal model for the mediterranean sea. *Journal of Geophysical Research: Oceans*, *100*(C8), 16223–16239.

Verri, G., Mahmoudi Kurdistani, S., Coppini, G., & Valentini, A. (2021). Recent advances of a box model to represent the estuarine dynamics: Time-variable estuary length and eddy diffusivity. *Journal of Advances in Modeling Earth Systems*, *13*(4), e2020MS002276.

Verri, G., Pinardi, N., Bryan, F., Tseng, Y.-h., Coppini, G., & Clementi, E. (2020). A box model to represent estuarine dynamics in mesoscale resolution ocean models. *Ocean Modelling*, *148*, 101587.

Verri, G., Pinardi, N., Oddo, P., Ciliberti, S. A., & Coppini, G. (2018). River runoff influences on the central mediterranean overturning circulation. *Climate Dynamics*, *50*, 1675–1703.

Vested, H. J., Berg, P., & Uhrenholdt, T. (1998). Dense water formation in the northern adriatic. *Journal of marine systems*, *18*(1-3), 135–160.

Vilibić, I., Mihanović, H., Janeković, I., & Šepić, J. (2016). Modelling the formation of dense water in the northern adriatic: Sensitivity studies. *Ocean modelling*, *101*, 17–29.

Vilibić, I., & Orlić, M. (2002). Adriatic water masses, their rates of formation and transport through the otranto strait. *Deep Sea Research Part I: Oceanographic Research Papers*, *49*(8), 1321–1340.

Vilibić, I., & Supić, N. (2005). Dense water generation on a shelf: The case of the adriatic sea. *Ocean Dynamics*, *55*(5-6), 403–415.

Vilibić, I., Zemunik, P., Dunić, N., & Mihanović, H. (2020). Local and remote drivers of the observed thermohaline variability on the northern adriatic shelf (mediterranean sea). *Continental Shelf Research*, *199*, 104110.

Vodopivec, M., Zaimi, K., & Peliz, Á. J. (2022). The freshwater balance of the adriatic sea: A sensitivity study. *Journal of Geophysical Research: Oceans*, *127*(11), e2022JC018870.

von Storch, H., Langenberg, H., & Feser, F. (2000). A spectral nudging technique for dynamical downscaling purposes. *Monthly weather review*, *128*(10), 3664–3673.

Waldron, K. M., Paegle, J., & Horel, J. D. (1996). Sensitivity of a spectrally filtered and nudged limited-area model to outer model options. *Monthly weather review*, *124*(3), 529–547.

Wright, D., Thompson, K., & Lu, Y. (2006). Assimilating long-term hydrographic information into an eddy-permitting model of the north atlantic. *Journal of Geophysical Research: Oceans*, *111*(C9).

Yari, S., Kovačević, V., Cardin, V., Gačić, M., & Bryden, H. L. (2012). Direct estimate of water, heat, and salt transport through the strait of otranto. *Journal of Geophysical Research: Oceans*, *117*(C9).

Zavatarelli, M., & Pinardi, N. (2003). The adriatic sea modelling system: A nested approach. *Annales Geophysicae*, *21*(1), 345–364.

Zore-Armanda, M. (1963). Mixing of three water types in the south adriatic. *Rapp. P.-v Reun. Comm int. Explor. scient. Mermedit., 17, 879*, *885.*